

Air Force Institute of Technology

AFIT Scholar

Theses and Dissertations

Student Graduate Works

3-1-2019

Optical and Electron Paramagnetic Resonance Characterization of Point Defects in Semiconductors

Elizabeth M. Scherrer

Follow this and additional works at: <https://scholar.afit.edu/etd>



Part of the [Electromagnetics and Photonics Commons](#)

Recommended Citation

Scherrer, Elizabeth M., "Optical and Electron Paramagnetic Resonance Characterization of Point Defects in Semiconductors" (2019). *Theses and Dissertations*. 2463.

<https://scholar.afit.edu/etd/2463>

This Dissertation is brought to you for free and open access by the Student Graduate Works at AFIT Scholar. It has been accepted for inclusion in Theses and Dissertations by an authorized administrator of AFIT Scholar. For more information, please contact richard.mansfield@afit.edu.



**OPTICAL AND ELECTRON PARAMAGNETIC RESONANCE
CHARACTERIZATION OF POINT DEFECTS IN SEMICONDUCTORS**

DISSERTATION

Elizabeth M. Scherrer, Captain, USAF

AFIT-ENP-DS-19-M-091

**DEPARTMENT OF THE AIR FORCE
AIR UNIVERSITY**

AIR FORCE INSTITUTE OF TECHNOLOGY

Wright-Patterson Air Force Base, Ohio

DISTRIBUTION STATEMENT A

APPROVED FOR PUBLIC RELEASE; DISTRIBUTION UNLIMITED.

The views expressed in this thesis are those of the author and do not reflect the official policy or position of the United States Air Force, Department of Defense, or the United States Government. This material is declared a work of the U.S. Government and is not subject to copyright protection in the United States.

AFIT-ENP-DS-19-M-091

**OPTICAL AND ELECTRON PARAMAGNETIC RESONANCE
CHARACTERIZATION OF POINT DEFECTS IN SEMICONDUCTORS**

DISSERTATION

Presented to the Faculty

Department of Engineering Physics

Graduate School of Engineering and Management

Air Force Institute of Technology

Air University

Air Education and Training Command

In Partial Fulfillment of the Requirements for the

Doctor of Philosophy Degree

Elizabeth M. Scherrer, BA, MS

Captain, USAF

March 2019

DISTRIBUTION STATEMENT A

APPROVED FOR PUBLIC RELEASE; DISTRIBUTION UNLIMITED.

OPTICAL AND ELECTRON PARAMAGNETIC RESONANCE
CHARACTERIZATION OF POINT DEFECTS IN SEMICONDUCTORS

Elizabeth M. Scherrer, BA, MS
Captain, USAF

Committee Membership:

Dr. Nancy C. Giles
Chair

Dr. Dean R. Evans
Member

Lt Col Michael R. Hogsed, PhD
Member

Dr. John W. McClory
Member

ADEDEJI B. BADIRU, PhD
Dean, Graduate School of Engineering and Management

Abstract

Point defects in two semiconductor materials, both with promising optical properties, are investigated. The first material, CdSiP₂, is a nonlinear optical material in which absorption bands due to point defects can hinder performance when used in frequency conversion applications in the infrared. The second material, Sn₂P₂S₆, is a photorefractive material where point defects with specific properties are needed to optimize response in dynamic holography applications. Electron paramagnetic resonance (EPR) spectroscopy is used to identify the electronic structure of defects and their charge states. Correlations between EPR spectra and optical absorption allow assignments for the primary absorption bands in CdSiP₂. This research established that singly ionized silicon vacancies in CdSiP₂ (V_{Si}^-) are responsible for three unwanted absorption bands peaking near 800 nm, 1.0 μm , and 1.9 μm . Two new acceptor defects were identified in CdSiP₂: the neutral silicon-on-phosphorus antisite (Si_P^0) and the neutral copper-on-cadmium (Cu_{Cd}^0). These defects are associated with two additional broad photoinduced optical absorption bands appearing at 0.8 μm and 1.4 μm . A series of new point defects have been identified in tellurium-doped Sn₂P₂S₆ crystals using EPR. An iodine ion on a phosphorous site and a tellurium ion on a Sn site are trapped-electron centers. Five trapped-hole centers involve Te ions replacing sulfur ions. The g-matrix has been determined for each of the new paramagnetic defects in Sn₂P₂S₆ and models are assigned.

Acknowledgements

I would like to express my sincere appreciation to my faculty advisor, Dr. Nancy Giles, and to Dr. Larry Halliburton for their expertise and providing guidance throughout my dissertation efforts. I also thank them for pushing me to succeed. I would also like to thank my committee for their support and sharing their knowledge with me.

Additionally, I would like to share my gratitude to my family for their continued patience and encouragement during this time.

Elizabeth M. Scherrer

Table of Contents

	Page
Abstract.....	iv
Table of Contents.....	vi
List of Figures.....	viii
List of Tables.....	xiv
List of Equations.....	xv
Chapter 1. Introduction.....	1
Chapter 2. Physical Properties of CdSiP ₂ and Sn ₂ P ₂ S ₆	4
2.1 CdSiP ₂ Crystals.....	4
2.2 Sn ₂ P ₂ S ₆ Crystals.....	10
Chapter 3. Characterization Methods.....	12
3.1 Principles of Electron Paramagnetic Resonance.....	12
3.2 Electron Paramagnetic Resonance Spectrometer.....	15
3.3 Principles of Optical Absorption.....	22
3.4 Fourier-Transform Infrared Spectrometer.....	24
3.5 UV/VIS/NIR Spectrophotometer.....	26
Chapter 4. Previous Studies of Point Defects in ZnGeP ₂ , CdSiP ₂ and Sn ₂ P ₂ S ₆	28
4.1 Zinc Germanium Diphosphide.....	29
4.2 Cadmium Silicon Diphosphide.....	31
4.2.1 Native Defect and Impurity Identifications.....	31
4.2.2 Optical Properties of CSP.....	33
4.3 Tin Hypothiodiphosphate.....	34
4.3.1 Sb-doped SPS.....	37
Chapter 5. CdSiP ₂ Results and Analysis.....	40
5.1 Silicon Vacancies and Associated Optical Absorption.....	40
5.1.1 Discussion on Compensation.....	45
5.1.2 Gaussian Fitting of Optical Absorption Spectra.....	47
5.2 Silicon-on-Phosphorus and Copper Acceptors.....	48
5.2.1 EPR of New Acceptors.....	49
5.2.2 Optical Absorption at 77 K.....	53

5.3 Carbon-on-Cation-Site Defect	58
5.4 Cadmium Vacancies.....	60
5.5 Neutron-Irradiated CSP.....	61
5.6 Effects of 1064 nm Light	62
5.6.1 CSP Sample 21D.....	63
Chapter 6. Sn ₂ P ₂ S ₆ Results and Analysis.....	65
6.1 Tellurium-Doped Sn ₂ P ₂ S ₆ Crystals	66
6.1.1 Tellurium-Related EPR Spectra	67
6.1.2 Extracting Spin-Hamiltonian Matrix Parameters	75
6.1.3 Models for Te-Related Defects	78
6.2 Iodine-Related EPR Spectrum	81
6.2.1 Extracting Spin-Hamiltonian Matrix Parameters	84
6.2.2 Model for Iodine in Sn ₂ P ₂ S ₆	87
6.3 Copper Impurity in Sn ₂ P ₂ S ₆ Crystals	89
6.3.1 Model for the Copper Impurity	91
6.4 Silver-Related Defect in Sn ₂ P ₂ S ₆ Crystals.....	92
Chapter 7. Conclusions	94
Bibliography	97
Appendix A – MatLab Fitting Program to Extract EPR Parameters	102
Appendix B – Magnetic Field Positions for Te-related Defects.....	111
Defect A	111
Defect B	113
Defect C	116
Defect D	118
Defect E.....	120
Defect F	123

List of Figures

	Page
Figure 2.1. Examples of large CSP crystals grown at BAE Systems. The crystal on the left is representative of the size of samples used in this study. Reproduced from [6] with permission from Elsevier.....	5
Figure 2.2. Ball and stick diagram of CdSiP ₂ . Phosphorus atoms are red, Cd is green, and Si is purple. Reproduced from [8] with permission from AIP Publishing.....	6
Figure 2.3. View of CSP looking down the c-axis. Reproduced from [8] with permission from AIP Publishing.....	6
Figure 2.4. Temperature dependences of indices of refraction for CSP for (a) ordinary and (b) extraordinary polarizations. Reproduced from [3]. © 2018 Optical Society of America.....	9
Figure 2.5. Crystal structure of SPS. The green atoms are tin, the sulfur atoms are red, and the phosphorus atoms are blue. Each figure shows the crystal structure as viewed along the <i>a</i> , <i>b</i> , and <i>c</i> axes, respectively.	11
Figure 3.1. Energy levels and associated EPR spectra for an $S = 1/2$ spin system (left) and an $S = 1/2, I = 1$ spin system (right). A magnetic field can split the energy levels..	14
Figure 3.2. Bruker EPR Spectrometer with key components labeled in red	16
Figure 3.3. Effects of microwave power on three defects in CdSiP ₂ are shown. The data were taken at 12 K after the sample had been exposed to 633 nm HeNe laser light. Each defect is best seen at a different microwave power.	19

Figure 3.4. The difference in magnetic field measurement between the Hall field vs. NMR probe is shown. A line (blue) was fit to the data from 1500 – 10000 G, and a quartic line (red) was used to fit the data above 10000 G. 21

Figure 3.5. Optical Diagram of a Fourier-Transform Infrared Spectrometer. 24

Figure 3.6. Diagram of a dual-beam absorption spectrophotometer. 27

Figure 4.1. Optical absorption data for various ZGP samples (left). The V_{Zn}^- was identified as the defect responsible based on EPR signal intensity of the defect correlated with the absorption coefficient at 1 μ m. Reproduced from [43] with permission from AIP Publishing. 31

Figure 4.2. Optical absorption data of two CSP samples at room temperature shown using both o-and e-polarized light (left). Also shown is one sample (24A) with E parallel to c-axis at various temperatures. Reproduced from [48] with permission from Elsevier. 33

Figure 4.3. EPR spectrum of both the Sn and S vacancies show phosphorus hyperfine. Data taken at 90 K with crystal axis c aligned along the magnetic field. Reproduced from [22] with permission from AIP Publishing. 35

Figure 4.4. EPR spectrum of the small polaron (Sn^{3+} ions) in a $Sn_2P_2S_6$ crystal. The spectrum was taken at 90 K with the magnetic field along the crystal b axis. Reproduced from [49] with permission from IOP Publishing..... 37

Figure 4.5. EPR signals from Sb-doped SPS samples shown. The red stick diagrams depict the lines for the trapped hole while the blue stick diagram shows the trapped electron. Reproduced from [27]. © 2016 Optical Society of America..... 39

Figure 4.6. The left image shows the hole trap model that corresponds to the red stick diagram. The right image shows the electron trap that corresponds to the blue stick diagram. Reproduced from [27]. © 2016 Optical Society of America..... 39

Figure 5.1. Optical absorption from CdSiP₂ at room temperature. Top left shows the optical absorption data before and during illumination with a 633 nm HeNe laser light. Bottom left shows the difference between the “light-on” and “light-off”. The right plot shows the difference curves for eight CSP samples. Reproduced from [50]. © 2017 Optical Society of America 41

Figure 5.2. EPR spectra at 300 K from CSP sample 32Z. (a) Taken with no illumination. (b) Taken with 633 nm light on. (c) Difference spectrum (“light-on” minus “light-off”). The lowest spectrum shows the silicon-vacancy acceptor and the antisite donor. Reproduced from [50]. © 2017 Optical Society of America 42

Figure 5.3. Left: Correlation of EPR intensity of V_{Si} signal vs intensity of 800 nm absorption peak. Right: Decay rate of V_{Si} EPR signal and 800 nm absorption peak. Reproduced from [50]. © 2017 Optical Society of America..... 43

Figure 5.4: Optical absorption spectra from sample 30Z (top) and 21D (bottom). Black curve is optical absorption data, red curves are Gaussian fits. Blue curve (top graph) is the sum of the two Gaussian curves (red). 48

Figure 5.5. Photo-induced EPR spectrum of CSP 47Z (a) during illumination and (b) 5 minutes after illumination while sample remained in the dark. Both spectra were collected at 77 K and with very high microwave power. Reproduced from [51] with permission from AIP Publishing. 50

Figure 5.6. EPR spectrum of silicon-on-cadmium anitsite donor. This spectrum was obtained at 77 K using very low microwave power to avoid saturation. Reproduced from [51] with permission from AIP Publishing. 51

Figure 5.7. EPR spectra of two new acceptors. Left – (a) experimental data and (b) simulation of copper-on-cadmium acceptor. Right – (a) experimental data and (b) simulation of silicon-on-phosphorus acceptor. Reproduced from [51] with permission from AIP Publishing. 52

Figure 5.8. Optical absorption spectra from sample 47Z. Left: There is no measureable increased absorption with a 633 nm laser at room temperature. Right: At 77 K, the sample shows a large increase in absorption when illuminated with a 633 nm HeNe laser..... 54

Figure 5.9. Photoinduced optical absorption data from sample 47Z as a function of temperature. Reproduced from [51] with permission from AIP Publishing. 55

Figure 5.10. Optical absorption spectra from sample 48Z showing the polarization dependence of the photoinduced optical absorption bands at 100 K. There was a detector change at 1 μm (approximately at 1.3 eV). Some of the 633 nm HeNe laser light is present in the spectrum near 2.0 eV..... 56

Figure 5.11. Optical absorption spectra from sample 47Z. As the sample is cooled, the band edge shifts to shorter wavelength and reveals an absorption band at 610 nm. The data was taken at room temperature and 77 K 58

Figure 5.12. The upper spectrum is the photoinduced signal that decayed when the 633 nm HeNe laser was removed (red) and a simulation of the Si_{Cd}^+ EPR signal (blue).

The lower spectrum shows the remaining signal when the SiCd^+ signal is removed (i.e., red minus blue)..... 59

Figure 5.13. Lifetime data from CSP sample 48Z showing the decay of the singly ionized cadmium vacancy. Compared with other defects, the cadmium vacancy is very unstable even at 10 K..... 61

Figure 5.14. Optical absorption spectra from sample 49Z. The black curve is before neutron irradiation and the red curve is after neutron irradiation. 62

Figure 6.1. EPR data from a Te-doped SPS crystal. The top spectrum was taken at 20 K while 633 nm light was illuminating the sample. The bottom spectrum was also taken at 20 K, after the sample was warmed to 160 K for 2 minutes. The red lines are magnified 5x to show the Sn hyperfine lines. The magnetic field was along the c axis. 68

Figure 6.2. EPR angular dependence from a 1% Te-doped SPS crystal. These results show that there are five different defects labeled A, B, C, D, and E..... 70

Figure 6.3. EPR angular dependence data for defects A, B, and C in Te-doped SPS. These data were taken at 20 K while the sample was illuminated with 633 nm HeNe laser light. 71

Figure 6.4. EPR angular dependence data for defects D and E in Te-doped SPS. The sample was illuminated with 633 nm laser light at 20 K, then briefly warmed to 110 K in the dark. The data were subsequently taken at 20 K without laser light. 72

Figure 6.5. Pulsed anneal results from a 1% Te-doped SPS crystal showing the thermal decay of each center. EPR spectra were monitored at 20 K. The sample was held at each higher temperature for two minutes. 73

Figure 6.6. EPR spectrum of defect F in a Te-doped SPS crystal. Associated ^{125}Te hyperfine lines are identified. 74

Figure 6.7. EPR angular-dependence for defect F in Te-doped SPS crystals..... 75

Figure 6.8. (Left) Models for defects A, B, C, D, and E involving Te ions on a S site. There may be a Sn vacancy next to the defect. (Right) Model for defect F involving a Te ion on a Sn site..... 80

Figure 6.9. Iodine-related EPR spectra taken at 20 K from a Te-doped SPS crystal after exposure to 633 nm laser light..... 83

Figure 6.10. EPR spectra from Cu impurities in SPS crystals..... 90

Figure 6.11. Thermal stability of the photoinduced Cu EPR signal in SPS. 91

Figure 6.12. EPR spectrum obtained from a 1% Ag-doped SPS crystal. The spectrum was taken at 30 K with the magnetic field along the b axis while illuminated with 633 nm laser light during measurement..... 93

List of Tables

	Page
Table 2.1: Temperature-dependent Sellmeier coefficients from Reference [3]	9
Table 6.1: Spin Hamiltonian parameters for Te-related defects	78
Table 6.2: Spin-Hamiltonian parameters describing iodine EPR spectrum in SPS crystals	88
Table 6.3: Spin-Hamiltonian parameters for copper in a 1% Cu-doped SPS crystal.	92

List of Equations

	Page
Equation 2.1 –General Sellmeier Equation.....	8
Equation 2.2 – Sellmeier Equations for CSP	8
Equation 3.1– Spin Hamiltonian.....	13
Equation 3.2– Defect concentration in terms of EPR signal intensity.....	20
Equation 3.3– EPR Calibration Curve (Hall Field vs. NMR Probe Magnetic Field Measurement)	22
Equation 3.4– Beer’s Law.....	22
Equation 3.5– Optical Density as a Function of Absorption Coefficient	23
Equation 3.6– Reflective Losses of Light due to a Surface	23
Equation 6.1– Spin Hamiltonian for Te-Related Defects in SPS	76
Equation 6.2 – Spin Hamiltonian in g-matrix principle axes.....	76
Equation 6.3– Spin Hamiltonian in laboratory x, y, z axes	77
Equation 6.4– Spin Hamiltonian written with raising and lowering operators.....	77
Equation 6.5– Spin Hamiltonian for Te-related defects in SPS.....	77
Equation 6.6– Spin Hamiltonian for Iodine-Related Defects in SPS	84
Equation 6.7– Spin Hamiltonian Operators in (x, y, z) axes for Iodine in SPS.....	85
Equation 6.8– Spin Hamiltonian in x, y, z axes for Iodine in SPS	86
Equation 6.9– Raising and Lowering operators.....	87

OPTICAL AND ELECTRON PARAMAGNETIC RESONANCE CHARACTERIZATION OF POINT DEFECTS IN SEMICONDUCTORS

Chapter 1. Introduction

This dissertation describes the results of an experimental research program that identifies and characterizes donors and acceptors, at the quantum level, in two recently developed ternary semiconductors with useful optical properties. These materials are cadmium silicon diphosphide (CdSiP_2) and tin hypthiodiphosphate ($\text{Sn}_2\text{P}_2\text{S}_6$). Single crystals of CdSiP_2 , or CSP for short, have promising nonlinear optical properties and are used in optical parametric oscillator applications in the mid-infrared. The ability to produce tunable coherent laser beams in the 3 to 6.5 μm region leads to a variety of useful devices with commercial and military value. Single crystals of $\text{Sn}_2\text{P}_2\text{S}_6$, or SPS for short, are photorefractive with fast response times and high gain and are especially useful for beam steering and signal processing applications in the near-infrared. These optical materials have room-temperature band gaps of about 2.2-2.4 eV [1-5].

Point defects (i.e., the donors and acceptors) play important roles in these materials. All of the presently available single crystals of CSP and SPS are highly compensated semiconductors with comparable concentrations of donors and acceptors. Even though their applications are quite different, the presence or absence of point defects are the focus of present-day development activities for both materials. Point defects cause unwanted absorption bands in CSP that affect the performance of optical parametric oscillators in the mid-infrared. In SPS, point defects must be present in a controlled manner to ensure that there are sufficient concentrations of appropriate electron and hole traps to allow transient

photoinduced changes in charge states. These photoinduced movements of charge give the fast response times to incident light and the high photorefractive gain. Both materials bear a physical resemblance (both are red or orange-red in color), but their crystal structures and optical properties are distinct from each other. These similarities and differences in material properties set the stage for the work presented in this dissertation, which focuses primarily on point defects in these two materials.

Chapter 2 begins with a review of the physical characteristics of the two semiconductor materials being studied. Growth techniques are described briefly. Crystal structures for each are introduced, where CSP is tetragonal and SPS is monoclinic. Bulk material optical properties are also presented.

Chapter 3 reviews the characterization methods used in this work: electron paramagnetic resonance (EPR) and optical absorption spectroscopy. Two different instruments are used to collect optical absorption data. These are a Fourier transform infrared (FTIR) spectrometer and a uv/vis/near infrared dual-beam spectrophotometer.

Chapter 4 summarizes previously reported research on defects in CSP and also in ZnGeP₂, a material analogous to CdSiP₂. Previous research performed on point defects in undoped, Sb-doped, and Ag-doped Sn₂P₂S₆ is also reviewed. These earlier reports provide intrinsic defect assignments and prove very useful in analyzing the new defect EPR spectra in Sn₂P₂S₆ that are revealed in the present dissertation study.

The results and analysis are divided into two separate chapters. Chapter 5 describes results from CSP. A correlation study between singly ionized silicon vacancies and unwanted optical absorption using photo-induced EPR and photoinduced optical

absorption is described. Assignments of models for two EPR spectra to new acceptors in CSP are made. The effects of 633 nm and 1064 nm light on EPR spectra and absorption spectra are reviewed. Chapter 6 presents the results obtained from SPS crystals. In tellurium-doped SPS crystals, EPR spectra from six Te-related defect centers and one iodine impurity center are observed. The iodine impurity replaces a phosphorous ion. The discovery of iodine is significant because iodine is used in the crystal growth process and, thus, cannot be readily eliminated from the SPS crystal.

Chapter 2. Physical Properties of CdSiP₂ and Sn₂P₂S₆

Both CdSiP₂ and Sn₂P₂S₆ are semiconductors with band gaps around 2.2-2.4 eV (and thus they both appear red to the eye). The two materials, however, have quite different crystal structures and physical properties. This chapter reviews their crystal structures, crystal growth methods, and optical properties.

2.1 CdSiP₂ Crystals

CdSiP₂, or simply CSP, is a nonlinear optical material. The CSP crystals investigated in this dissertation were grown by Peter Schunemann and Kevin Zawilski at BAE Systems (Nashua, NH) using the horizontal gradient freeze method [6]. This growth method uses a fused silica ampoule where the P is loaded at one end, and the Cd and Si are placed into a pyrolytic boron nitride (PBN) coated graphite boat, which was subsequently placed at the opposite end of the ampoule from the P. The ampoule was then evacuated (i.e., placed under vacuum) before going into a two-zone furnace. The hotter side of the furnace was where the Cd and Si were placed (in the PBN-coated graphite boat) which was held at a temperature greater than 1133°C. The P side of the ampoule was maintained at a lower temperature of less than 600°C. This method of crystal growth produced relatively large crystals, as shown in Figure 2.1. The CSP samples used in the EPR and optical absorption studies were cut from larger boules and had approximate dimensions of 3 x 3 x 6 mm³. This is the largest size that would fit into the Bruker EPR spectrometer cryostat glassware.

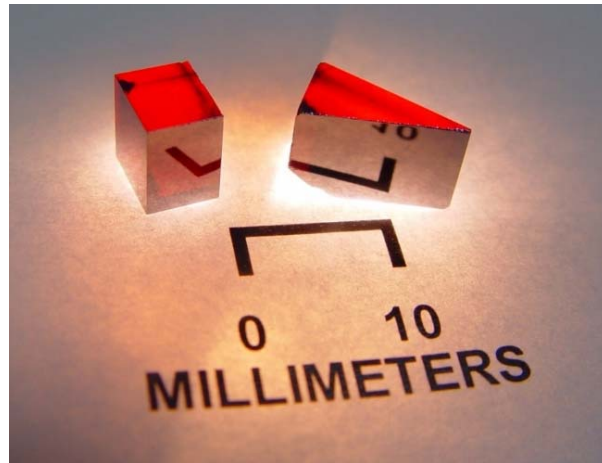


Figure 2.1. Examples of large CSP crystals grown at BAE Systems. The crystal on the left is representative of the size of samples used in this study. Reproduced from [6] with permission from Elsevier.

CdSiP_2 has a tetragonal crystal structure with space group $\bar{4}2m$ [7]. The crystal structure is referred to as a chalcopyrite and is similar to zinc blende, as shown in Figure 2.2. Each cation (Group II cadmium and Group IV silicon) has four nearest neighbor P^{3-} anions (tetrahedral bonding). Each P anion is tetrahedrally bonded with two Cd^{2+} and two Si^{4+} neighbors. Since the ionic radii of the cations are significantly different ($\text{Cd}^{2+} = 0.78 \text{ \AA}$ and $\text{Si}^{4+} = 0.26 \text{ \AA}$), the crystal structure is compressed along the c axis. The anions are rotated about the c axis, shown in Figure 2.3. The ideal ratio for a chalcopyrite structure is $c/a = 2$. For CSP, given that $a = 5.68 \text{ \AA}$ and $c = 10.431 \text{ \AA}$, the ratio is notably less than 2 ($c/a = 1.836$) due to the compression [8-10].

CSP is not a direct bandgap material, but rather is referred to as pseudodirect bandgap material. There are three conduction bands and three valence bands which arise due to spin-orbit coupling. The transitions between each valence band and the Γ_7 conduction band are referred to as the A, B, and C transitions.

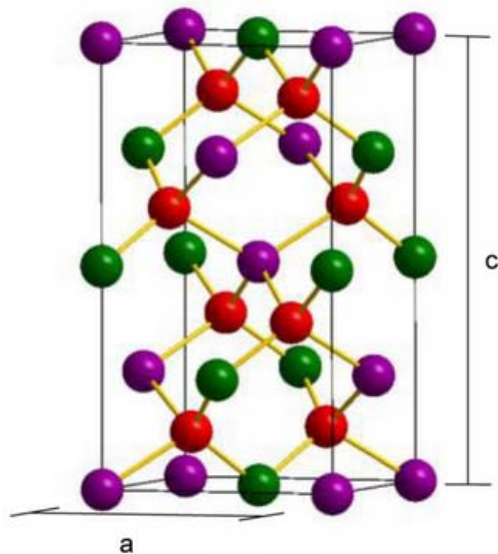


Figure 2.2. Ball and stick diagram of CdSiP_2 . Phosphorus atoms are red, Cd is green, and Si is purple. Reproduced from [8] with permission from AIP Publishing.

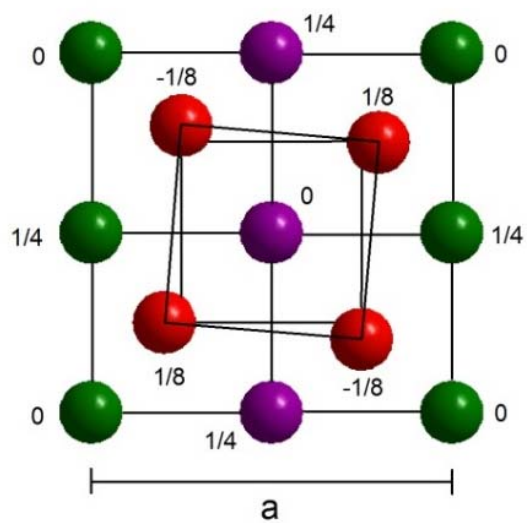


Figure 2.3. View of CSP looking down the c-axis. Reproduced from [8] with permission from AIP Publishing.

In direct bandgap chalcopyrites such as CdGeAs₂, the A transition corresponds to the lowest energy transition. In pseudodirect bandgap chalcopyrites like CSP, the lowest energy conduction band is Γ_6 (not Γ_7 as for direct bandgap chalcopyrites) so the A transition does not correspond to the lowest energy bandgap. Instead, the corresponding transitions from each valence band to Γ_6 are referred to as A', B' and C'. The lowest energy transition in CSP is therefore the A' transition [9]. Each of these transitions has its own selection rules which depend on the polarization of the incident light. Different conditions produce different absorption spectra. For example, transition A favors polarization where the electric field is parallel to the crystal c axis whereas transitions B and C favor polarization where the electric field is perpendicular to the crystal c axis. Similarly, transitions B' and C' also favor perpendicular polarization, but transition A' is a weakly allowed transition that favors perpendicularly polarized light. For a pseudodirect bandgap material like CSP, transitions A, B, and C involve the third highest conduction band. The fundamental absorption edge, which is caused by optical transitions to the lowest conduction band, is at 2.2 eV [10].

The nonlinear optical coefficient for CSP has been reported as $d_{\text{eff}} = 57.2$ pm/V [11]. Because of the excellent nonlinear optical properties of CSP, it is used for nonlinear frequency conversion applications (such as in optical parametric oscillators) with a pump wavelength in the near-infrared. The output wavelength is tunable from 2 -10 μm when pumped with 1550 nm laser, for example [6]. Similarly, a 2055 nm pump can produce output wavelengths between 3-10 μm depending on the phase matching angle. CSP has

also been shown to produce output wavelengths near 6.5 μm that are not critically phase matched when pumped with 1-1.5 μm light [12].

Previous research has also been analyzing the bulk optical properties of CSP. Because CSP is a birefringent material, it has two indices of refraction: ordinary n_o and extraordinary n_e . These two refractive indices are a function of wavelength and temperature [3, 6]. These relationships are referred to as Sellmeier equations. A general form of the Sellmeier equation is shown in Equation 2.1.

$$n^2 = A + \frac{B}{\lambda^2 - C} - \frac{D}{\lambda^2 - E} \quad (2.1)$$

Zawilski et al. [6] fit experimental data to the Sellmeier equations to determine the Sellmeier coefficients. There was an empirical modification made to the third term of

. The resulting room temperature equations are shown in Equation 2.2 where λ is in units of μm .

$$\begin{aligned} n_o^2 &= 3.0811 + \frac{6.2791 \lambda^2}{\lambda^2 - 0.10452} - 0.0034888 \lambda^2 \\ n_e^2 &= 3.4343 + \frac{5.6137 \lambda^2}{\lambda^2 - 0.11609} - 0.0034264 \lambda^2 \end{aligned} \quad (2.2)$$

While Zawilski et al. [6] determined the CSP coefficients at room temperature, Wei et al. [3] studied the temperature dependence of the indices of refraction at temperatures ranging from 90 K up to 450 K. These latter results are shown in Figure 2.4. Based on these data, it is apparent that lower temperature lowers the refractive index regardless of polarization. Wei et al. [3] determined that the coefficients in the Sellmeier equation are also temperature

dependent. Those coefficients are shown in Table 2.1. Please note that temperature is in units of K, and λ is in μm .

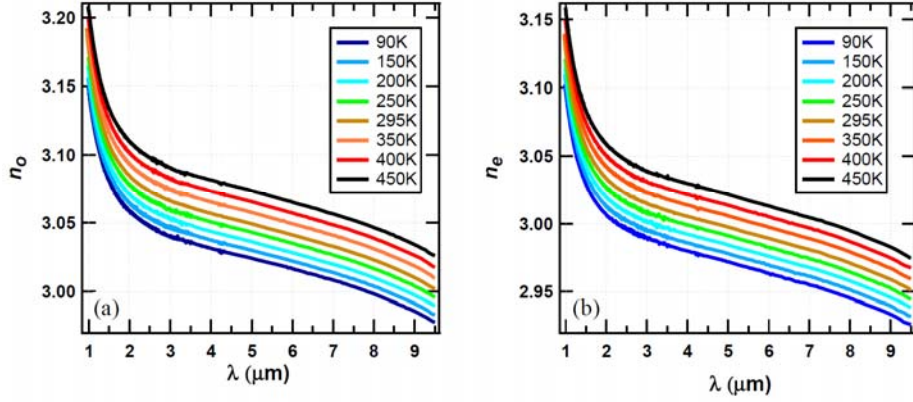


Figure 2.4. Temperature dependences of indices of refraction for CSP for (a) ordinary and (b) extraordinary polarizations. Reproduced from [3]. © 2018 Optical Society of America

Table 2.1: Temperature-dependent Sellmeier coefficients from Reference [3]

Coeff.	n_o	n_e
A	$11.95 + 5.3479 \times 10^{-4}T + 5.5894 \times 10^{-7}T^2$	$11.438 + 5.5408 \times 10^{-4}T + 5.0458 \times 10^{-7}T^2$
B	$0.6134 + 9.4768 \times 10^{-5}T + 2.0148 \times 10^{-7}T^2$	$0.61584 + 3.8668 \times 10^{-5}T + 2.9901 \times 10^{-7}T^2$
C	0.101733	0.11182
D	2334.22	2021.26
E	833.205	777.162

**Temperature is in units of Kelvins*

The index of refraction data were used to make baseline corrections for reflective losses in absorption spectra in Chapter 5. The choice to use n_o or n_e depended on the light propagation and light polarization direction. At room temperature, the results from Zawilski et al.[6] and Wei et al.[3] are equivalent. These fits were used to account for any light that is reflected at the surface of a CSP sample. Further details of how reflective losses were calculated are presented in Section 3.3.

2.2 Sn₂P₂S₆ Crystals

The other material which was studied is tin hypophosphite (Sn₂P₂S₆, or SPS). SPS is also a semiconductor and bulk crystals are typically heavily compensated. SPS holds promise as a photorefractive material with sensitivity in the near-infrared wavelength range. The crystal structure for SPS is monoclinic with space group P_n and point group m [13]. The lattice constants are the following: $a = 9.378 \text{ \AA}$, $b = 7.488 \text{ \AA}$, and $c = 6.513 \text{ \AA}$. The mirror plane is perpendicular to the b axis, and the angle between the a and c axes is 91.15° [14]. The fundamental unit cell consists of four Sn²⁺ cations and two (P₂S₆)⁴⁻ anionic molecular units, as shown in Figure 2.5 [15]. There are two inequivalent Sn positions, two inequivalent P positions, and six inequivalent S positions. At around 64°C, SPS undergoes a phase transition from paraelectric (at higher temperatures) to ferroelectric (at lower temperatures). Studies of the lattice dynamics associated with this transition are ongoing [16-21]. At room temperature, SPS has an absorption band edge near 530 nm (2.3 eV) [22-23]. At 10 K, the bandgap has increased to about 2.5 eV [4].

SPS is attractive as a photorefractive material due to fast response times and high photorefractive gain [24-26]. Intentionally doping SPS with a photo-active impurity may further improve the response times and gain. This dissertation focuses on Te-doped SPS. Tellurium can occupy any of the six inequivalent S sites, or it can occupy either of the two inequivalent Sn sites. Antimony is a similar dopant as tellurium because it can act as both a hole and electron trap depending on whether it has an adjacent Sn vacancy. Previous studies have been done on Sb-doped SPS [27-29], but far fewer defect studies have been done on Te-doped SPS. Other dopants that have been studied as part of this dissertation

include Ag and Cu. No previous research has been published on either ion. Both dopants are transition metal ions normally having partially filled d-shells; as such they are expected to behave as deep acceptors. However, in SPS, Ag and Cu do not behave as predicted, and those results are presented in detail in Sections 6.3 and 6.4.

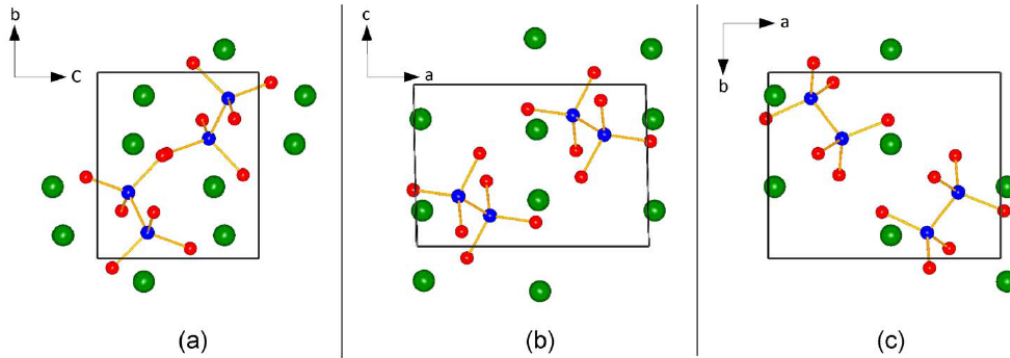


Figure 2.5. Crystal structure of SPS. The green atoms are tin, the sulfur atoms are red, and the phosphorus atoms are blue. Each figure shows the crystal structure as viewed along the *a*, *b*, and *c* axes, respectively.

The SPS samples studied in this dissertation were grown using either the chemical vapor transport method or the vertical Bridgman growth method at Uzhgorod National University (Uzhgorod, Ukraine). The chemical vapor transport method, however, is distinct from the Bridgman bulk method because the solid starting material is volatilized with a gaseous reactant and transported by a carrier gas to the growing crystal. In the case of SPS samples studied here, the gaseous reactant used contains iodine [5]. Samples grown using the two different methods exhibit different as-grown defects. Namely, those crystals grown using the chemical vapor transport method exhibit iodine impurities, which is described in further detail in section 6.2.

Chapter 3. Characterization Methods

This chapter describes the experimental methods that were employed in the investigation of point defects in CSP and SPS crystals. Two techniques, electron paramagnetic resonance (EPR) and optical absorption spectroscopies, were used. The EPR section is divided into two parts: (1) a discussion of the general principles of EPR and the spin Hamiltonian and (2) a description of the experimental instrument and its use. The optical absorption section is divided into three parts: (1) basic optical absorption principles, (2) the instrument used for near infrared absorption measurements, and (3) the spectrophotometer used to collect absorption spectra from the visible to the near-infrared.

3.1 Principles of Electron Paramagnetic Resonance

Electron paramagnetic resonance (EPR) is a high-sensitivity, high-resolution microwave spectroscopy technique that has been widely used in condensed matter physics to identify and characterize point defects in insulating and semiconducting materials. This method is capable of measuring parts per billion of paramagnetic defects under optimum conditions. These defects with unpaired spins may include extrinsic impurities (transition metal ions, rare earth ions, and substitutional donors and acceptors) and intrinsic centers (vacancies, antisites, and interstitials). When the material is placed in a slowly varying magnetic field, Zeeman splitting of the spin-related energy levels will occur and transitions between these levels can be driven by microwave photons [30]. An EPR spectrum consists of lines located at the discrete values of magnetic field where an absorption of microwave energy occurs.

The spin Hamiltonian is the “meeting” place of experiment and theory. An experimentalist determines the principal values and principal-axis directions for the g matrix, the hyperfine matrices, and the nuclear electric quadrupole matrices, whereas the theorist predicts values for these matrices using ab-initio quantum chemistry methods (such as unrestricted Hartree-Fock and density functional theory) [30]. A general Hamiltonian describes all possible energy states for a particular quantum system. The spin portion of the Hamiltonian includes only terms that involve the spin operators \mathbf{S} and \mathbf{I} , and thus forms the theoretical basis for EPR spectroscopy. Equation 3.1 is a typical spin Hamiltonian.

$$H = \mu_B \mathbf{S} \cdot \mathbf{g} \cdot \mathbf{B} - g_n \mu_N \mathbf{I} \cdot \mathbf{B} + \mathbf{I} \cdot \mathbf{A} \cdot \mathbf{S} + \mathbf{I} \cdot \mathbf{Q} \cdot \mathbf{I} \quad (3.1)$$

It includes electron and nuclear Zeeman terms, a hyperfine term, and a nuclear electric quadrupole term. The electron Zeeman and hyperfine terms describe the interactions of the electron spin \mathbf{S} with the magnetic field \mathbf{B} and the nuclear spin \mathbf{I} , respectively, while the nuclear electric quadrupole term is independent of the electron spin \mathbf{S} and the magnetic field \mathbf{B} . Constants in Equation 3.1 are the Bohr magneton (μ_B), the nuclear g factor (g_n), and the nuclear magneton (μ_N). The hyperfine matrix is denoted by \mathbf{A} , and the nuclear electric quadrupole matrix is denoted by \mathbf{Q} . In the absence of a magnetic field ($\mathbf{B} = 0$) and nuclear spin interactions, the two energy levels are degenerate for $S = 1/2$. Zero-field splittings of the electron energy levels may occur when S is greater than $1/2$ [15, 30-31]. Experimental spectra are used to determine the nuclear spin \mathbf{I} and electron spin \mathbf{S} values for a particular defect. The assignments of nuclear spin values must also take into account the natural abundance of isotopes and their respective nuclear spins.

In general, there are $2S+1$ spin states for a given value of S [30]. Because electrons tend to pair off, many defects will have $S = 0$. If there is one unpaired electron, then $S = 1/2$ and there are two spin states (referred to as spin-up and spin-down). In the case of the $S = 1/2$ and $I = 0$ system shown in the left side of Figure 3.1, there will be one line (or resonance) where absorption of microwave energy occurs as B increases. Both $S = 1$ and $S = 3/2$ systems may produce additional lines. For $I = 0$, the number of lines in the EPR spectrum is $2S$. These $2S$ number of lines represent the allowed transitions ($\Delta m_s = \pm 1$) that occur between different m_s spin states [30-31]. The relative intensities of these EPR lines represent the degeneracies of these levels. As an example, if two lines are equally intense, the transitions are equally probable.

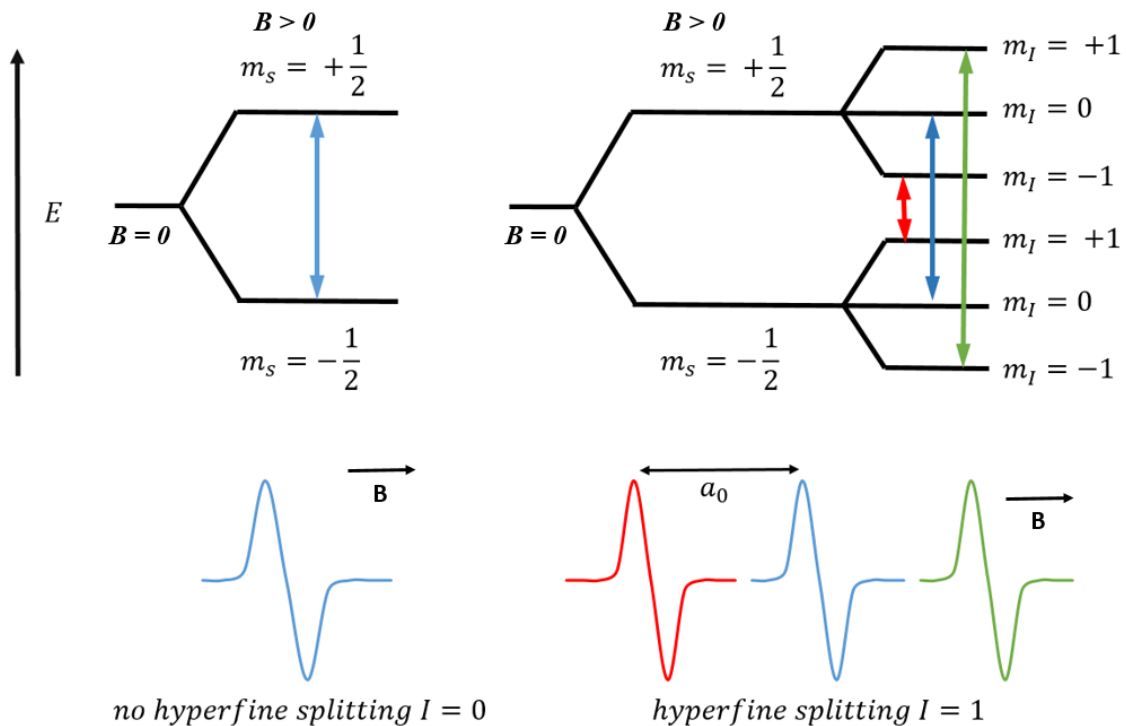


Figure 3.1. Energy levels and associated EPR spectra for an $S = 1/2$ spin system (left) and an $S = 1/2, I = 1$ spin system (right). A magnetic field can split the energy levels.

3.2 Electron Paramagnetic Resonance Spectrometer

All of the EPR spectra presented in this dissertation were obtained using a commercial cw spectrometer from Bruker that operates at X band frequency (near 9.4 GHz). These microwave photons have energies of the order of $1 \mu\text{eV}$. A typical crystalline sample is rectangular in shape with dimensions no larger than 3 mm x 3 mm x 6 mm. In EPR experiments, the sample is placed inside a resonant microwave cavity that has been critically coupled to the waveguide (i.e., there is no reflected power back along the waveguide). As the magnetic field is swept at a constant rate from low to high field, energy is absorbed by the sample when the microwave photon matches the energy separation between spin states. This absorption of energy by the spins, referred to as spin flips, is what EPR spectroscopy measures [30].

Figure 3.2 is a photograph of the AFIT Bruker EMX spectrometer and its associated liquid helium gas-flow system (from Oxford Instruments). A cryostat is attached below the microwave cavity with glassware extending up into the cavity. One end of the double-walled transfer line is inserted into the liquid helium storage dewar and the other end is inserted into the cryostat. A roughing vacuum pump is attached to the transfer line so that cold helium gas is “pulled” through the inner wall of the transfer line and into the cryostat. The helium gas exits the system through the outer wall of the transfer line. Prior to operating the spectrometer with the liquid helium gas-flow system, the internal portion of the cryostat and transfer line is purged with room-temperature nitrogen gas to remove any accumulated moisture from previous low-temperature operations. A slight amount of moisture in these lines can freeze and thus clog the flow of helium gas through the system.

When taking EPR spectra at low temperature, nitrogen purge gas flows continually around the cryostat's glassware within the microwave cavity to prevent absorption of microwaves by condensed moisture.

The resonant cavity used for all experiments in this dissertation is a Bruker Model ER4103TM. The resonant cavity is cylindrical in shape and operates in the TM_{110} mode. In this mode, the microwave magnetic field is a maximum in the center of the cavity (along the cylindrical z axis) which is ideally where the sample should be located. There is some flexibility in the sample's location relative to the cavity center, however, as the location of the peak microwave magnetic field spans a larger volume around the cylindrical z axis (vertical axis) of this cavity when compared with the standard rectangular resonant cavity which operates in the TE_{102} mode. Therefore the cylindrical cavity is well suited for samples that have a high dielectric constant [32].

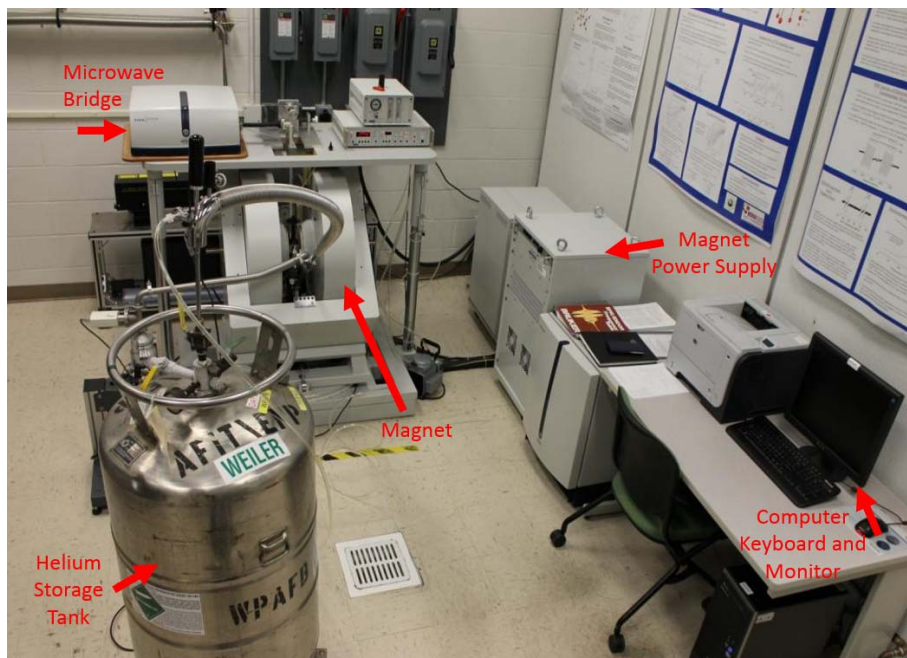


Figure 3.2. Bruker EPR Spectrometer with key components labeled in red

To increase the sensitivity of an EPR spectrometer, a 100 kHz magnetic field, referred to as the modulation, is added to the large “static” magnetic field. This causes the magnetic field that the sample sees to vary at the 100 kHz frequency. As the static magnetic field is swept through a region of interest, the reflected microwaves representing an EPR signal are amplitude-modulated at the 100 kHz frequency. A phase-sensitive detector selects only this 100 kHz signal and eliminates random noise at other frequencies and phases. Because of the application of the modulation field, the EPR signals appear as first derivatives. Therefore the “peak” of any EPR signal occurs when the signal crosses the baseline [32].

When operating the EPR spectrometer, the user must select values for several primary parameters. Two of these parameters include the modulation amplitude (measured in G) and phase (in degrees). These parameters refer to the amplitude of the 100 kHz modulation field and its phase. When an EPR signal is over-modulated, the amplitude of the modulation field is larger than the line width of the EPR signal. As the static magnetic field is swept, an over modulation brings the sample into resonance at slightly lower and slightly higher magnetic fields than at the true resonant field. This results in an artificial broadening of the EPR signal. On the other hand, under modulating the EPR signal results in a reduced signal intensity (although the line width measurement would be more accurate in this case) [32]. Therefore, when a signal is being monitored with EPR, accurate line widths must be measured with a lower modulation amplitude. The modulation amplitude is then set to reflect the line width of the signal. Similarly, the phase setting refers to the phase-sensitive detector that processes the EPR signal. This modulation phase, which can

take any value from 0 to 360 degrees, can greatly affect the EPR signal intensity. The EPR signals are maximized at two possible phase values that are 180 degrees apart, and thus the signals are minimized at a phase 90 degrees from the phase that produced the maximized signal. The main difference between the two possible phases that produce the maximum signal is that the line shape is either a positive first derivative or a negative first derivative. The positive first derivative is chosen by convention. In some materials, for example, one defect is more easily seen at 180 degree phase, whereas other defects are more easily seen at 270 degree phase. Selecting the proper phase and corresponding modulation amplitude can produce a larger, better signal.

Another parameter that the user selects is the microwave power incident on the sample. Figure 3.3 shows an example of the effect of changing the microwave power using the attenuator in the signal arm of the microwave bridge while keeping all other conditions identical. This allows the three spectra in the figure to be directly compared. These data were taken on CdSiP₂ sample 46 at 12 K. A 633 nm HeNe laser was incident on the sample for several minutes, then removed before acquiring the spectra. Three defects were produced. Although the three traces were measured under identical conditions (except for the microwave power), the signal associated with each defect has a different intensity. The microwave power is expressed in dB's, with a higher dB value representing more attenuation and less power. The 45 dB (0.00632 mW) spectrum in Figure 3.3 clearly shows the singly ionized silicon-on-cadmium Si_{Cd}⁺ defect, but this signal can barely be seen in the 20 dB (2.0 mW) or the 10 dB (20 mW) spectra. This observed behavior of the Si_{Cd}⁺ defect is due to long spin-lattice relaxation times. If the microwave power is too high, long

relaxation times of a particular defect can cause the EPR signal to saturate, which in turn reduces the signal intensity. The Fe^+ signal is best seen in Figure 3.3 at the intermediate power of 20 dB, and the signal is saturated during the 10 dB measurement. The third signal that is readily seen is the EPR signal for the singly ionized cadmium vacancy (V_{Cd}^-). This signal does not saturate even at 10 dB, but it is barely seen at 45 dB. This particular example highlights how different defects are best seen under different spectrometer microwave power settings.

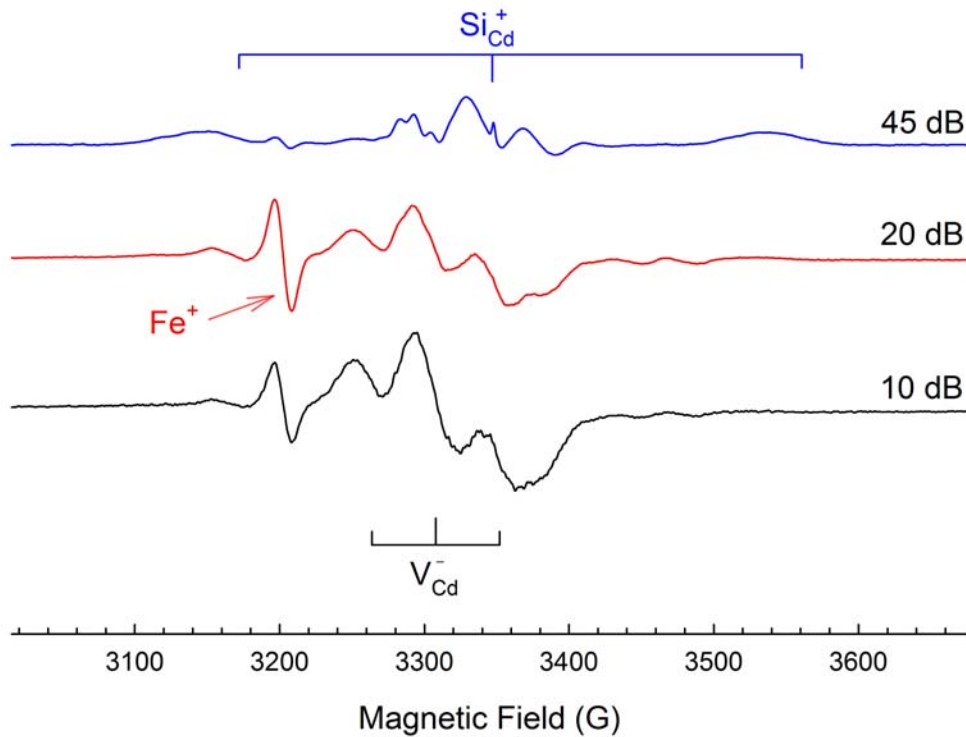


Figure 3.3. Effects of microwave power on three defects in CdSiP_2 are shown. The data were taken at 12 K after the sample had been exposed to 633 nm HeNe laser light. Each defect is best seen at a different microwave power.

Temperature is an important parameter the user can control while operating the EPR spectrometer. With the helium-gas-flow system, the sample temperature can be

controlled anywhere from 300 K to 5 K. Often times, EPR signals are broadened at higher temperatures; the EPR signals sharpen (the line width decreases) and the intensity increases as the sample is cooled. This effect is related to the temperature dependence of the spin-lattice relaxation time. There is another even more general effect of temperature. An EPR signal is proportional to the difference in population for the two spin states participating in the transition. The paramagnetic defects (i.e., spin systems) are independent and thus Boltzmann statistics apply. As a result, the difference in population will increase as the temperature decreases. This means that the intensity of an EPR signal increases when the temperature is lowered. Specifically, the signal intensity varies as $1/T$ for a fixed concentration of defects [30]. For the two reasons just described, many EPR spectra are acquired in the 30-50 K range.

The concentration of defects contributing to an $S = 1/2$ EPR spectrum can be estimated. Equation 3.2 provides an empirical relationship for extracting the concentration N from a spectrum [33]. In this equation, ΔW is the line width of the EPR signal in gauss, S/N is the signal-to-noise ratio, T is the temperature in degrees Kelvin, and V is sample volume in cm^3 . The # of lines refers to the hyperfine patterns with multiple lines.

$$N = (5 \times 10^5 \text{ spins})(\Delta W)^2 \left(\frac{S}{N}\right) \left(\frac{T}{10}\right) \left(\frac{1}{V}\right) (\# \text{ of lines}) \quad (3.2)$$

Magnetic field values that the EPR spectrometer records using a Hall field sensor must be slightly corrected (by a few gauss) to reflect the true magnetic field value at the sample position. The Hall probe is located on one magnetic pole cap which is several centimeters away from the center of the magnet. The sample cavity is placed so that the

sample location inside the cavity is as close to the center of the magnet as possible. Because the Hall probe is not measuring the field at the sample, a separate Gaussmeter probe is placed next to the cavity, as close as possible to the sample position. This movable probe uses nuclear magnetic resonance (NMR) of protons to accurately measure the magnetic field. Bruker provides a calibration file that corrects Hall field measurements to the NMR probe measurements [32].

Verification of this calibration file for the magnet in Dr. Giles' EPR lab is presented in Figure 3.4. These data were fit to two functions, with the transition from a linear fit to a quartic fit occurring at 10,000 G. Equations 3.3 are the results of the two fittings. For the EPR spectra studied in this dissertation, all magnetic field values for the defects are below 10,000 G, so only the linear expression in Equation 3.3 was necessary to correct the magnetic field positions.

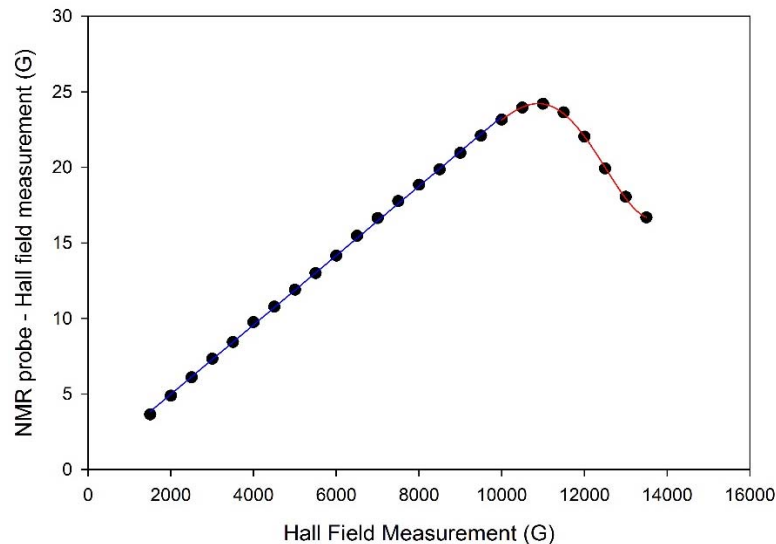


Figure 3.4. The difference in magnetic field measurement between the Hall field vs. NMR probe is shown. A line (blue) was fit to the data from 1500 – 10000 G, and a quartic line (red) was used to fit the data above 10000 G.

$$\begin{aligned}
y &= 0.00229527x + 0.39773306 \\
y &= 1.736364 \times 10^{-13}x^4 - 7.777879 \times 10^{-9}x^3 + 1.288320 \times 10^{-4}x^2 \\
&\quad - 0.9357808x + 2539.263
\end{aligned}
\tag{3.3}$$

3.3 Principles of Optical Absorption

When light is incident upon an optical material, the light may interact with the material in one of three ways: the light is either reflected, transmitted, or absorbed. When the light is absorbed, that means that the frequency of the light resonates with the frequency of the atoms in the material [34]. While this is a property of the bulk material, a similar phenomenon can occur with point defects in the material as well. If there is a defect present in a material, optical absorption measurements associated with defect-related absorption may aid in characterizing the defect when used in conjunction with EPR. In general, when light is absorbed in the material, it is also attenuated, so the amount of light absorbed is dependent on the thickness of the material. Beer's Law, Equation 3.4, describes this attenuation in terms of the absorption coefficient α (z is the depth that the light has traveled into the material).

$$I(z) = I_0 e^{-\alpha z} \tag{3.4}$$

The absorption coefficient (in units of inverse centimeters) is strongly dependent on the wavelength of the incident light, and therefore α is a function of wavelength λ (or alternatively as a function of frequency ν). Additionally, α is independent of the material thickness. When measuring absorption spectra, units of optical density (O.D.) are a more convenient quantity because it includes the material thickness. Also called absorbance,

O.D. can be represented by Equation 3.5 (note l is the total thickness of the material along the light propagation path) [34]:

$$O.D. = \log_{10} \left(\frac{I_0}{I(l)} \right) = \frac{\alpha l}{\ln(10)} \quad (3.5)$$

Even if a material is completely transparent at a particular wavelength (and thus not absorbing any light), not all of the light will necessarily transmit through the material. Some of the light is reflected at the front and back surfaces. The total amount of light reflected (represented by R) depends on the index of refraction of the material. The complex index of refraction $\tilde{n} = n + i\kappa$ is defined in terms of the wave vector of light k : $k = (n + i\kappa) \frac{2\pi}{\lambda}$ [34]. Using this definition of the index of refraction, the total reflective loss at a single air/dielectric surface is given by

$$R = \left| \frac{\tilde{n} - 1}{\tilde{n} + 1} \right|^2 = \frac{(n - 1)^2 + \kappa^2}{(n + 1)^2 + \kappa^2} \quad (3.6)$$

When optical absorption spectra are acquired, the reflective losses at both front and back surfaces contribute to a nonzero baseline in the raw data. These reflective losses are subsequently subtracted from the experimental data, thus showing only the true optical absorption measurement of the material. For CSP, because the index of refraction is not constant over all wavelengths [3, 6], Equation 3.6 is applied to the room temperature experimental data using Equation 2.2 for n_o and n_e . Because reflective losses are independent of sample thickness, these losses are reported in O.D. Example O.D. values due to reflective losses of CSP are 0.259 O.D. at 2.5 μm and 0.272 O.D. at 1 μm .

3.4 Fourier-Transform Infrared Spectrometer

Fourier transform infrared (FTIR) spectroscopy uses a Michelson interferometer (beamsplitter, one moving mirror, one fixed mirror), light source, and a detector to measure absorption spectra. Figure 3.5 shows the optical diagram of a basic FTIR spectrometer. The light output from the source is directed through a beam-splitter. Half the light passes through to a fixed mirror, and the other half travels to a moving mirror. The two reflected beams recombine constructively or destructively. The resulting recombined light depends on the optical path difference of the two initial beams. The recombined light then passes through the sample and toward the detector [35]. Because of the varying optical path difference of each recombined wave, the recombined light produces a detector signal that is a mixture of many sinusoids thus producing an interferogram. The Omnic software package provided with the FTIR allows the user to take the Fourier transform of the interferogram spectrum. The resulting absorption spectrum is typically shown as absorption in O.D. vs energy, which is reported in wavenumber units (cm^{-1}).

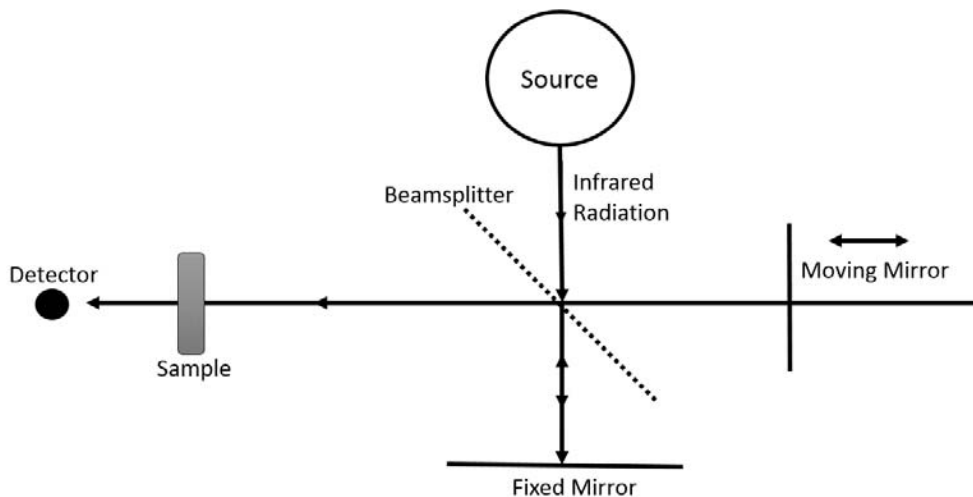


Figure 3.5. Optical Diagram of a Fourier-Transform Infrared Spectrometer.

A Thermo Scientific Nicolet 8700 Fourier-transform infrared spectrometer (FTIR) was used to obtain IR absorption data. Nitrogen gas was used to purge the system to minimize infrared atmospheric absorptions (H_2O and CO_2). This FTIR system at AFIT has three detectors (Si, HgCdTe, and DTGS (deuterated triglycine sulfate), three beamsplitters (CaF_2 , KBr, and quartz), and two light sources (white light, and heated ceramic for IR). Most of the CdSiP_2 measurements reported here were taken in the range from 18000 to 3000 cm^{-1} ($0.560 - 3.33\text{ }\mu\text{m}$) using the white light source, the quartz beamsplitter, and either the Si or DTGS detector. Per manufacturer's specifications, the quartz beamsplitter has an operating capability spanning from 27,000 to 2800 cm^{-1} , the white light source spans from 27,000 to 2000 cm^{-1} , the DTGS detector has an operational range from 12500 to 350 cm^{-1} , and the Si detector operates 27000 to 8600 cm^{-1} . Therefore, a detector changeover was required at approximately $10,000\text{ cm}^{-1}$ (or $1.0\text{ }\mu\text{m}$) to obtain absorption over the visible and near-IR wavelength range that was of interest in the CSP study [36].

Because the FTIR only has a single light path, two scans are required to take a measurement. First, a background scan is performed using the same aperture without the sample to account for any absorption that is due to anything except the sample (such as water molecules in the air or a glass surface). Then a sample scan is performed under the same conditions as the background scan. To measure polarization effects, a wire-grid polarizer is placed in the beam path for both background and sample scans. This process is repeated for each polarization studied. The resulting sample scans are then compared.

For low temperature measurements using liquid nitrogen, a dewar with a "cold-finger" copper plate is used (CryoIndustries model ND 110H) The windows on the dewar

are made of sapphire, which is transparent in both the visible and infrared. The copper plate has two identical apertures on it, so that the sample is mounted over one aperture while the other aperture remains open to allow for a low-temperature background scan. After mounting the sample, the dewar is attached to a vacuum pump to evacuate room air (since room air contains moisture that produces ice) before liquid nitrogen is added to the dewar reservoir. A heater (Lakeshore 335 Temperature Controller) is used to control the temperature of the copper plate from 77 K – 150 K.

3.5 UV/VIS/NIR Spectrophotometer

Similar to the FTIR, a dual-beam absorption spectrophotometer yields an absorption spectrum. Instead of using a single beam of light incident on the sample, a dual-beam absorption spectrophotometer uses two beams. One beam serves as a reference beam where no sample is present in the beam path. The other beam of light passes through the sample. Figure 3.6 shows a diagram of the dual-beam spectrophotometer. In general, there is a lamp that produces light in the ultraviolet, visible, or near-infrared ranges of the electromagnetic wave spectrum. A monochromator isolates a narrow range of frequencies of light, which then gets sent to a chopper. The light is split at the chopper in an alternating fashion, where one beam is sent to the sample arm while the other is sent to the reference arm. Both beams are then directed toward the detector. The difference in measurement from the reference and sample beams at the detector yields the absorption measurement [37].

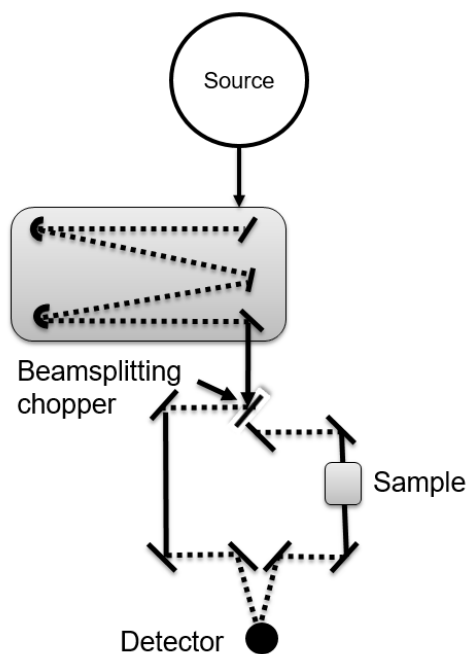


Figure 3.6. Diagram of a dual-beam absorption spectrophotometer.

The specific dual-beam absorption spectrophotometer used for this dissertation is the Cary 5000, which has an operating range that extends into the UV and near IR (175 to 3300 nm). The Cary 5000 has two sources and two detectors depending on the range over which absorption is being measured. For wavelengths longer than 800 nm, the lead sulfide detector is used; for wavelengths shorter than 800 nm, the photomultiplier tube (PMT) is used. An incandescent bulb is used for the visible and near-IR wavelengths; for wavelengths less than 350 nm, a deuterium lamp is used to produce UV wavelengths. The chopper is divided into three parts – one which allows light to pass straight through (toward a mirror that directs the beam toward the reference arm), a mirror which sends the beam to the sample arm, and an opaque section which allows the detector to be in an “off” or no light setting, thus allowing for more accurate signals at each data point [38].

Chapter 4. Previous Studies of Point Defects in ZnGeP_2 , CdSiP_2 and $\text{Sn}_2\text{P}_2\text{S}_6$

CdSiP_2 (or simply CSP) has a tetragonal crystal structure; it is a II-IV-V₂ chalcopyrite that is derived from the III-V zincblende structure [8]. ZnGeP_2 (or ZGP), a well-studied material with a very similar crystal and energy band structure, is described here because it is most similar to CSP in terms of not only crystal structure but because it shares the same intended use in infrared countermeasures as part of an optical parametric oscillator device that operates in the mid-infrared [1]. Because of similar crystal structures [10], the EPR signals for known defects are expected to be similar between CSP and ZGP, although the thermal stability of those defects may differ. Just as the EPR signals for analogous defects are expected to be similar, optical absorption spectra may bear some similarities. This chapter describes the relevant point defect research on ZGP and on CSP using predominantly EPR and optical absorption measurements to identify defects and correlate those defects to optical absorption bands.

This chapter also describes the previous research on $\text{Sn}_2\text{P}_2\text{S}_6$ (or simply SPS), which is a photorefractive material. Section 4.3 details three native defects that have been previously identified in SPS using EPR. The final section reviews research that had been done on Sb-doped SPS. Antimony is of particular interest because it can occupy multiple sites in the SPS crystal. Similarly, tellurium in Te-doped SPS can also occupy multiple sites. Therefore, Sb-doped SPS can be directly compared to Te-doped SPS, which is a primary material studied as part of this dissertation.

4.1 Zinc Germanium Diphosphide

ZGP is a nonlinear optical material very similar to CSP [8]. Its primary application is optical parametric oscillators (OPO) operating in the mid-infrared [1]. There are, however, unwanted absorption bands in the 1-2 μm region that hinder ZGP performance as an OPO material [39-40]. The crystal is tetragonal with $a = 5.46 \text{ \AA}$ and $c = 10.71 \text{ \AA}$ [41]. Point defects in ZGP have been extensively studied using optical absorption, luminescence, and EPR methods [39-45]. More specifically, EPR was used to identify point defects in paramagnetic charge states and correlate those particular defects with optical absorption bands. Since 1994, multiple characterization tools were used to study ZGP defects such as EPR and FTIR.

As-grown ZGP exhibits an EPR signal that has been associated with the singly ionized zinc-vacancy (V_{Zn}^-), an acceptor [39-40]. The doubly ionized charge state is not paramagnetic. This signal contains three lines with intensity ratios of 1:2:1, and the EPR signal can be clearly seen at 20 K. The line intensity ratio is due to a $S = 1/2$, two $I = 1/2$ spin system. Rakowsky et al. [39] in the initial study determined that this three-line EPR spectrum was either due to a zinc vacancy or a zinc-on-germanium antisite. Halliburton et al [40] concluded that this EPR spectrum was indeed due to the zinc vacancy rather than the antisite. Another characterization method, electron nuclear double resonance (ENDOR) spectroscopy, was used to identify the defect.

Later research also identified two donors by photoinducing an EPR signal [41-42]. The conditions for identifying the donor defects were, however, different than for identifying the zinc vacancy acceptor. Both defects produced EPR spectra under illumination with a 633 nm HeNe laser. One of these defects, a neutral phosphorus

vacancy, a donor, can be easily seen at 8 K. This donor was identified through a process of elimination. First, the large number of spins in the donor EPR signal suggests that a native defect is responsible for the signal rather than an impurity (impurities typically produce smaller signals than native defects). Additionally, the defect could not have been the phosphorous-on-germanium antisite because large hyperfine lines due to phosphorus would be expected (and the observed signal exhibits no hyperfine lines) [41]. Germanium vacancies were eliminated because the crystal was known to have been grown with excess germanium. Because the crystal is compensated, that leaves only two possible defects: the phosphorous vacancy and germanium-on-zinc antisite. The observed paramagnetic defect is required to be in a neutral charge state, and prior to illumination with the HeNe laser, the donor is in a nonparamagnetic state which must be singly ionized. The antisite was ruled out because it was expected to be in a singly ionized state when under illumination. Thus, the defect observed was likely due to a phosphorus vacancy.

The other observed donor, the singly ionized germanium-on-zinc antisite, can be seen by illuminating the crystal with 633 nm HeNe laser and subtracting out known signals due to other defects. A “lights-off” spectrum was taken, then a “lights-on.” A new signal appears when the sample is illuminated. By subtracting the “lights-off” spectra from the “lights-on” spectra, the three-line EPR signal for the antisite (with line intensity ratios of 1:2:1) now becomes evident [42].

Once the defects have been identified using EPR and ENDOR techniques, the next logical step is to associate those defects with optical absorption bands [43-44]. Figure 4.1 (left) shows the optical absorption data of various ZGP samples. The data was collected at

room temperature. A clear band appears at 1 μm for all sample, albeit of varying intensities. An EPR study of all samples indicated a singly ionized zinc vacancy, as predicted from previous studies. However, the intensity of the zinc vacancy EPR signal was then plotted against the absorption coefficient of each sample at 1 μm for o-polarized rays. Figure 4.1 (right) also shows the clear correlation between absorption coefficient at 1 μm and the EPR concentration of the singly ionized zinc vacancy. Thus, the singly ionized zinc vacancy was identified as the dominant defect contributing to the increase in 1 μm absorption. For its application as an OPO, this means ideal ZGP crystals will minimize zinc vacancies [43].

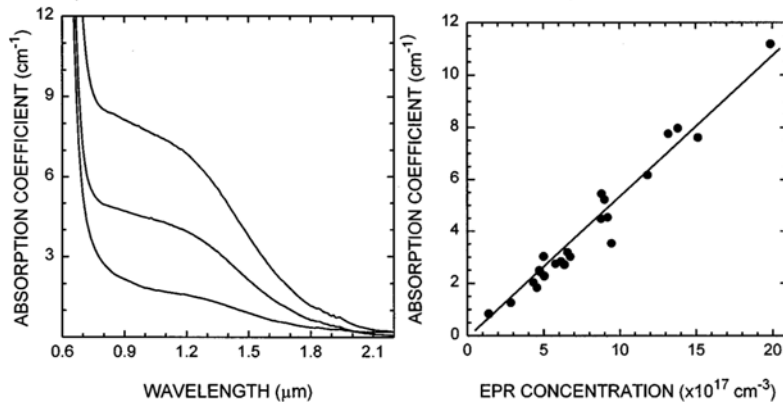


Figure 4.1. Optical absorption data for various ZGP samples (left). The V_{Zn}^- was identified as the defect responsible based on EPR signal intensity of the defect correlated with the absorption coefficient at 1 μm . Reproduced from [43] with permission from AIP Publishing.

4.2 Cadmium Silicon Diphosphide

4.2.1 Native Defect and Impurity Identifications

The native defects of CSP (silicon vacancies, cadmium vacancies, phosphorus vacancies, and silicon-on-cadmium antisites) have been identified via EPR in reference [8]. For the cation vacancy defects, only the silicon and cadmium vacancies that are in the 1– charge state can be monitored with EPR. Both of these defect types are acceptors in CSP.

For the silicon vacancy, the unpaired electron spin is shared among 4 neighboring phosphorus atoms. Because phosphorus has $I=1/2$, this leads to 5 lines in the spectra with intensity ratios of 1:2:3:2:1. Similarly, for the cadmium vacancy the unpaired spin is shared between two phosphorus atoms. This leads to a 3 line spectra with intensity ratios of 1:2:1. The silicon-on-cadmium antisite (Si_{Cd}^+) is a donor. The EPR signal for this defect is a three line spectrum (similar to the V_{Cd}^- EPR signal) due to the unpaired spin shared equally between two nearby phosphorus atoms. The phosphorus vacancy EPR signal (V_{P}^0) is a single line due to the unpaired spin shared with nearby silicon and cadmium atoms (most of which have isotopes that are $I = 0$).

Other native defects that have been identified include a P_{Si} antisite lattice defect. The EPR signal of this defect is characterized by a 1:4:6:4:1 line intensity ratio similar to the silicon vacancy. There is an additional splitting where the five-line spectrum is split into two parts which is due to the unpaired spin being shared with an additional phosphorus atom (100% abundant $I=1/2$) on the silicon site. The EPR signal associated with the P_{Si} (also denoted as P^{4+}P_4) is thus two sets of five lines with line intensities of ratios 1:4:6:4:1. Additional lines are also present between the two sets of five lines; the weak lines in the center are due to manganese, and the low-field P_{Si} are overlapping with another unknown signal. The five-line V_{Si}^- signal is also apparent in the center of the EPR spectrum [46].

One important impurity that appears in every CSP sample studied in this dissertation is iron. Kaufmann et al. [47] characterized several iron charge states found in CSP by studying heavily-doped samples. A few charge states of iron were found in the BAE-grown samples and were easily seen, such as Fe^+ and Fe^{3+} [8] Other charge states of

iron are not as easily seen in the BAE samples, but under the right conditions (temperature, microwave power, etc) small EPR signals that resemble iron are sometimes visible.

4.2.2 Optical Properties of CSP

Following the example from ZGP, Giles et al. [48] explored the correlation between optical absorption and EPR signal intensity for a particular defect. Notably, the absorption coefficient was clearly dependent on whether o- or e-polarized light was incident on the sample during measurement. The absorption band intensity also showed a clear dependence on temperature in one sample (24A) while E was parallel to the c axis. Both of these images are shown in Figure 4.2. Giles et al. [48] concluded that the 1.75 μm absorption band is associated with Fe^{2+} ions, and that this unwanted absorption band may negatively affect CSP performance as a nonlinear material.

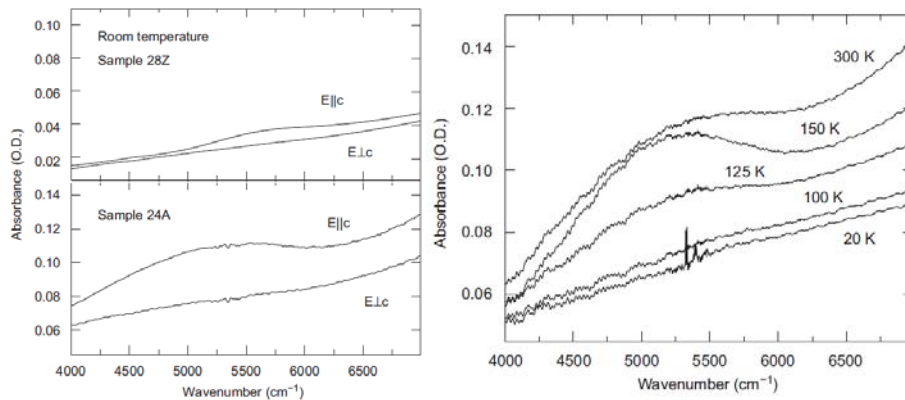


Figure 4.2. Optical absorption data of two CSP samples at room temperature shown using both o-and e-polarized light (left). Also shown is one sample (24A) with E parallel to c-axis at various temperatures. Reproduced from [48] with permission from Elsevier.

4.3 Tin Hypthiodiphosphate

Three native point defects in $\text{Sn}_2\text{P}_2\text{S}_6$ crystals have been fully characterized with EPR. These are the tin vacancy, the sulfur vacancy, and the holelike small polaron [14, 22, 49]. The vacancies are introduced during growth and are initially in nonparamagnetic states, with the tin vacancies being doubly ionized acceptors ($\text{V}_{\text{Sn}}^{2-}$) and the sulfur vacancies being doubly ionized donors (V_{S}^{2+}). If the crystal is grown tin deficient, then significant concentrations of tin vacancies may be present. Conversely, a significant concentration of sulfur vacancies may be present in crystals grown sulfur deficient. Both vacancies can be converted to their paramagnetic charge state (and thus become observable with EPR) when the sample is illuminated with 633 nm light from a HeNe laser while the crystal is at a sufficiently cold temperature (below 90 K). The sulfur vacancies will trap an electron and becomes singly ionized donors (V_{S}^+) and the tin vacancies will trap a hole and become singly ionized acceptors (V_{Sn}^-).

The EPR spectra from these vacancies exhibit resolved hyperfine lines from two phosphorous nuclei (the ^{31}P isotope is 100% abundance with $I = 1/2$). The two ^{31}P interactions are expected because there are two phosphorous ions in an anionic $(\text{P}_2\text{S}_6)^{4-}$ unit. In general, four lines are expected in the EPR spectrum from inequivalent hyperfine interactions with two $I = 1/2$ nuclei. Figure 4.3 shows the EPR spectra from these vacancies when the magnetic field is parallel to each crystal axes a, b, and c. Both defects exhibit some angular dependence in their spectra, so when the magnetic field is along the a axis, the EPR signals for both defects are overlapping [14, 22].

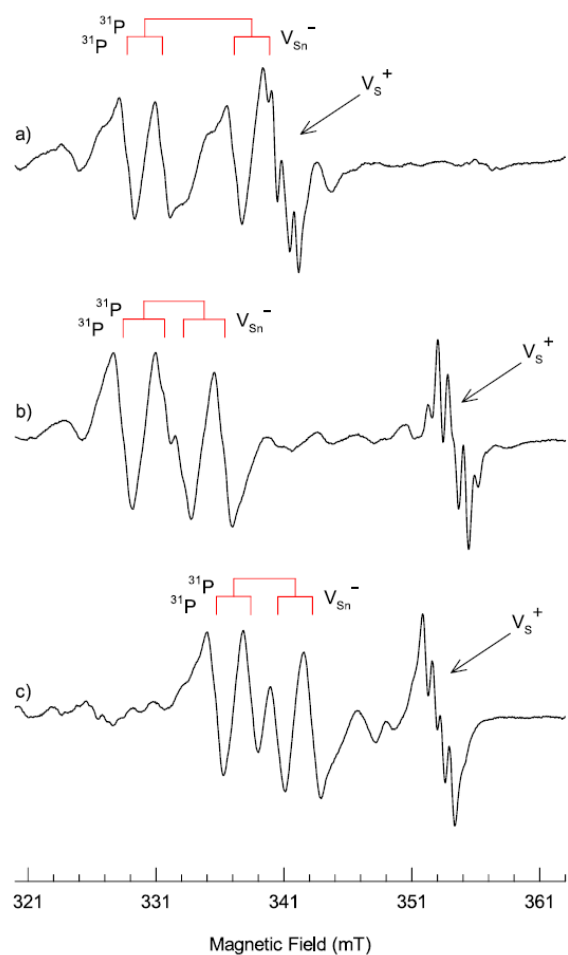


Figure 4.3. EPR spectrum of both the Sn and S vacancies show phosphorus hyperfine. Data taken at 90 K with crystal axis c aligned along the magnetic field. Reproduced from [22] with permission from AIP Publishing.

The EPR spectrum of the sulfur vacancy exhibits magnetic field resonances that vary from 341 mT up to 355 mT depending on the crystal orientation relative to the static magnetic field in the EPR spectrometer. The principal values of the g -matrix for the singly ionized sulfur vacancy are 1.9700, 1.8949, and 1.9006, in the a , b , and c directions, respectively. For this analysis, the a , b , and c crystal directions are all assumed to be

perpendicular to each other. The g values less than 2.0 suggests that this defect is an electron trap [14].

The tin-vacancy with a trapped hole is thus the other defect that exhibits phosphorus hyperfine. The crystals used to obtain the EPR spectra from the Sn -vacancy were intentionally grown Sn deficient using the vertical Bridgman crystal growth technique, thus ensuring that the resulting single crystal will have Sn vacancies. Unlike other SPS crystals that appear to be a deep red color to the eye, these crystals appear orange-red. The EPR spectra for the singly ionized Sn vacancy exhibits angular dependence in all three planes, including site-splitting in the b-c plane. The complete spin Hamiltonian for this defect contains hyperfine terms for two unequal phosphorous interactions. The principal g -matrix parameters are 2.0079, 2.0231, and 1.9717 in the (θ, ϕ) directions $(91.9^\circ, 2.6^\circ)$, $(72.4^\circ, 92.0^\circ)$, and $(17.7^\circ, 278.6^\circ)$, respectively. The hyperfine matrix for the larger phosphorus interaction has principal values of 244.0, 132.8, and 124.3 MHz in the (θ, ϕ) directions $(77.1^\circ, 359.9^\circ)$, $(98.7^\circ, 87.9^\circ)$, and $(15.7^\circ, 144.7^\circ)$, respectively. Similarly, the A hyperfine matrix for the smaller phosphorus interaction is 87.5, 82.5, and 67.7 MHz in the (θ, ϕ) directions $(69.3^\circ, 74.2^\circ)$, $(116.0^\circ, 153.6^\circ)$, and $(34.2^\circ, 197.8^\circ)$, respectively [22].

The third native defect that can be formed in $\text{Sn}_2\text{P}_2\text{S}_6$ crystals is the intrinsic holelike small polaron. Before illumination below 50 K, the Sn ions are present as Sn^{2+} ions. Upon illumination with a 633 nm light from a HeNe laser, a portion of the Sn^{2+} ions trap a hole and become Sn^{3+} ions. The EPR spectrum from this small polaron consists of a large $I = 0$ center line and two smaller $I = 1/2$ lines symmetrically spaced around the center

line. The two smaller lines are assigned to ^{117}Sn , which is 7.68% abundant in nature, and ^{119}Sn , which is 8.59% abundant. All other naturally occurring isotopes of tin are $I = 0$.

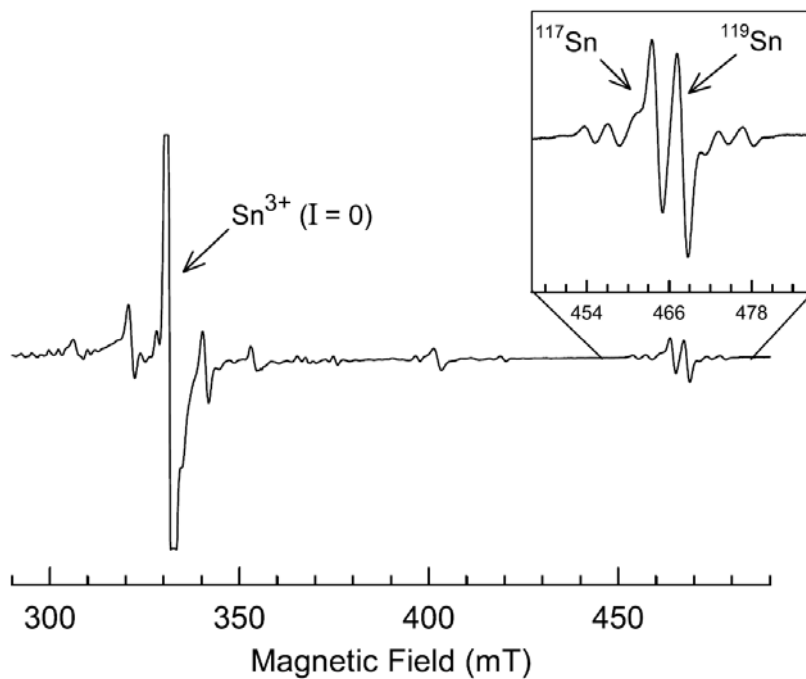


Figure 4.4. EPR spectrum of the small polaron (Sn^{3+} ions) in a $\text{Sn}_2\text{P}_2\text{S}_6$ crystal. The spectrum was taken at 90 K with the magnetic field along the crystal b axis. Reproduced from [49] with permission from IOP Publishing.

4.3.1 Sb-doped SPS

SPS crystals doped with antimony exhibit two distinct photoinduced EPR spectra. One spectrum is due to substitutional Sb^{2+} ions on the Sn site with no other defects nearby. When the sample is illuminated with either 633 or 442 nm laser light at 30 K, the Sb^{3+} ions trap an electron and become Sb^{2+} ions. The resulting EPR spectrum exhibits well-resolved hyperfine lines due to interactions with ^{121}Sb and ^{123}Sb nuclei. The ^{121}Sb nuclei are 57.2% abundant with $I = 5/2$ and the ^{123}Sb nuclei are 42.8% abundant with $I = 7/2$. Similar to

other defects in SPS, the EPR spectra for Sb^{3+} exhibits site-splitting in two planes (a-b and b-c planes). The site-splitting phenomena occurs when the \mathbf{g} and \mathbf{A} matrices do not have a principal direction perpendicular to the mirror plane (b-axis) of the crystal. In this case, there are two crystallographically equivalent but magnetically inequivalent Sb sites, which subsequently gives rise to two EPR lines present in the spectra. As expected, no site splitting is seen in the a-c plane, which is also the mirror plane. The principal g values for this defect have been determined to be 1.810, 1.868, and 1.887 in the (θ, ϕ) directions $(68.7^\circ, 218.6^\circ)$, $(49.6^\circ, 109.2^\circ)$, and $(48.0^\circ, 329.2^\circ)$, respectively. The \mathbf{A} hyperfine matrix for the ^{121}Sb nuclei is 1404, 1687, and 1849 MHz in the (θ, ϕ) directions $(34.7^\circ, 213.0^\circ)$, $(121.9^\circ, 187.3^\circ)$ and $(77.9^\circ, 104.9^\circ)$, respectively [29].

In addition to the isolated Sb ions, there are Sb^{3+} ions located adjacent to a Sn vacancy in the $\text{Sn}_2\text{P}_2\text{S}_6$ crystals. In the as-grown crystal, this defect complex has effective negative charge. When the sample is illuminated with 633 nm HeNe laser light at temperatures below 150 K, this defect complex traps a hole. It becomes an overall neutral complex $(\text{Sb}-\text{V}_{\text{Sn}})^0$ and is paramagnetic with $S = 1/2$. The EPR spectrum for this defect complex shows the characteristic ^{121}Sb and ^{123}Sb hyperfine along with hyperfine from two ^{31}P nuclei with 1:2:1 intensities. The model assigned to this defect has the hole primarily localized on the $(\text{P}_2\text{S}_6)^{4-}$ anionic unit next to the Sb^{3+} ion and Sn^{2+} vacancy. The g -matrix principal values for this defect pair are 1.850, 1.888, and 1.925 in the (θ, ϕ) directions $(91.4^\circ, 241.6^\circ)$, $(125.1^\circ, 332.5^\circ)$, and $(35.1^\circ, 329.6^\circ)$, respectively. The Sb hyperfine \mathbf{A} matrix has principal values of 1153, 1473, 1679 MHz in the (θ, ϕ) directions $(117.0^\circ, 234.4^\circ)$, $(86.6^\circ, 146.1^\circ)$, and $(152.8^\circ, 62.7^\circ)$, respectively. Figure 4.5 shows EPR data on

Sb doped SPS crystals depicting both the trapped-hole and trapped-electron spectra [27].

The model that depicts the Sb-related hole and electron traps is shown in Figure 4.6.

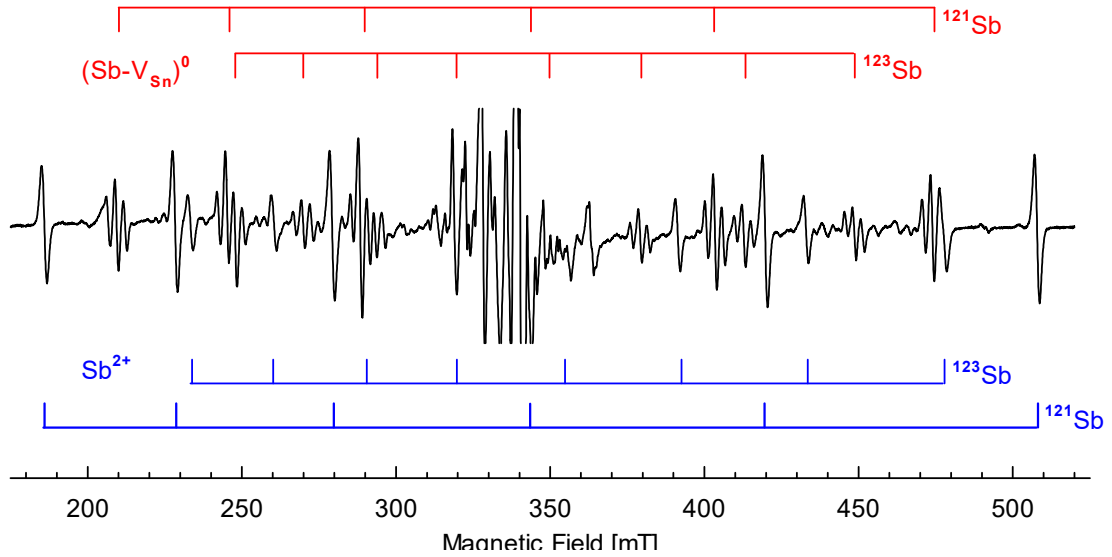


Figure 4.5. EPR signals from Sb-doped SPS samples shown. The red stick diagrams depict the lines for the trapped hole while the blue stick diagram shows the trapped electron. Reproduced from [27]. © 2016 Optical Society of America

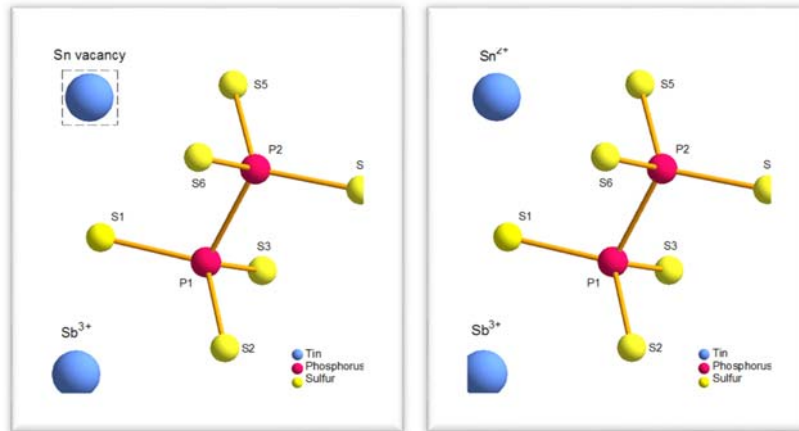


Figure 4.6. The left image shows the hole trap model that corresponds to the red stick diagram. The right image shows the electron trap that corresponds to the blue stick diagram. Reproduced from [27]. © 2016 Optical Society of America

Chapter 5. CdSiP₂ Results and Analysis

This chapter describes the results of electron paramagnetic resonance (EPR) and optical absorption experiments on CdSiP₂ (CSP) crystals. The goal of these studies is to identify specific point defects that may have associated optical absorption bands. Two native defects of significant interest are the silicon vacancy acceptor and the silicon-on-cadmium donor, both of which can be monitored in their singly ionized charge states at room temperature with EPR. Intensities of three optical absorption bands were correlated with the presence of the singly ionized silicon vacancies (V_{Si}^-). More recently grown samples exhibited fewer silicon vacancies. Additional defects including silicon-on-phosphorus antisites, cadmium vacancies, and copper and carbon impurities were present in the CSP samples. These latter defects, however, are not visible at room temperature and require cooling below 300 K in order to observe their EPR spectra.

5.1 Silicon Vacancies and Associated Optical Absorption

Following the example of the previous EPR and optical absorption correlation studies in ZnGeP₂ [42], a comparison of EPR and optical absorption data from CdSiP₂ was completed. These results are discussed in detail in this section, and they are also published in Optical Materials Express [50]. A set of eight CSP samples were selected that had easily measurable photoinduced changes in absorption at room temperature. In this study, 633 nm photons (1.96 eV) from a HeNe laser were incident on the sample, and the absorption spectrum was measured at room temperature using the Cary 5000 spectrophotometer. That spectrum was then compared to the pre-illumination spectrum.

The “light on” spectrum showed a marked increase in absorption in these CSP samples. A “light on” minus “light off” difference spectrum in Figure 5.1 (left side) shows an increased absorption peaking near 800 nm with a shoulder at 1 μm . A separately resolved peak appears in the difference spectra at 1.9 μm . These results are shown in Figure 5.1 (right side) for eight CSP samples.

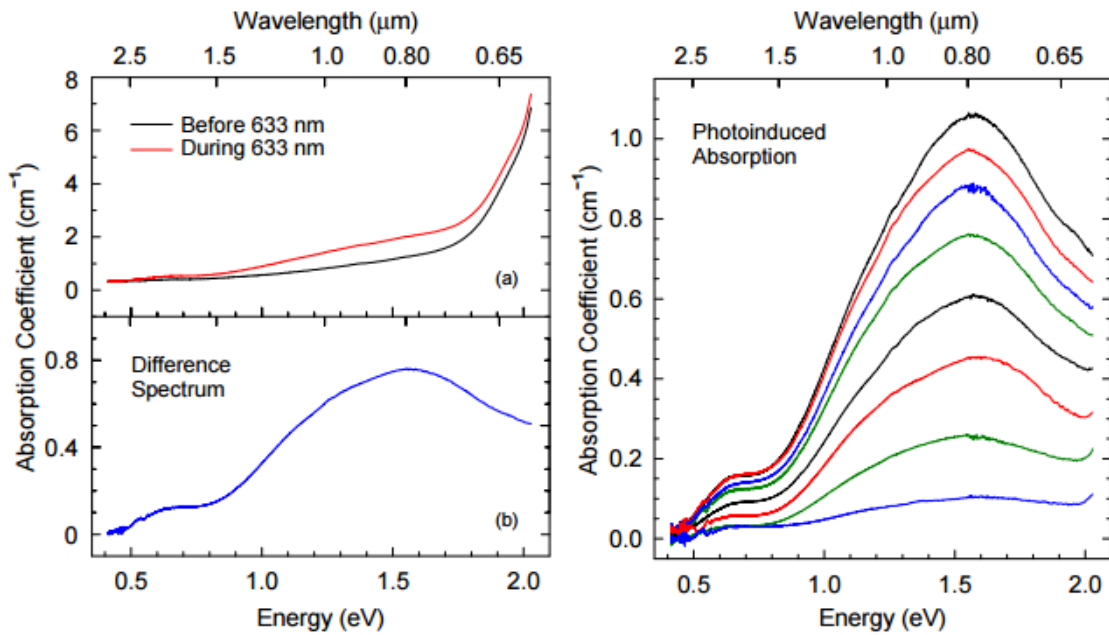


Figure 5.1. Optical absorption from CdSiP₂ at room temperature. Top left shows the optical absorption data before and during illumination with a 633 nm HeNe laser light. Bottom left shows the difference between the “light-on” and “light-off”. The right plot shows the difference curves for eight CSP samples. Reproduced from [50]. © 2017 Optical Society of America

The same experiment was then performed using EPR to monitor the defects. In Figure 5.2, the top EPR spectrum was a “lights-off” measurement and the middle spectrum was a “lights-on” measurement where the sample was continuously illuminated with 633 nm HeNe laser light. The third spectrum is a difference spectrum, i.e., “light on” minus

“light off”. Similar EPR spectra were obtained for each of the eight samples included in Figure 5.1. EPR lines due to Mn^{2+} ($S = 5/2$, $I = 5/2$) are present in the top two spectra, but this ion is not photoactive and does not change when the crystal is illuminated. They cancel and thus do not appear in the “lights-on” minus “lights-off” difference spectrum. The difference spectrum shows only the photoinduced EPR signals. One of these signals is the five-line acceptor spectrum that has been assigned to the singly ionized silicon vacancy (V_{Si}^-) [8]. The singly ionized silicon-on-cadmium antisite donor signal is also present in the difference spectrum, where it appears as a widely split three-line EPR signal. The EPR results for CSP sample 32Z are shown in Figure 5.2, but the other seven samples show similar results.

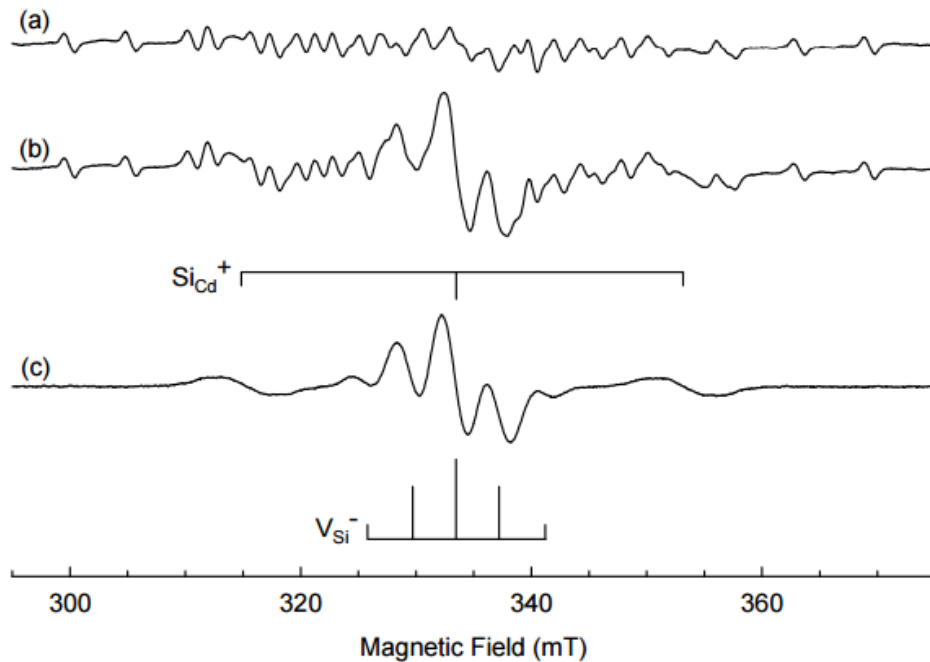


Figure 5.2. EPR spectra at 300 K from CSP sample 32Z. (a) Taken with no illumination. (b) Taken with 633 nm light on. (c) Difference spectrum (“light-on” minus “light-off”). The lowest spectrum shows the silicon-vacancy acceptor and the antisite donor. Reproduced from [50]. © 2017 Optical Society of America

In their doubly ionized charge states, Si vacancies and Si_{Cd} antisites are not paramagnetic. The 633 nm light produces the 5-line EPR spectrum due to V_{Si}^- ($S = 1/2$, as an electron is moved from the silicon-vacancy acceptor to the antisite donor. This suggests that the photoinduced optical absorption is related to the temporary formation of the singly ionized silicon vacancy. While the evidence from one sample is not conclusive, the EPR experiment was repeated for seven additional samples (see the optical absorption spectra for the eight samples in Figure 5.1). A correlation plot of the absorption coefficient at 800 nm vs the EPR concentration of the singly ionized silicon vacancy defect is shown in Figure 5.3 for the eight CSP samples. The EPR concentrations in Figure 5.3 were determined using Equation 3.2.

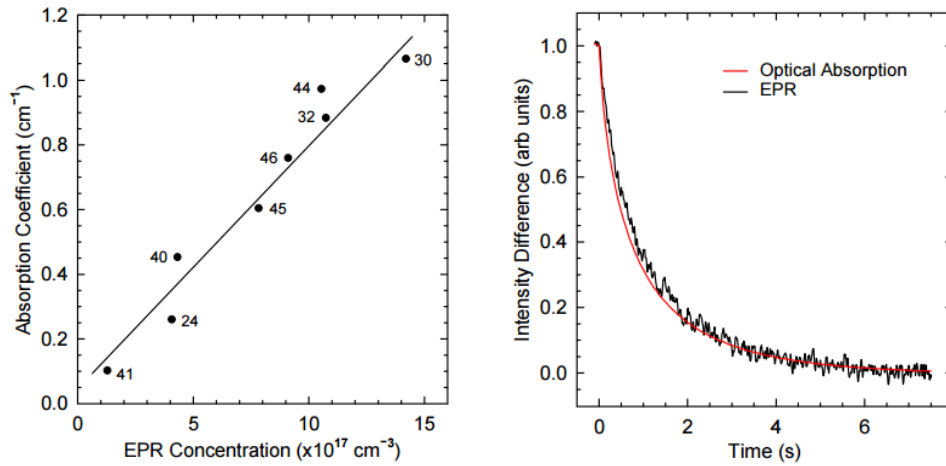


Figure 5.3. Left: Correlation of EPR intensity of V_{Si} signal vs intensity of 800 nm absorption peak. Right: Decay rate of V_{Si} EPR signal and 800 nm absorption peak. Reproduced from [50]. © 2017 Optical Society of America

The photoinduced EPR signal and the photoinduced increase in optical absorption at 800 nm are not stable at room temperature. Upon removing the laser light, both signals

decay immediately. The right side of Figure 5.3 shows the experimental results. The normalized decay of signal intensity for the optical absorption at 800 nm (red curve) and the center line of the five-line singly ionized silicon vacancy EPR signal (black curve) are nearly identical. Together, the production results in Figure 5.1 and the decay results in Figure 5.3 strongly suggest that the photoinduced optical absorption is correlated with the presence of singly ionized silicon vacancies. It is reasonable to conclude that the presence of singly ionized silicon vacancies is responsible for the increase in optical absorption at 800 nm, 1.0 μm , and 1.9 μm at room temperature when CSP crystals are exposed to 633 nm laser light.

In the proposed scenario, most of the silicon vacancies were in a 2⁻ charge state prior to illumination with the 633 nm HeNe laser. Similarly, all of the silicon-on-cadmium antisites are doubly ionized and in the 2⁺ charge state in the as grown crystal. Photons from the 633 nm laser have sufficient energy to move an electron from the valence band to the $\text{Si}_{\text{Cd}}^{+2}$, which then becomes $\text{Si}_{\text{Cd}}^{+}$ after trapping the electron (and seen with EPR). The holes created in the valence band then localize on the silicon vacancies, causing $\text{V}_{\text{Si}}^{2-}$ to change charge state (thus becoming V_{Si}^{-} and seen with EPR). This explains why at the pre-illumination stage there was no visible EPR signal for the silicon-on-cadmium antisite. By trapping an electron, $\text{Si}_{\text{Cd}}^{2+}$ becomes $\text{Si}_{\text{Cd}}^{+}$ which is paramagnetic and produces the three-line EPR spectrum in Figure 5.2.

The nature of the transitions responsible for the room-temperature photoinduced optical absorption bands at 800 nm, 1.0 μm , and 1.9 μm is of interest. The 1.9 μm band is suggested to be consistent with an electron moving from the valence band to the singly

ionized silicon-vacancy acceptor, which would have an energy level at 0.65 eV above the valence band. Based on previous research involving ZnGeP₂ [43-44], the 800 nm (1.55 eV) and 1.0 μm (1.24 eV) bands represent one of two possible transitions: (1) an intracenter transition from the ground state to excited state of the singly ionized silicon vacancy or (2) an acceptor-to-donor transition where an electron moves directly from the singly ionized silicon vacancy to a donor without involving the valence or conduction band.

5.1.1 Discussion on Compensation

Not only did eight CSP samples exhibit a photoinduced optical absorption, five of the eight samples included in this study initially exhibited a stable V_{Si}^- EPR signal at room temperature signal prior to illumination with the 633 nm laser. These five samples also had a non-zero optical absorption at 800 nm, 1.0 μm, and 1.9 μm before illumination. Another CSP sample that is not part of the eight in Figure 5.1 shows a large silicon vacancy EPR signal at room temperature and a large associated 800 nm absorption band, but it does not exhibit any detectable change in absorption upon illumination with the 633 nm laser. This raises the question, “Why do some samples have singly ionized silicon vacancies prior to illumination while other samples do not?” One possible explanation is that the ratio of donor defects (in this case, silicon-on-cadmium antisite) to acceptor defects (silicon vacancies) affects the charge state of the defect in the as-grown crystal. For example, if a sample were to have a one-to-one ratio of donor-to-acceptor defects, both defect types will be in their respective doubly ionized charge state prior to illumination (which is nonparamagnetic). During illumination, an electron from the doubly ionized acceptor will become trapped at the doubly ionized donor site, which subsequently changes the charge

state of both the donor and acceptor to become singly ionized. This change in charge state causes an increase in absorption in the 800 nm, 1.0 μm , and 1.9 μm bands. The total number of defects that changed charge state is proportional to the increase in absorption of the optical absorption bands. This scenario, however, assumes one primary donor and one primary acceptor present in equal concentrations.

On the other hand, if there were twice as many acceptors (V_{Si}) as donors (Si_{Cd}) in an as-grown CSP crystal, then initially the donors will all be in a doubly ionized charge state (nonparamagnetic) while most of the acceptors will be in a singly ionized charge state (paramagnetic). In this case, because all of the acceptors are already in their singly-ionized charge state prior to illumination with the 633 nm laser, there are very few doubly ionized acceptors that can release an electron. Thus, in this case, there would be optical absorption present, but no additional absorption would be photoinduced during an illumination with the 633 nm HeNe laser. This is most likely why I observed one sample to have a large stable silicon-vacancy EPR signal but no photoinduced absorption when illuminated with the 633 nm laser. It may not have many doubly ionized silicon vacancies present in the as-grown crystal because of a reduced amount of donors.

This explanation can extend to the five samples in the silicon vacancy study that had a stable singly ionized silicon vacancy EPR signal before illumination. If the ratio of donors to acceptors is somewhere between 1:1 and 1:2, there will be a silicon-vacancy-EPR signal before illumination. This suggests that the singly ionized silicon vacancy is the more stable defect, and not the singly ionized silicon-on-cadmium antisite donor.

5.1.2 Gaussian Fitting of Optical Absorption Spectra

Additional optical absorption studies were performed on sample 21D at room temperature and compared to the photoinduced spectrum of 30Z. These spectra are shown in Figure 5.4. The photoinduced optical absorption spectrum of sample 30Z requires two Gaussians centered on 1.3 and 1.7 eV (954 nm and 729 nm, respectively) to fit the experimental data, whereas the spectrum for sample 21D, which is the same before and after illumination, can be readily fit with a single Gaussian centered on 1.3 eV. The Gaussian fitting results are also shown in Figure 5.4.

For sample 30Z, which was included in the silicon-vacancy correlation study, the bands at approximately 1 μm and 800 nm are easily seen. For sample 21D, only the 1 μm band is seen. (The 1.9 μm band is present in both samples, but it was not the focus of this specific analysis.) Under these same conditions, EPR measurements show three defects for sample 30Z (silicon vacancies, silicon-on-cadmium antisites, and manganese) and only two defects for sample 21D (silicon vacancies and manganese). These results raise a question about the transition assignment for the photoinduced band peaking at 800 nm. They suggest that the 800 nm band may be due to the presence of singly ionized silicon-on-cadmium antisites, and not simply silicon vacancies as previously reported. Similarly, the 1 μm shoulder is still believed to be due to singly ionized silicon vacancies. These conclusions are tentative, however, because only two samples were compared. Further studies are needed to correlate each absorption band with a particular defect.

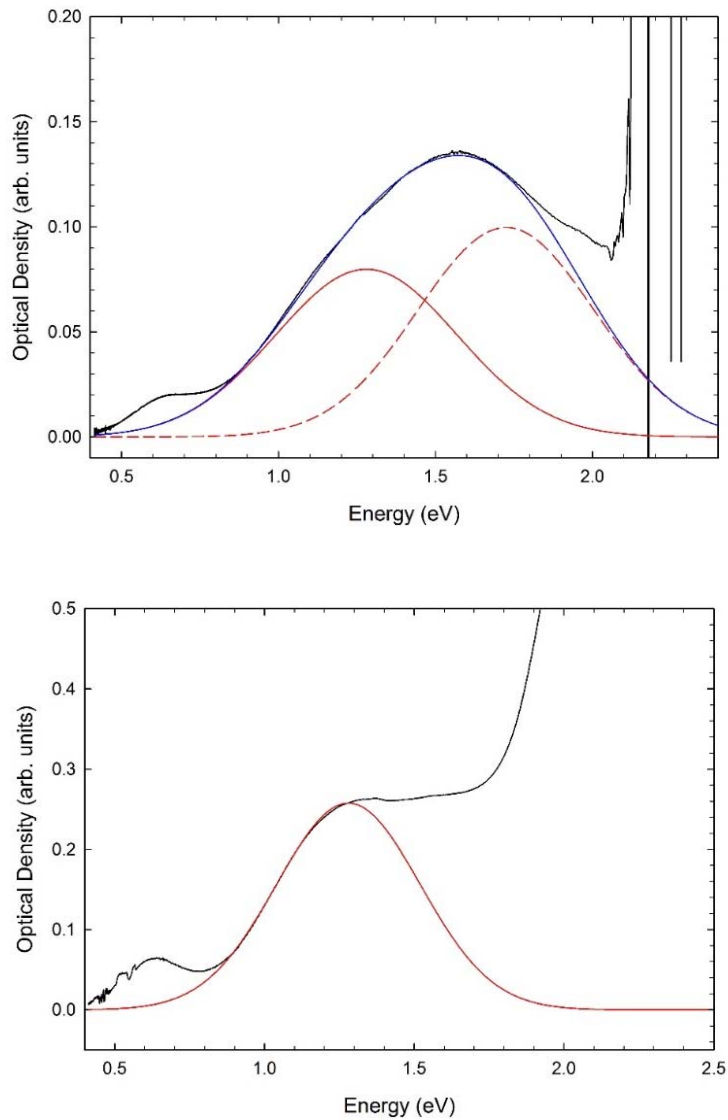


Figure 5.4: Optical absorption spectra from sample 30Z (top) and 21D (bottom). Black curve is optical absorption data, red curves are Gaussian fits. Blue curve (top graph) is the sum of the two Gaussian curves (red).

5.2 Silicon-on-Phosphorus and Copper Acceptors

Two CSP samples had neither a measurable photoinduced optical absorption (due to illumination with a 633 nm HeNe laser) nor a measurable EPR signal due to silicon vacancies. These samples, labeled 47Z and 48Z, however, exhibited a photoinduced

optical absorption at 77 K. The details of the optical absorption spectra are outlined in the next section, but the presence of the photoinduced absorption motivated the search for the responsible defects using EPR. Two new acceptors were identified as a result of my study, which was published in 2018 [51]. The first of these acceptors was a copper atom substituting for cadmium. The second acceptor that was identified was a silicon-on-phosphorus anitsite. The EPR spectrum for each acceptor overlapped the EPR spectrum from the singly ionized silicon-on-cadmium donor, so a series of difference spectra were generated in order to isolate each new signal.

5.2.1 EPR of New Acceptors

First, an EPR spectrum from the CSP sample was collected at 77 K in the dark (before exposing the sample to 633 nm light) with the magnetic field along the c-axis of the crystal. The only defect signal that is easily seen are those due to Mn^{2+} ions, which are not optically active. Then, the sample was illuminated with 633 nm HeNe laser light. Figure 5.5(a) shows this photoinduced spectrum with the pre-illumination spectrum removed, thus eliminating the lines due to Mn^{2+} . After waiting 5 minutes in the dark, the large center line decays. At the same time, the silicon-on-cadmium donor EPR signal also decays at approximately the same rate. An EPR spectrum remains after the large center line and the donor have nearly completely decayed. This remaining spectrum can be seen in Figure 5.5(b) [51].

Figure 5.5(b) shows the EPR spectrum assigned to a copper-on-cadmium acceptor, but a small portion of the silicon-on-cadmium donor signal is still overlapping the new copper signal. Therefore, to isolate the new acceptor signal due to copper, the EPR

spectrum for the antisite donor was first collected separately using very low microwave power. At this low power, the new acceptor signal is still present, but greatly minimized. The low-power spectrum of the silicon-on-cadmium antisite donor is shown in Figure 5.6. This donor signal was removed from the spectrum shown in Figure 5.5(b). Because the two spectra were collected at different microwave powers, a multiplication factor was applied to the donor signal so that the outermost EPR lines of the donor were of equal intensity in both spectra before a subtraction was performed. This procedure ensured that the donor signal was completely removed, leaving only the new copper acceptor signal.

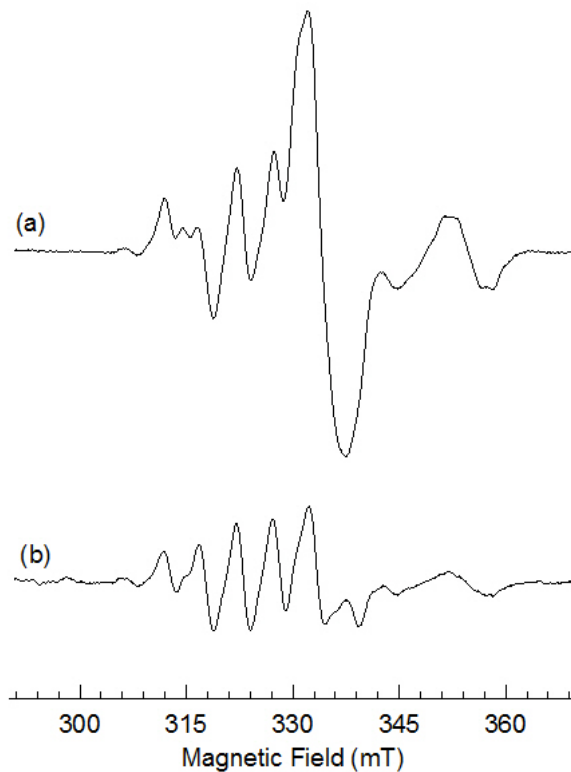


Figure 5.5. Photo-induced EPR spectrum of CSP 47Z (a) during illumination and (b) 5 minutes after illumination while sample remained in the dark. Both spectra were collected at 77 K and with very high microwave power. Reproduced from [51] with permission from AIP Publishing.

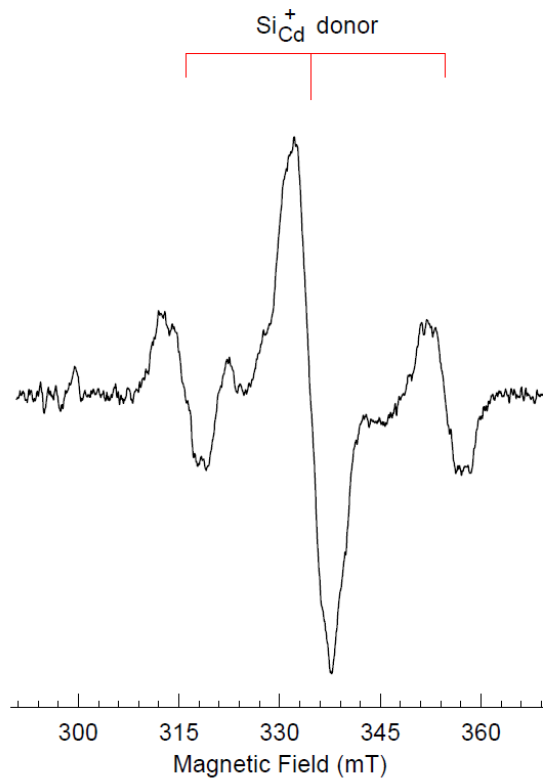


Figure 5.6. EPR spectrum of silicon-on-cadmium anitsite donor. This spectrum was obtained at 77 K using very low microwave power to avoid saturation. Reproduced from [51] with permission from AIP Publishing.

Evidence that the now isolated EPR signal is due to a copper-on-cadmium acceptor is shown in Figure 5.7 (left-a). The EPR signal associated with this defect is an eight-line spectrum with varying line intensities. The eight-line spectrum is due to hyperfine interactions of the copper ion ($I = 3/2$) with the nearest four phosphorus ($I = 1/2$) neighbors results in 20 lines. These lines are strongly overlapping, which results with eight lines with intensities of ratio 1:5:11:15:15:11:5:1 being observed. A simulation using EasySpin was performed to verify the origin of this new EPR signal. The parameters used in the simulation are $g_c = 2.062$, $A_c(^{63}\text{Cu}) = 5.10$ mT, $A_c(^{65}\text{Cu}) = 5.46$ mT, and $A_c(^{31}\text{P}) = 5.10$

mT. The results of the simulation can be seen in Figure 5.7 (left-b). When the sample is rotated such that the magnetic field is along the a-axis, the eight lines collapse to one broad line centered at $g = 2.067$ with a width of 5.0 mT [51].

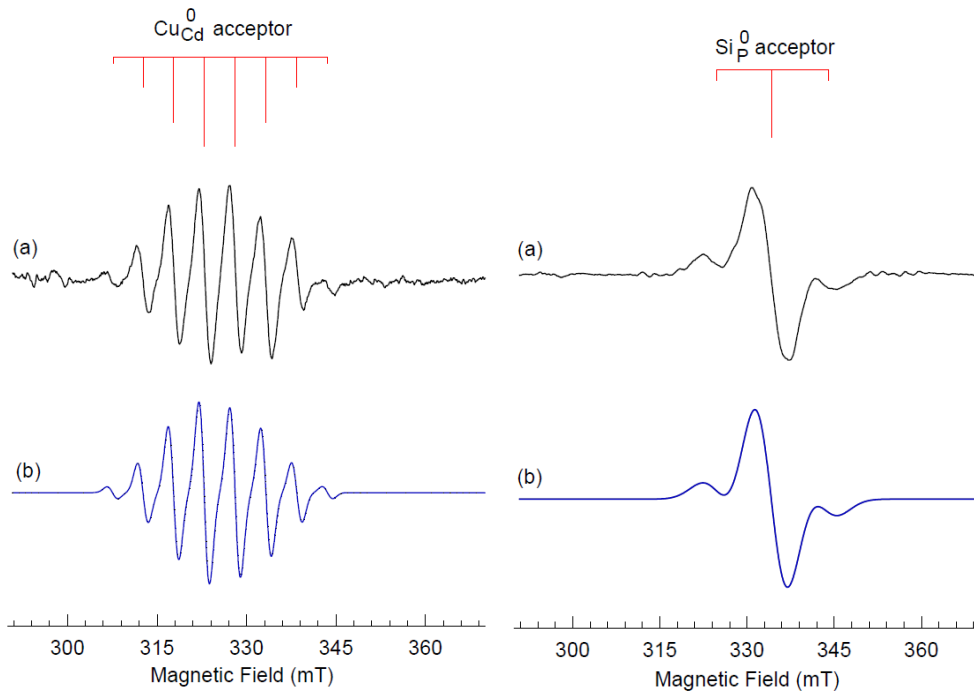


Figure 5.7. EPR spectra of two new acceptors. Left – (a) experimental data and (b) simulation of copper-on-cadmium acceptor. Right – (a) experimental data and (b) simulation of silicon-on-phosphorus acceptor. Reproduced from [51] with permission from AIP Publishing.

A similar analysis is performed to isolate the silicon-on-phosphorus antisite acceptor, which decays within minutes at 77 K after the laser light is removed. Subtracting the bottom spectrum from the top spectrum in Figure 5.5 (so that only the decayed EPR signals can be seen) yields the EPR signal for the silicon-on-phosphorus antisite acceptor along with the silicon-on-cadmium antisite donor. Then the donor signal (silicon-on-cadmium) is removed so that only the isolated silicon-on-phosphorus acceptor EPR signal

remains. This latter spectrum is shown in Figure 5.7 (right-a). The hyperfine pattern in this EPR spectrum, consisting of two less intense lines either side of the main line, is due to the unpaired spin of the silicon-on-phosphorus ($I = 0$) interacting with its two nearest cadmium neighbors (25% of naturally occurring cadmium isotopes are $I = 1/2$, and 75% are $I = 0$). This would predictably result in a large center line with two symmetric lines on each side of the center line that are 1/6 the intensity of the large center line. A simulation was performed of this spectrum using EasySpin to verify the model. The following parameters were used: $g_c = 2.0077$ and $A_c(^{111,113}\text{Cd}) = 16.9$ mT, where $A_c(^{111,113}\text{Cd})$ represents an average of the values for the ^{111}Cd and ^{113}Cd nuclei. The average was used because of the similar magnetic moments of the two isotopes. The simulation verified that the second new signal is indeed consistent with a neutral silicon-on-phosphorus acceptor. The simulation results are shown in Figure 5.7 (right-b) [51].

5.2.2 Optical Absorption at 77 K

As previously stated, some CSP samples have been identified that may not have a measureable silicon vacancy EPR signal, nor the associated absorption band that the singly ionized silicon vacancy causes at room temperature. One of these samples, 47Z, was analyzed at 77 K using the FTIR spectrometer. At room temperature, sample 47Z did not show an increase in absorption when illuminated with the 633 nm HeNe laser. However, at 77 K, two bands were present before any illumination. During illumination, the intensities of these two bands increased. In Figure 5.8, the difference curve (“light-on” minus “light-off”) shows two peaks at 1.4 μm and 800 nm. Another CSP sample, 48Z, also exhibited similar room temperature optical absorption data as 47Z. Neither sample had a

measurable photoinduced effect with the 633 nm HeNe laser at room temperature. Neither sample exhibited an EPR signal associated with the singly ionized silicon vacancy at room temperature. However, both samples have absorption bands at 77 K without illumination, and both samples had increased absorption when the 633 nm laser was on the samples at 77 K. One notable difference, however, was 48Z had a much larger (approximately 3 times larger) absorption than 47Z at 77 K with the laser on. Both samples were studied using EPR to identify differences. A possible correlation may exist between the increase in optical absorption with the 633 nm laser and the silicon-on-cadmium antisite donor and the two new acceptors (copper-on-cadmium and silicon-on-phosphorus).

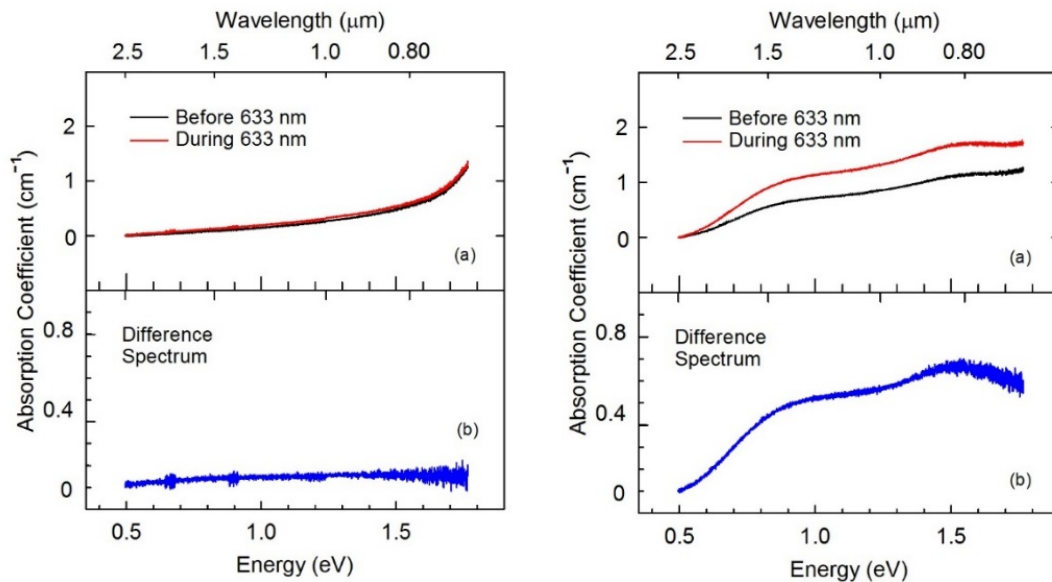


Figure 5.8. Optical absorption spectra from sample 47Z. Left: There is no measurable increased absorption with a 633 nm laser at room temperature. Right: At 77 K, the sample shows a large increase in absorption when illuminated with a 633 nm HeNe laser.

Because the two new acceptors have different thermal stabilities at 77 K, this optical absorption at 77 K was further analyzed at various temperatures. The two absorption bands appear at different temperatures, as shown in Figure 5.9. This suggests that the presence of the two bands are unrelated to each other. An initial hypothesis is that one band is due to the copper-on-cadmium impurity acceptor and the other band is due to the silicon-on-phosphorus antisite acceptor. EPR has shown that the copper defect is much more stable at 77 K than the silicon-on-phosphorus antisite acceptor. This would suggest that the copper acceptor traps electrons at a higher temperature than the antisite acceptor. It is apparent from the data that the 800 nm band emerges at a higher temperature than the 1.4 μm band. Therefore, the data presented in Figure 5.9 suggests that the 800 nm band is due to the copper impurity, and the 1.4 μm band is due to the silicon-on-phosphorus acceptor.

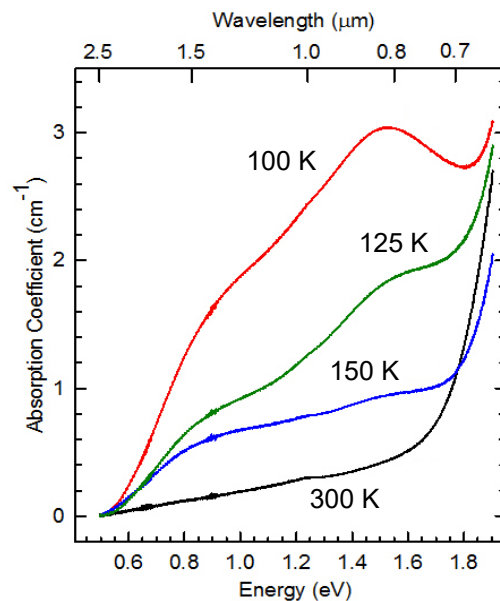


Figure 5.9. Photoinduced optical absorption data from sample 47Z as a function of temperature. Reproduced from [51] with permission from AIP Publishing.

Additional studies were performed using a polarizer. Figure 5.10 shows the results of the optical absorption spectrum collected at 100 K using a polarizer on CSP 48Z, shown in Figure 5.10. In the spectrum, there was a detector change at 1 μm (near 1.3 eV) and the presence of some HeNe laser light is visible near 2.0 eV. (Note that the polarization dependence for sample 47Z is similar, but the absorption bands in sample 48Z are more pronounced, which is why they are shown here rather than 47Z). The overall absorption is much larger when only o-rays (electric field perpendicular to the c-axis) are allowed to pass through the polarizer, and the absorption is minimized when e-rays are allowed to pass through the polarizer. Three distinct bands appear: 1.6 eV, 1.5 eV, and 0.9 eV.

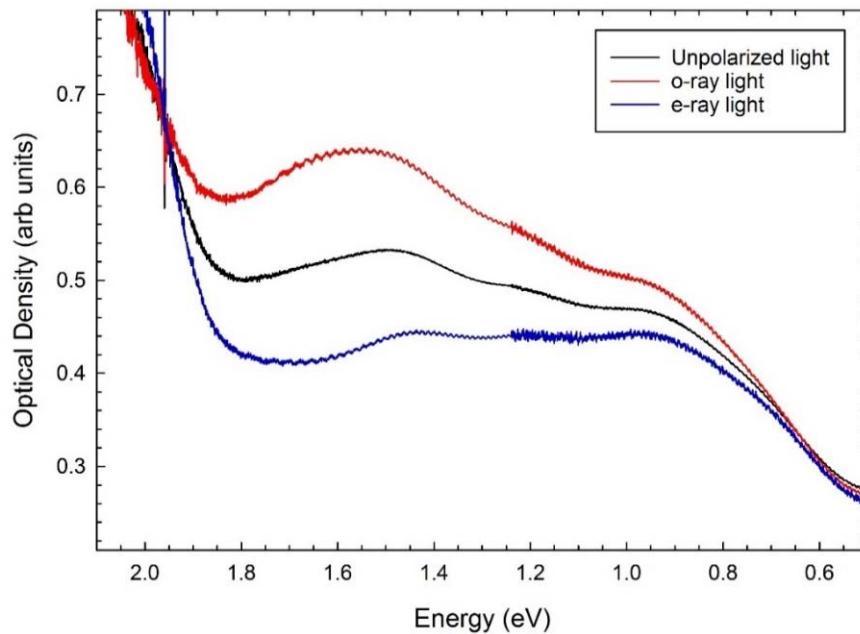


Figure 5.10. Optical absorption spectra from sample 48Z showing the polarization dependence of the photoinduced optical absorption bands at 100 K. There was a detector change at 1 μm (approximately at 1.3 eV). Some of the 633 nm HeNe laser light is present in the spectrum near 2.0 eV.

Notably, the band near 1.6 eV is most strongly affected by the polarizer, and it increases when only o-rays are allowed to interact with the sample. On the other hand, the 0.9 eV band is not affected by the polarization of the incoming light. The preliminary results are inconclusive on the polarization of the 1.5 eV band. Not surprisingly, the overall spectrum collected using unpolarized light is roughly the average of the o-ray polarized and e-ray polarized spectra. This is further evidence that each absorption band is due to a different defect. The polarization dependence of the 1.6 eV absorption band may provide some insight into the responsible defect transition.

Additional optical absorption studies were performed at 77 K. Both CSP samples 47Z and 48Z had no obvious optical absorption at room temperature either with or without illumination from the 633 nm laser. Both samples however, did have photoinduced absorption at 77 K which is tentatively attributed to the presence of the two new acceptors that have now been identified (silicon-on-phosphorus and copper on a cation site). One other feature worth noting is an optical absorption band that does not appear to be photoinduced. Figure 5.11 shows this band, which is found near 610 nm. At room temperature, this feature is not seen because the band edge is located near this wavelength. As the sample is cooled, the band edge shifts to shorter wavelengths, and thus reveals this band. This band is not photoinduced (the photoinduced increase in absorption at 610 nm is due to the tail of the 800 nm band extending to 610 nm). Further studies are needed to identify the mechanism responsible for this absorption band at 610 nm.

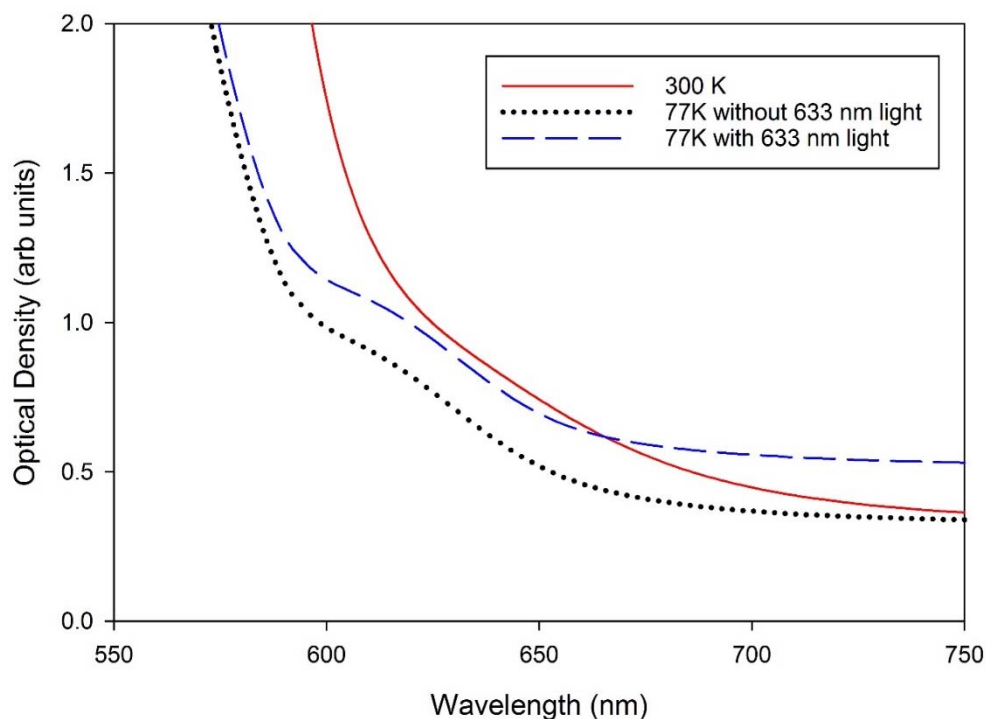


Figure 5.11. Optical absorption spectra from sample 47Z. As the sample is cooled, the band edge shifts to shorter wavelength and reveals an absorption band at 610 nm. The data was taken at room temperature and 77 K

5.3 Carbon-on-Cation-Site Defect

A new, and unexpected, EPR signal was observed in CSP sample 52AA. When the sample is illuminated with 633 nm HeNe laser light at 56 K, EPR spectra from multiple defects are observed when the spectrometer is operated at high microwave power. When the laser light is removed and the sample remains in the dark, EPR signals from two separate defects decay, leaving the familiar EPR signal from the Cu^{2+} acceptors. The EPR signals that decayed can then be isolated by performing a “light-on” minus “light-off” subtraction. This gives the upper (red) spectrum in Figure 5.12. This effectively removes

the EPR signal due to copper which is stable at this temperature. The remaining red spectrum clearly shows the Si-on-Cd antisite along with another signal. The known signal due to the Si-on-Cd is then removed from the red spectrum and only the EPR spectrum due to the new defect remains. This is the lower spectrum in Figure 5.12. The hyperfine structure in this spectrum indicates that the unpaired spin unequally interacts with three neighboring ions, each with nuclear spin $I = 1/2$. In CSP, this strongly suggests interactions with phosphorus neighbors.

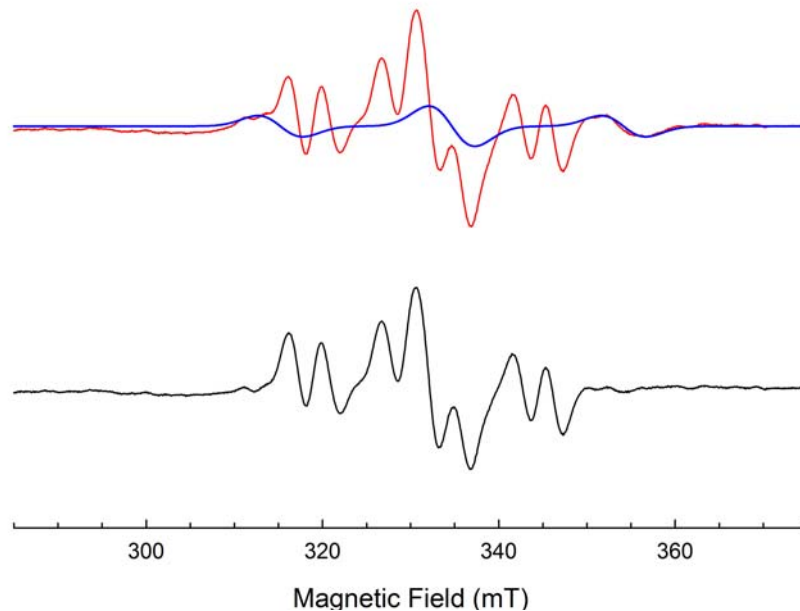


Figure 5.12. The upper spectrum is the photoinduced signal that decayed when the 633 nm HeNe laser was removed (red) and a simulation of the Si_{Cd}⁺ EPR signal (blue). The lower spectrum shows the remaining signal when the Si_{Cd}⁺ signal is removed (i.e., red minus blue).

The presence of an unpaired spin interacting with three (instead of two or four) phosphorous nuclei is unexpected in this material, and suggests that an impurity is present on either a silicon or cadmium site and is significantly smaller than Si or Cd. The unequal

sharing of the electron spin suggests that the impurity ion is small enough that it is able to move slightly within its lattice position (i.e., off-center), causing it to be physically closer to three phosphorus instead of in the middle of four phosphorus atoms. The impurity must also be predominantly $I = 0$ because no hyperfine is seen (except for the three nearest phosphorus neighbors). Carbon is a likely candidate for this impurity. Additional studies are needed to establish a complete model for this new defect.

5.4 Cadmium Vacancies

Recent research on CSP has shown that the singly ionized cadmium vacancy acceptor is not visible using EPR unless the sample is at a very low temperature (15 K or less). Every CSP crystal exhibits an EPR signal from these vacancies, but thus far, there is no information available about optical absorption associated with the cadmium-vacancy acceptors. Future work on CSP needs to remedy this lack of information.

Lifetimes for the cadmium-vacancy EPR signal were measured at various temperatures for 48Z, as shown in Figure 5.13. It is clear that the cadmium vacancy is unstable, and even at 10 K the EPR signal decays within a few minutes. A working theory is that the cadmium-vacancy acceptors and the silicon-on-cadmium antisite donors exchange electrons when the sample is illuminated at very low temperature with the 633 nm HeNe laser. Proving this will be difficult because the cadmium vacancy can only be seen with EPR at 20 K or below, and the antisite is strongly microwave-power saturated at these low temperatures due to long spin-lattice relaxation times.

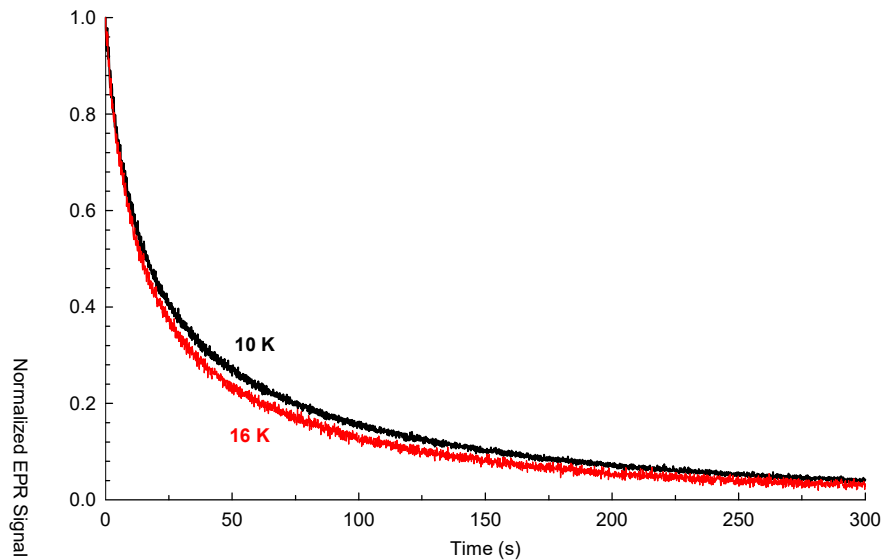


Figure 5.13. Lifetime data from CSP sample 48Z showing the decay of the singly ionized cadmium vacancy. Compared with other defects, the cadmium vacancy is very unstable even at 10 K.

5.5 Neutron-Irradiated CSP

Neutron-irradiated CSP samples may also provide insight into how defects affect optical absorption by creating additional defects that were not previously present in the pre-irradiated crystal. Figure 5.14 shows the FTIR absorption spectrum taken at room temperature for sample 49Z, both pre- and post-neutron irradiation. A large absorption appears from the band edge out to 1 μm that was not present before the neutron irradiation. EPR has not provided any insight as to the identity of the defects causing the large absorption. The 633 nm HeNe laser has no effect on the large absorption, either at room temperature or 77 K.

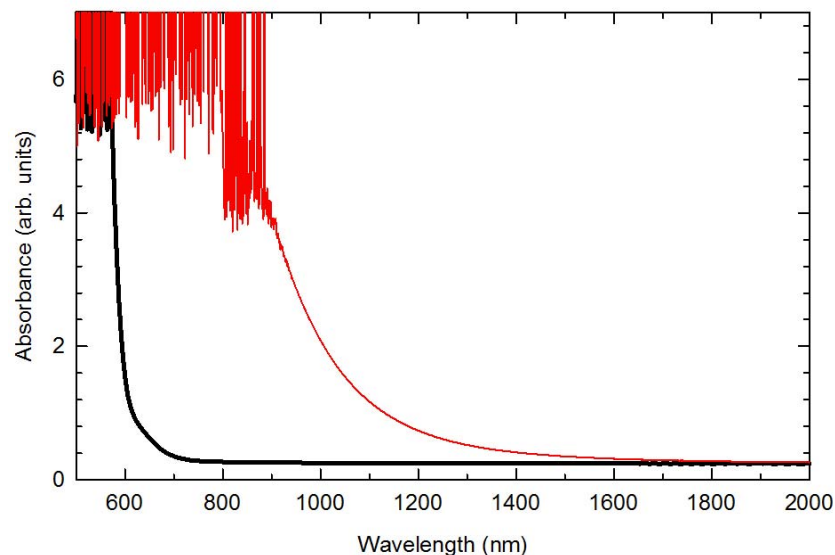


Figure 5.14. Optical absorption spectra from sample 49Z. The black curve is before neutron irradiation and the red curve is after neutron irradiation.

5.6 Effects of 1064 nm Light

In all CSP samples, there are both acceptors and donors that are responsible for photoinduced effects when illuminated with 633 nm laser light at various temperatures. These photoinduced effects can be stabilized, with a very slow decay rate, if the sample is illuminated at a sufficiently low temperature. In the case of the singly ionized silicon vacancy, 77 K is sufficient to maintain a stable photoinduced absorption and corresponding EPR signal. Upon illumination with 1064 nm light, the photoinduced absorption is immediately reduced. This effect is more striking for those samples which had a singly ionized silicon vacancy EPR signal (and associated absorption) at room temperature prior to illumination with a 633 nm laser. In these cases, the EPR signal and associated absorption can be destroyed at 77 K upon illumination with 1064 nm light. This effect,

however, is not observed at room temperature. A similar effect occurs at 77 K with the relatively stable copper impurity EPR signal – it is annihilated with illumination with 1064 nm light.

The silicon-on-cadmium antisite is the most dominant donor in all samples with optical absorption at room temperature and 77 K, but the associated acceptor defect varies from sample to sample. Regardless of the acceptor defect present, all absorption is bleached at 77 K with 1064 nm laser light. This suggests that the bleaching effect of the photoinduced optical absorption with 1064 nm light is due to the presence of the silicon-on-cadmium donor. This further suggests that the donor level is deep since 1064 nm light corresponds to a mid-bandgap energy level. This would also be consistent with the thermal stability of the silicon-on-cadmium donor EPR signal. Because the silicon-on-cadmium antisite EPR signal is produced easily at room temperature, the stability of the singly silicon-on-cadmium antisite donor appears to be dependent primarily on the stability of the associated acceptor (except when the acceptor is the singly ionized silicon vacancy). After illuminating with 1064 nm laser light, the charge state of the silicon-on-cadmium antisite donor is nonparamagnetic. It is either doubly ionized or neutral (since only the singly ionized state is paramagnetic and can be monitored with EPR).

5.6.1 CSP Sample 21D

CSP sample 21D was initially deemed simply an outlier, but further investigation has shown that it may be especially interesting and useful. It merely has different relative amounts of defects than most of the other samples and thus may offer additional clues as to the proposed models for the defects in other samples. At room temperature, sample 21D

shows a large silicon vacancy EPR signal and an optical absorption band peaking at 1 μm (see Figure 5.4). These signals remain the same intensity upon illumination with 633 nm laser light. Therefore, this sample does not exhibit any measurable photoinduced absorption at this temperature. However, at 77 K, it shows a photoinduced absorption. These effects at 77 K are very similar to other samples at room temperature: the singly ionized silicon vacancy EPR signal increases in intensity upon illumination with the 633 nm laser and the silicon-on-cadmium antisite EPR signal appears. Illumination with 1064 nm laser light bleaches all observed EPR signals at 77 K.

A possible explanation for the photoinduced absorption in sample 21D at 77 K, but not at room temperature, requires the Fermi level of the material to decrease as the temperature is lowered. The singly ionized silicon vacancies are decreasing with temperature, but are they becoming doubly ionized or neutral vacancies? Either the electron is moving from the singly ionized silicon vacancy (for example $V_{Si}^- \rightarrow V_{Si}^0$) to a non-paramagnetic donor ($Si_{Cd}^{++} \rightarrow Si_{Cd}^0$) or the electron is moving from the donor to the silicon vacancy acceptor through the conduction band. More data is required to definitively identify where the electron is coming from and moving to upon illumination with the 1064 nm laser.

Chapter 6. $\text{Sn}_2\text{P}_2\text{S}_6$ Results and Analysis

Single crystals of SPS separately doped with tellurium (Te), copper (Cu), or silver (Ag) were investigated. These crystals were supplied by Professor Alexander Grabar at Uzhgorod University in the Ukraine. The majority of the SPS research results described in this chapter are focused on the Te-doped SPS crystals. Seven distinct photoinduced defects were identified in these crystals: five defects that have trapped holes and two defects that have trapped electrons. All five defects with trapped holes are assigned to tellurium ions on sulfur sites in the crystal. One of the defects with a trapped electron is assigned to a tellurium ion on a tin site. The second defect with a trapped electron is assigned to an iodine ion located on a phosphorous site. The presence of hyperfine lines and the anisotropy of the g matrices provided the critical information needed to establish the defect models.

Investigation of Cu-doped SPS crystals revealed a photoinduced EPR spectrum from Cu^{2+} ions located at Sn^{2+} sites. In SPS, these neutral Cu^{2+} acceptors have a filled $3d^{10}$ configuration with the unpaired spin in an outer, more delocalized, hydrogenic orbital, instead of the often occurring $3d^9$ configuration with the unpaired spin in a d orbital. This “classic” acceptor behavior of Cu in SPS is similar to the behavior of Cu in CSP reported earlier (see Section 5.2). Despite Cu and Ag having similar electron configurations (3d versus 4d outer shells), only limited success was encountered in the study of the Ag-doped SPS crystals. Photoinduced EPR lines that may be associated with Ag were observed, but they did not exhibit the expected hyperfine from the ^{107}Ag and ^{109}Ag nuclei. One Ag-related spectrum could be tentatively assigned to Ag^0 atoms at interstitial sites, with

motional effects minimizing hyperfine splittings. A spectrum due to Ag^{2+} ions was not detected.

6.1 Tellurium-Doped $\text{Sn}_2\text{P}_2\text{S}_6$ Crystals

In SPS crystals, tellurium ions may trap an electron or a hole during illumination at low temperature. Which behavior occurs depends on whether the Te ion occupies a Sn^{2+} cation site or a S^{2-} anion site. Tellurium on a tin site will be a Te^{4+} closed shell ion with the $[\text{Kr}]4d^{10}5s^2$ configuration. A Te^{4+} ion will trap one or two electrons when the crystal is exposed to near band-edge laser light and form a Te^{3+} ion or a Te^{2+} ion, respectively. As described later in this section, an EPR spectrum with $S = 1/2$ is assigned to the Te^{3+} ions. The Te^{2+} ions, with a $5p^2$ outer shell, are expected to have either $S = 0$ or $S = 1$, depending on whether the two p electrons align parallel or not. Since an EPR spectrum attributable to Te^{2+} ions has not been seen, it is most likely that a low spin ($S = 0$) ground state is formed.

Tellurium on a sulfur site will be a Te^{2-} closed shell ion with the $[\text{Kr}]4d^{10}5s^25p^6$ configuration. The tellurium ions are less electronegative than the sulfur ions, thus allowing a hole to be trapped on the $(\text{P}_2\text{TeS}_5)^{4-}$ anionic groups in SPS and form $(\text{P}_2\text{TeS}_5)^{3-}$ units. In the regular unperturbed lattice, the $(\text{P}_2\text{S}_6)^{4-}$ anionic groups will not trap a hole at any low temperature. In other words, self-trapped holes associated with the $(\text{P}_2\text{S}_6)^{4-}$ units are not found in SPS crystals. Five photoinduced EPR spectra representing trapped holes have been observed in Te-doped SPS crystals and are assigned to Te on S sites. The five distinct, yet similar, spectra arise because the six sulfur sites in the $(\text{P}_2\text{S}_6)^{4-}$ unit are all

inequivalent. Assuming the Te ions randomly occupy sulfur sites within this unit, then each site occupied by a Te ion will give a different g matrix (specifically, different principal-axis directions for the g matrix) and thus a different EPR spectrum.

6.1.1 Tellurium-Related EPR Spectra

Six EPR spectra, not previously reported, were photoinduced in tellurium-doped SPS crystals. Figure 6.1 shows EPR spectra from an SPS crystal doped with 1% Te. This sample was relatively large, with dimensions of 3 x 3 x 6 mm³. The upper spectrum in Figure 6.1 were taken at 20 K while a 633 nm HeNe laser continuously illuminated the sample. In this spectrum, four strong signals are present between 275 and 400 mT. Each line represents a different defect. One of these (located near 330 mT) has been previously identified as the holelike small polaron [49]. The three remaining strong signals in the upper spectrum in Figure 6.1 are assigned to Te defects. These signals are labeled A, B, and C. Weak ¹¹⁷Sn and ¹¹⁹Sn hyperfine lines are seen at lower and higher fields in the upper spectrum in Figure 6.1. These tin-hyperfine lines were assigned to the separate large lines by comparing the intensities of the hyperfine lines and the center lines at several different temperatures. For example, the intensity of the large EPR line corresponding to defect B increased as the temperature was raised and the tin-hyperfine lines labeled B also increased.

After taking the upper spectrum in Figure 6.1, the laser light was removed and the temperature of the sample was raised to 160 K for 2 min before returning to 20 K where the lower spectrum was taken. The three original A, B, and C defects, present at 20 K, disappeared when the crystal was warmed. This suggests that, upon warming, the charge

states of these three defects changed from paramagnetic to nonparamagnetic. As a result of the thermal anneal, two new EPR lines appear, labeled defect D and defect E. Although formed at higher temperature, these lines are best seen around 20 K. They are too broad to be detected at temperatures above 50 K. As shown in the lower spectrum in Figure 6.1, defect D also has associated tin-hyperfine lines. No tin hyperfine lines were seen with defect E.

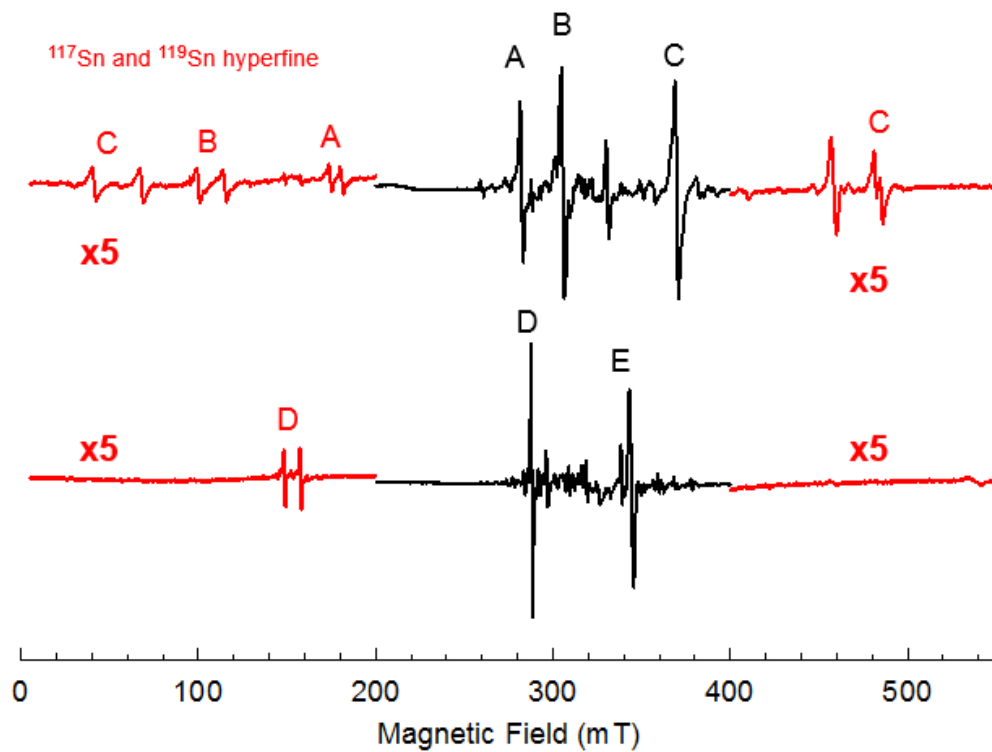


Figure 6.1. EPR data from a Te-doped SPS crystal. The top spectrum was taken at 20 K while 633 nm light was illuminating the sample. The bottom spectrum was also taken at 20 K, after the sample was warmed to 160 K for 2 minutes. The red lines are magnified 5x to show the Sn hyperfine lines. The magnetic field was along the c axis.

To verify that the lines in Figure 6.1 correspond to separate defects, the angular dependence of each large EPR signal was then measured. By rotating the sample in 5 or

10 degree increments about the a axis (i.e., in the b-c plane) with the direction of the static magnetic field fixed, the EPR signals in Figure 6.1 separate into two branches and change magnetic field position. The upper plot in Figure 6.2 shows the angular data for defects A, B, and C, taken at 24 K while the HeNe laser light is on the sample. The lower plot in Figure 6.2 shows the angular data for defects D and E, taken at 24 K after turning the laser off and warming to 110 K for 1 min. The flat black line between 0 and 45 degrees in the top plot represents the small polaron, which does not exhibit any angular dependence [49]. The large g-shifts for these five defects were a surprise. Large swings in g-values are not common for most defects. In the present case, these large shifts are most likely caused by the large spin-orbit coupling associated with the “heavier” tellurium ions.

Angular-dependence data were then collected for all three planes of rotation using other Te-doped SPS crystals. These latter samples were small enough (approximately 2 x 2 x 2 mm³) so that they could be oriented within the EPR cryostat glassware with either a, b, or c directions vertical and thus allow data to be taken in all three planes. Doping levels in these samples ranged between 0.5% and 2.0% tellurium. As expected, the data from these additional crystals were consistent with the results from the physically larger 1% Te-doped crystal, but the intensities of the EPR signals were notably smaller due to the smaller sample size. Complete sets of angular dependence data for each defect (A-E) are shown in Figure 6.3 and Figure 6.4. Data were collected in 5 degree steps from the c-axis to the a-axis. Then the crystal was rotated to collect data in the c-b plane. Finally, data were collected in the b-a plane. In all cases, the measured magnetic field values were corrected using the calibration curve presented in section 3.2.

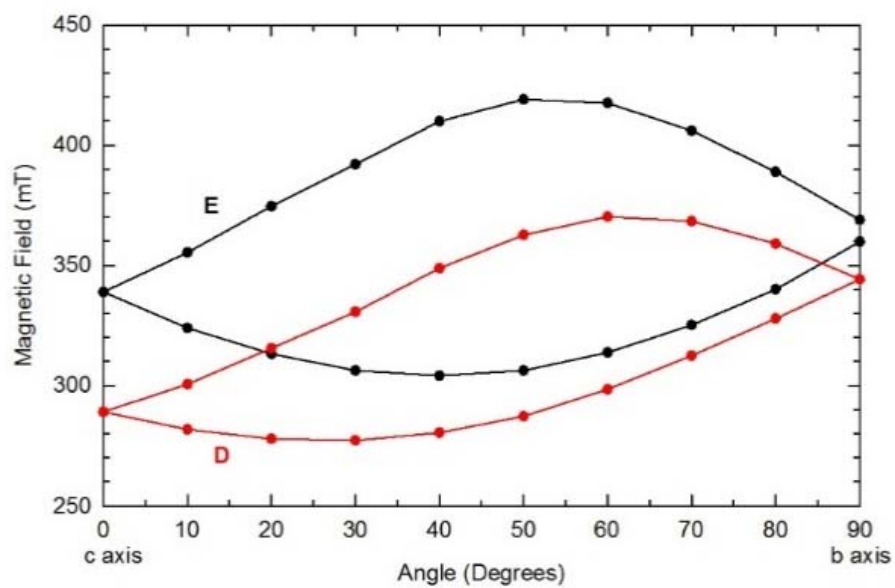
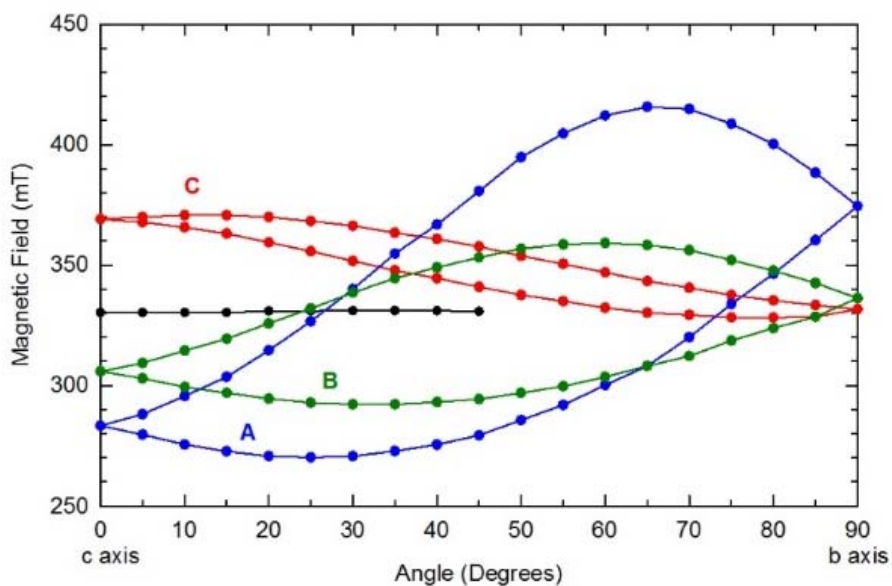


Figure 6.2. EPR angular dependence from a 1% Te-doped SPS crystal. These results show that there are five different defects labeled A, B, C, D, and E.

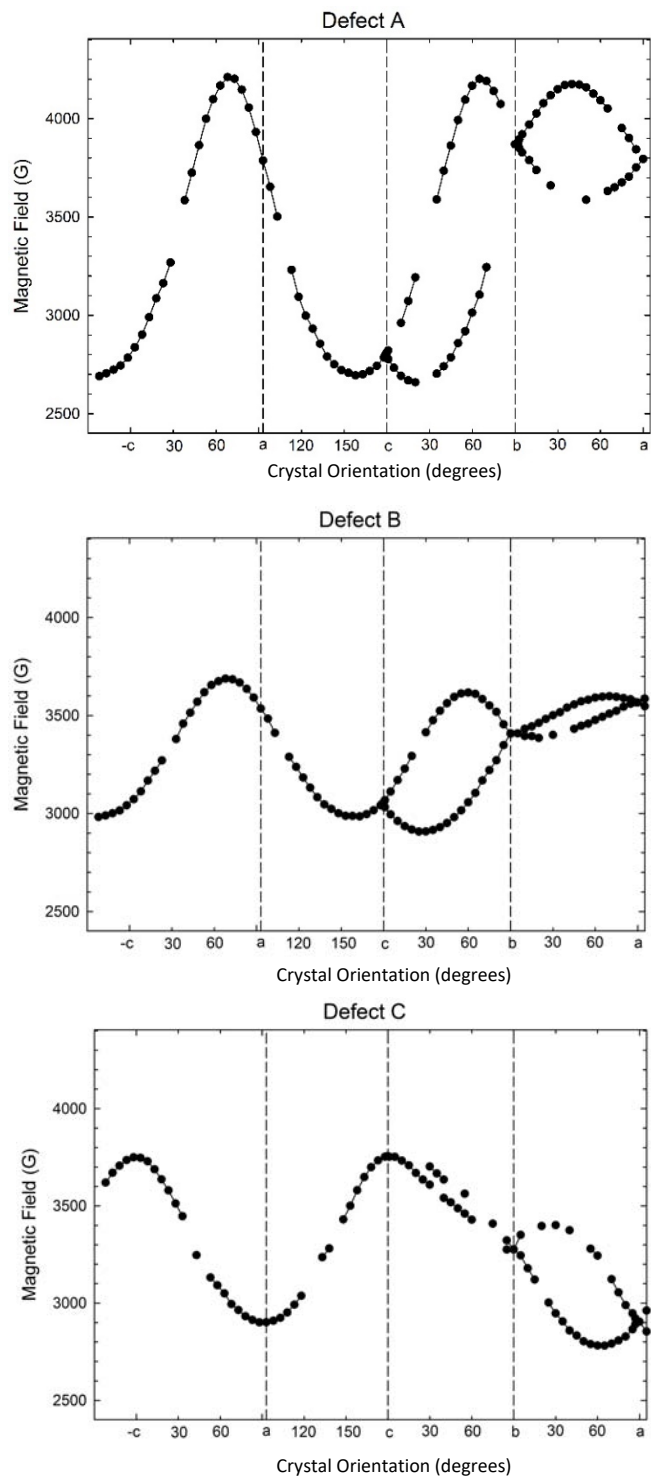


Figure 6.3. EPR angular dependence data for defects A, B, and C in Te-doped SPS. These data were taken at 20 K while the sample was illuminated with 633 nm HeNe laser light.

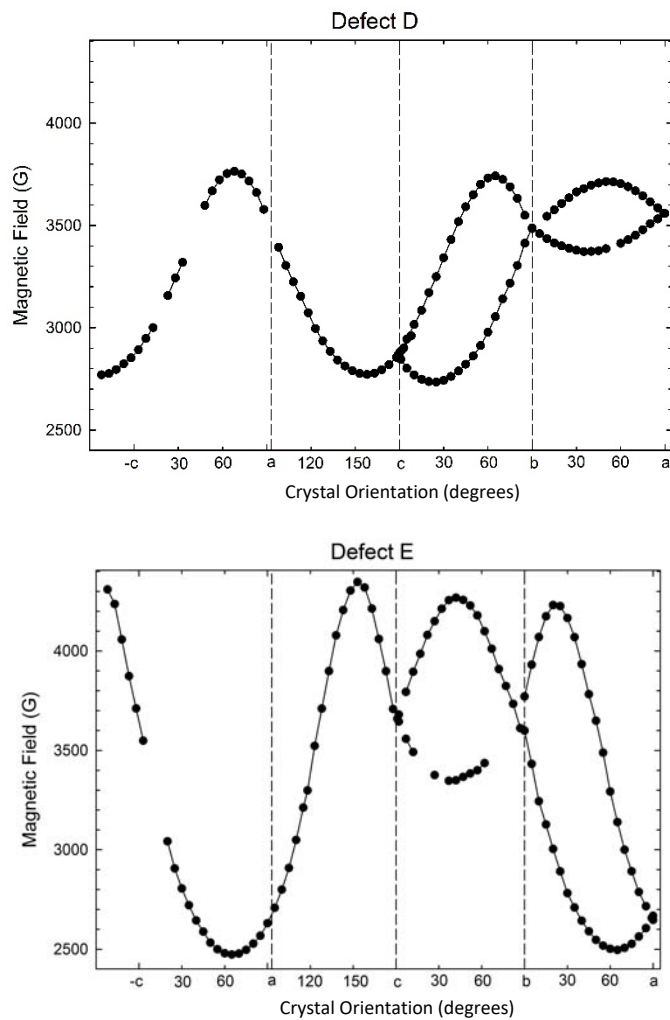


Figure 6.4. EPR angular dependence data for defects D and E in Te-doped SPS. The sample was illuminated with 633 nm laser light at 20 K, then briefly warmed to 110 K in the dark. The data were subsequently taken at 20 K without laser light.

The approximate thermal stabilities of the defects labeled A, B, C, D, and E, present in Figure 6.1, were determined. For this anneal experiment, the Te-doped crystal was initially aligned in the EPR cavity with the magnetic field along the c axis. Then at 20 K, the sample was exposed to 633 nm light. When the laser light was removed, the spectra did not decay. The intensities of the A, B, and C defects were recorded. Next, the sample was warmed to 60 K and held for two minutes, and then cooled back to 20 K. The intensities

of the three defects were again recorded. This procedure was repeated, with the higher anneal temperature increasing in steps of 20 K. Specifically, spectra were recorded at 20 K after holding for two min at 80, 100, 120, 140, and 160 K. The results of this experiment are shown in Figure 6.5.

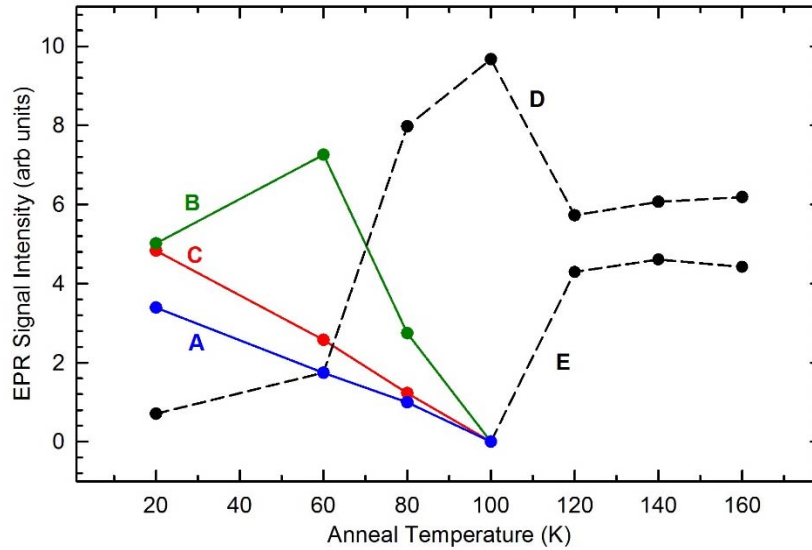


Figure 6.5. Pulsed anneal results from a 1% Te-doped SPS crystal showing the thermal decay of each center. EPR spectra were monitored at 20 K. The sample was held at each higher temperature for two minutes.

Another EPR signal, labeled defect F, is seen in Te-doped SPS crystals. This defect can be produced in two ways: (1) illuminate the sample at 20 K, warm to a temperature slightly above 100 K, then return to a monitoring temperature below 50 K, or (2) illuminate the sample at 100 K then cool the sample in the dark back to the monitoring temperature below 50 K. The spectrum of defect F is shown in Figure 6.6. Unlike defects A, B, C, D, and E, defect F does not exhibit large g-shifts as the crystal is rotated in the magnetic field. The angular dependence of defect F is shown in Figure 6.7. The other tellurium-related

defects have an angular dependence spanning 2000 G; in comparison, the angular dependence of defect F only extends over 150 G.

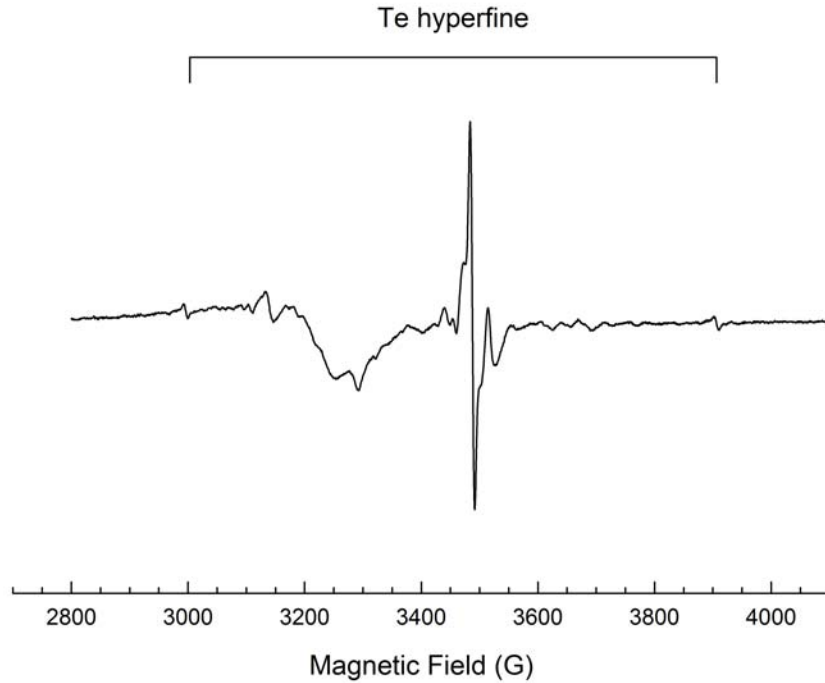


Figure 6.6. EPR spectrum of defect F in a Te-doped SPS crystal. Associated ^{125}Te hyperfine lines are identified.

The EPR spectrum from defect F shows a pair of hyperfine lines due to an interaction with a ^{125}Te nucleus. These lines are located near 3000 and 3900 G in Figure 6.6. It is interesting that the other tellurium-related defects (A through E) did not show tellurium hyperfine lines. The ^{125}Te isotope is 7.07% abundant and has an $I = 1/2$ nuclear spin. Thus, the two ^{125}Te lines in Figure 6.6 are a factor of 26 less intense than the center $I = 0$ line. Further discussion of the proposed model for defect F is presented in section 6.1.3.

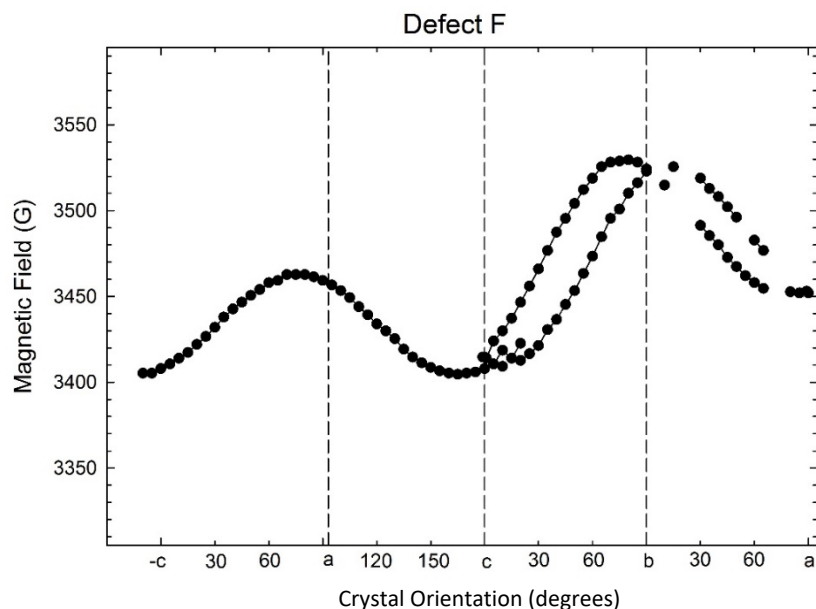


Figure 6.7. EPR angular-dependence for defect F in Te-doped SPS crystals.

6.1.2 Extracting Spin-Hamiltonian Matrix Parameters

Once the measured positions of the magnetic field lines were corrected, the angular-dependence data were analyzed using MatLab matrix programs. These programs were written expressly for fitting spin-Hamiltonian parameters to the angular data and predicting line positions once the parameters are known. In each case, the spin Hamiltonian is written in a matrix form, and then diagonalized to obtain the eigenvalues. For the defects in the Te-doped SPS crystals, the goal was to convert the angular dependence into a g matrix. There are six parameters, in general, for a g matrix. These six parameters include the three principal values and the three Euler angles that specify the orientation of the corresponding principal-axis directions relative to the crystal axes. The less intense Sn hyperfine lines are ignored at this point for the Te-related defects and only the electron Zeeman term in

the spin Hamiltonian is considered. In other words, only the intense $I = 0$ lines are used in the fitting. Equation 6.1 shows the spin Hamiltonian with only the electron Zeeman term.

$$H = \mu_B \mathbf{S} \cdot \mathbf{g} \cdot \mathbf{B} \quad (6.1)$$

To solve the spin Hamiltonian in general, there are multiple coordinate systems to consider. Three primary coordinate systems are used in this analysis: the magnetic field axes (x, y, z) where z is the direction of the static magnetic field, the crystal axes (x_c, y_c, z_c) , and the principal axes of the g matrix (x_g, y_g, z_g) . Ultimately, the spin Hamiltonian is written in the magnetic field coordinate system. This requires introducing 3×3 transformation matrices $[R]$ and $[G]$. In other words, the crystal axes (x_c, y_c, z_c) and g -matrix axes (x_g, y_g, z_g) are each written in terms of a rotation matrix multiplied by (x, y, z) in the magnetic field coordinate system. The rotation matrix $[R]$ transforms from the crystal axes (x_c, y_c, z_c) to the magnetic field axes (x, y, z) . Mathematically, this equates to $(x_c, y_c, z_c) = R(x, y, z)$. Similarly, the rotation matrix $[G]$ transforms the g matrix axes to the crystal axes, or $(x_g, y_g, z_g) = G(x_c, y_c, z_c)$. The product of the two rotation matrices $[GR] = [G][R]$ transforms the g matrix axes to the magnetic field axes, or equivalently $(x_g, y_g, z_g) = G(x_c, y_c, z_c) = GR(x, y, z)$. Equation 6.1 is first written in terms of the g matrix coordinate system, as in Equation 6.2.

$$H = \mu_B (S_{x_g} g_x B_{x_g} + S_{y_g} g_y B_{y_g} + S_{z_g} g_z B_{z_g}) \quad (6.2)$$

The operators S_{x_g} , S_{y_g} , and S_{z_g} are then written in the magnetic field coordinate system using the combined rotation matrix $[GR]$. For example, S_{x_g} becomes $S_{x_g} = GR(1,1)S_x + GR(1,2)S_y + GR(1,3)S_z$. A similar process is followed for S_{y_g} and

S_{zg} . Note that when the static magnetic field components B_{xg} , B_{yg} , and B_{zg} in the g matrix coordinate system are expressed in the magnetic field coordinate system, only B_z is nonzero because the direction of the magnetic field is chosen to be the z axis. Therefore, $B_{xg} = GR(1,3)B_z$, $B_{yg} = GR(2,3)B_z$, and $B_{zg} = GR(3,3)B_z$. Equation 6.2 is now rewritten in the following form.

$$H = \mu_B B_z \left(g_x GR(1,3) (GR(1,1)S_x + GR(1,2)S_y + GR(1,3)S_z) \right. \\ \left. + g_y GR(2,3) (GR(2,1)S_x + GR(2,2)S_y + GR(2,3)S_z) \right. \\ \left. + g_z GR(3,3) (GR(3,1)S_x + GR(3,2)S_y + GR(3,3)S_z) \right) \quad (6.3)$$

By separately combining terms with S_x , S_y , and S_z , Equation 6.3 can be written in the form $H = W_1 S_x + W_2 S_y + W_3 S_z$. The spin operators are then rewritten in terms of the raising and lowering operators: $S_x = \frac{1}{2}(S_+ + S_-)$ and $S_y = \frac{1}{2i}(S_+ - S_-)$. This converts the spin Hamiltonian to the form shown in Equation 6.4.

$$H = \frac{1}{2}(W_1 - iW_2)S_+ + \frac{1}{2}(W_1 + iW_2)S_- + W_3 S_z \quad (6.4)$$

Finally, the spin Hamiltonian is expressed as a matrix. The Te-related defects described in this chapter have $S = 1/2$. Thus, the two basis states are $MS = | + 1/2 \rangle$ and $MS = | - 1/2 \rangle$. The result is a 2×2 Hamiltonian matrix with four elements.

$$H = \frac{1}{2} \begin{bmatrix} W_3 & (W_1 - iW_2) \\ (W_1 + iW_2) & W_3 \end{bmatrix} \quad (6.5)$$

Eigenvalues obtained by diagonalizing the matrix in Equation 6.5 are used in a least-squares fitting routine (located in Appendix B) to determine the six parameters

describing the g matrix for each tellurium defect in SPS. Data used in this fitting process is also included in Appendix B. Table 6.1 contains the final best-fit values for these g matrix parameters. The Euler angles presented in Table 6.1 are defined using the ZXZ convention, where the first rotation ϕ is about the z -axis, followed by a rotation of θ about the new x -axis, and then finally a rotation ψ about the subsequent Z axis again.

Table 6.1: Spin Hamiltonian parameters for Te-related defects

Defect	Principal g values			Euler Angles in degrees		
				ϕ	θ	ψ
A	2.610	1.605	1.580	60.64	45.25	87.75
B	2.307	1.919	1.795	60.55	70.57	72.25
C	2.400	1.945	1.786	-9.61	83.46	124.54
D	2.490	1.986	1.613	64.12	46.30	85.17
E	2.853	1.541	1.594	59.10	9.27	27.40
F	1.898	1.941	1.971	-24.00	69.00	38.00

6.1.3 Models for Te-Related Defects

As shown in Figure 6.1, the Te-related defects labeled A, B, and C have less intense lines in the low and high field regions; these are due to interactions with ^{117}Sn and ^{119}Sn nuclei. The ^{117}Sn and ^{119}Sn isotopes both have $I = 1/2$, are 7.68% and 8.59% abundant, respectively. Observation of these Sn hyperfine lines is a key result that allows model assignments to be made for the Te-related defects. Similar Sn hyperfine lines were seen in the EPR spectrum of the Sn vacancy in SPS crystals [22]. The unpaired spin in the Sn-vacancy study was primarily localized on the adjacent $(\text{P}_2\text{S}_6)^{4-}$ anionic unit. Thus, by analogy, a model is proposed for defects A, B, and C where a Te^{2-} ion replaces a S^{2-} ion and a hole is trapped on the resulting $(\text{P}_2\text{TeS}_5)^{4-}$ anionic unit, thus converting it to a $(\text{P}_2\text{TeS}_5)^{3-}$ unit. The three defects would correspond to three different locations of the Te

ion in the anionic unit. Although the Sn hyperfine lines in Figure 6.1 are separated by thousands of gauss, the portion of the unpaired spin actually located on the adjacent Sn ion is only a few percent. The results of the angular studies in Figures 6.2 and 6.3 and the thermal decay of the EPR signals in Figure 6.5 also support the assignment of defects A, B, and C to holes trapped on Te-containing anionic units.

An EPR signal from an electron trap was not observed at the same time that the holelike defects A, B, and C were observed. This suggests that the compensating electron trap is in a nonparamagnetic state. Therefore, the electron trap is not seen after illumination with the 633 nm light. This suggests the electron trap during and after illumination is trapping two electrons. As considered earlier, a defect showing this behavior would be the Te^{4+} ion on a Sn^{2+} site. Upon trapping two electrons, a Te^{4+} ion becomes a Te^{2+} ion.

The defect labeled D also represents a hole trapped at a Te ion replacing a S ion, and exhibits characteristics similar to defects A, B and C such as the presence of Sn hyperfine and large g shifts. The thermal anneal results in Figure 6.5 show that when the holes associated with defects A, B, and C become thermally unstable, they move to $(\text{P}_2\text{TeS}_5)^{4-}$ units that have the Te ion in the proper position to form the $(\text{P}_2\text{TeS}_5)^{3-}$ unit labeled defect D. Then as defect D becomes thermally unstable between 100 K and 120 K, the EPR signal from defect E appears. Figure 6.5 shows that the decrease in the concentration of defect D is comparable to the increase in the concentration of defect E. This supports the idea that the hole moved from an anionic unit with the Te ion on one S site (defect D) to a nearby anionic unit with the Te ion on a different S site (defect E). Defect E has an angular dependence that strongly resembles that of defects A, B, C, and

D, with principal g values well above and below $g=2.0$. Therefore defect E is also likely a hole trap. Despite the absence of Sn hyperfine, the model for defect E must be similar to the Te-replacing-S models for the other trapped hole defects. It is not presently understood why defect E does not have an observable hyperfine interaction with an adjacent Sn ion. A generic model for defects A, B, C, D, and E is shown in the left side of Figure 6.8. The possible presence of the Sn^{2+} vacancy may help to stabilize the hole at the anionic units with a Te ion.

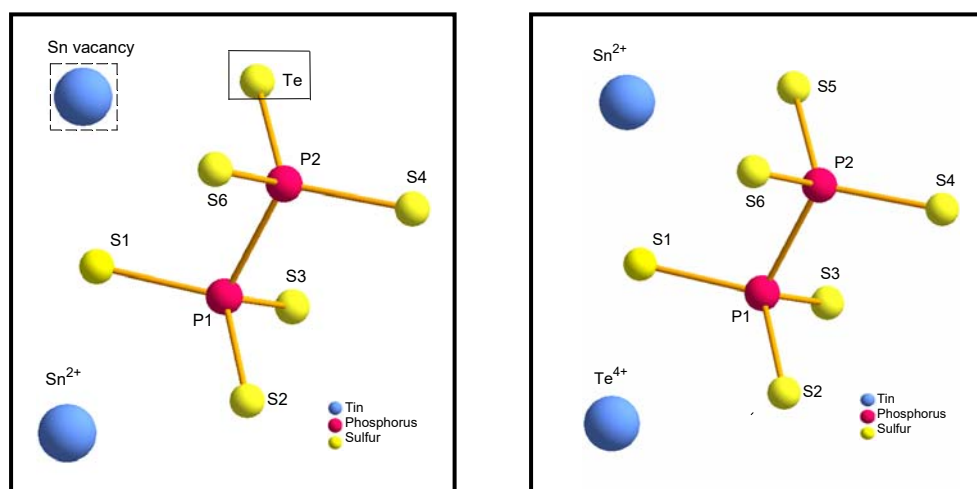


Figure 6.8. (Left) Models for defects A, B, C, D, and E involving Te ions on a S site. There may be a Sn vacancy next to the defect. (Right) Model for defect F involving a Te ion on a Sn site.

Defect F, on the other hand, is distinct from defects A, B, C, D, and E. The EPR spectrum from defect F has hyperfine lines from one tellurium nucleus and also has a significantly different angular dependence. Its principal g values, from Table 6.1, are all less than $g = 2.00$. Together, these provide strong evidence that defect F is an electron trap.

The presence of tellurium hyperfine would suggest that defect F corresponds to a tellurium ion on a tin site. A possible model could be a tellurium ion on a tin site which is next to another tin vacancy. A more reasonable model is a tellurium on a tin site that trapped two electrons upon illumination; then as the crystal is warmed, one of the electrons is released. Once that first electron is released, the defect becomes paramagnetic. Defect F is seen at the same time as defect D and E, but as the crystal continues to warm, all three defect signals decrease. Defect D and E are inversely correlated when the EPR signal for defect F is absent (i.e., when defect D decreases, defect E increases), but both signals decrease when the EPR line for defect F is present. This strongly supports the model that defect F is a Te^{3+} ion (with $S = 1/2$) on a Sn site.

6.2 Iodine-Related EPR Spectrum

Iodine was unexpectedly discovered to be present in tellurium- and silver-doped SPS crystals. In all of these samples, the crystal was grown using the chemical-vapor-transport method, with iodine (SnI_4) being used as the transfer agent during the crystal growth process. There is no previously published research showing that isolated iodine ions are incorporated as an inadvertent impurity in SPS crystals, but there are instances of other single crystals that were deliberately doped with iodine [52-56]. In all the SPS samples where iodine is seen, the EPR spectrum is photoinduced with 633 nm light from a HeNe laser. To produce the iodine spectrum, the sample was first illuminated with laser light at 20 K. Then the light was removed, and the sample was briefly warmed to a temperature above 50 K (for Ag-doped) or above 100 K (for Te-doped). Although the EPR signal for iodine is easily produced at temperatures above 100 K for Te-doped SPS, the

signal decays slowly over several minutes when the temperature of the sample is then held constant at approximately 50 K. In these cases, the sample was quickly cooled back to 20 K to prevent loss of signal.

Figure 6.9 shows the new EPR spectra due to iodine in a Te-doped SPS crystal. These two spectra were taken with the magnetic field along the *b* and *c* axes. For both the *b* and *c* directions of magnetic field, there are two sets of 6 lines as illustrated by the stick diagrams above the spectra. This suggests that the responsible defect consists of an unpaired spin ($S = 1/2$) interacting with two nuclear spins, one with $I = 5/2$ and one with $I = 1/2$. The obvious choice for these nuclei are ^{127}I and the ^{31}P . Both the $I = 5/2$ isotope and $I = 1/2$ isotope are 100% abundant because there are no $I = 0$ lines in the spectra. Phosphorus is a constituent element in SPS, thus it is reasonable to assign the $I = 1/2$ lines to ^{31}P . Possible assignments for the $I = 5/2$ nuclei include ^{27}Al , ^{55}Mn , ^{127}I , and ^{141}Pr , as these are the only nuclei that have $I = 5/2$ and 100% abundance. Of these nuclei, only iodine is a realistic candidate since aluminum and praseodymium are not expected to be present in SPS crystals. Furthermore, if manganese were present in SPS, it would be Mn^{2+} on a Sn^{2+} site. In this charge state, manganese has a quite different EPR spectrum because of its 5 d-shell electrons ($S = 5/2$ spin), and therefore the observed spectrum is not due to Mn^{2+} ions. For these reasons, the $I = 5/2$ hyperfine in Figure 6.9 is assigned to ^{127}I nuclei. Numerous less intense lines are present in the spectra in Figure 6.9, in addition to the two more intense sets of 6 lines. These less intense lines are most likely due to partially allowed lines arising from a nuclear electric quadrupole interaction for the ^{127}I nuclei. The strength of this quadrupole interaction depends on the product of the magnitude of the electric

quadrupole moment of the ^{127}I nucleus and the magnitude of the electric field gradient at the nucleus. The quadrupole moment of ^{127}I is large and the electric field gradients in monoclinic SPS crystals are also large, thus nuclear electric quadrupole effects should be expected in the iodine spectra.

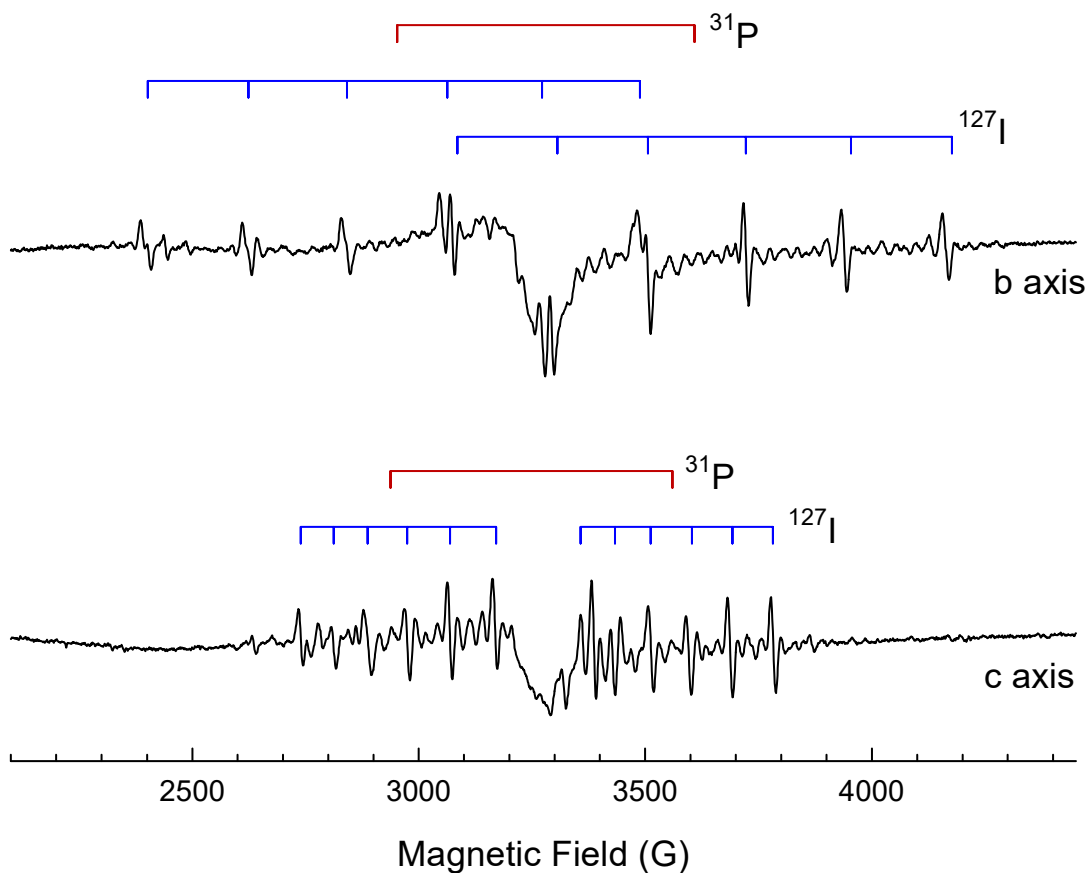


Figure 6.9. Iodine-related EPR spectra taken at 20 K from a Te-doped SPS crystal after exposure to 633 nm laser light.

6.2.1 Extracting Spin-Hamiltonian Matrix Parameters

The spin Hamiltonian representing iodine in SPS crystals is significantly more complex than the Hamiltonian for the tellurium-related defects. This is because the EPR spectrum shows hyperfine interactions with two nuclear spins. Thus, the spin Hamiltonian must contain hyperfine terms for both nuclei. Specifically, the EPR spectrum describes a single unpaired electron spin ($S=1/2$) interacting with 100% $I = 1/2$ and $I=5/2$ nuclear spins. Thus, the number of terms in the spin Hamiltonian (and the number of subsequent matrix elements) increases. Rewriting Equation 3.1 for the two nuclei I_1 and I_2 gives Equation 6.6.

$$H = \mu_B \mu_B \mathbf{S} \cdot \mathbf{g} \cdot \mathbf{B} + \mathbf{I}_1 \cdot \mathbf{A}_1 \cdot \mathbf{S} + \mathbf{I}_2 \cdot \mathbf{A}_2 \cdot \mathbf{S} - g_{n_1} \mu_N \mathbf{I}_1 \cdot \mathbf{B} - g_{n_2} \mu_N \mathbf{I}_2 \cdot \mathbf{B} \quad (6.6)$$

For this particular case, let $I_1 = 1/2$ and $I_2 = 5/2$. Several sets of axes must be defined and rewritten in a common set of axes. That common set is (x, y, z) which corresponds to the magnetic field coordinate system, where the magnetic field \mathbf{B} is parallel to z . Additional coordinate systems are the principal axes of the g -matrix (x_g, y_g, z_g) , the principal axes of the A_1 matrix (x_1, y_1, z_1) , the principal axes of the A_2 matrix (x_2, y_2, z_2) , and the crystal axes (x_c, y_c, z_c) .

Now it is necessary to establish rotation matrices such that each set of axes can be written in terms of the chosen axes (x, y, z) . First, let $(x_c, y_c, z_c) = \mathbf{R}(x, y, z)$ where \mathbf{R} is a 3 x 3 rotation matrix. Next, let $(x_g, y_g, z_g) = [\mathbf{G}](x_c, y_c, z_c) = [\mathbf{G}][\mathbf{R}](x, y, z) = [\mathbf{TR}](x, y, z)$, where $[\mathbf{G}]$ and $[\mathbf{TR}]$ are also 3 x 3 matrices. Using analogous expressions, the principal axes of the A_1 and A_2 matrices can be written in terms of yet additional rotation matrices \mathbf{H}_1 and \mathbf{H}_2 , or equivalently $(x_1, y_1, z_1) = [\mathbf{H}_1](x_c, y_c, z_c) = [\mathbf{H}_1][\mathbf{R}](x, y, z) = [\mathbf{TH}_1](x, y, z)$. The spin

operators in Equation 6.6 can now be rewritten in terms of the same axes (x, y z), as shown in Equation 6.7 (note that B is assumed to be B_z).

$$\begin{aligned}
S_{x_g} &= TG(1,1)S_x + TG(1,2)S_y + TG(1,3)S_z \\
S_{y_g} &= TG(2,1)S_x + TG(2,2)S_y + TG(2,3)S_z \\
S_{z_g} &= TG(3,1)S_x + TG(3,2)S_y + TG(3,3)S_z \\
\\
I_{x_1}^1 &= TH_1(1,1)I_x^1 + TH_1(1,2)I_y^1 + TH_1(1,3)I_z^1 \\
I_{y_1}^1 &= TH_1(2,1)I_x^1 + TH_1(2,2)I_y^1 + TH_1(2,3)I_z^1 \\
I_{z_1}^1 &= TH_1(3,1)I_x^1 + TH_1(3,2)I_y^1 + TH_1(3,3)I_z^1 \\
\\
S_{x_1} &= TH_1(1,1)S_x + TH_1(1,2)S_y + TH_1(1,3)S_z \\
S_{y_1} &= TH_1(2,1)S_x + TH_1(2,2)S_y + TH_1(2,3)S_z \\
S_{z_1} &= TH_1(3,1)S_x + TH_1(3,2)S_y + TH_1(3,3)S_z \\
\\
I_{x_2}^2 &= TH_2(1,1)I_x^2 + TH_2(1,2)I_y^2 + TH_2(1,3)I_z^2 \\
I_{y_2}^2 &= TH_2(2,1)I_x^2 + TH_2(2,2)I_y^2 + TH_2(2,3)I_z^2 \\
I_{z_2}^2 &= TH_2(3,1)I_x^2 + TH_2(3,2)I_y^2 + TH_2(3,3)I_z^2 \\
\\
S_{x_2} &= TH_2(1,1)S_x + TH_2(1,2)S_y + TH_2(1,3)S_z \\
S_{y_2} &= TH_2(2,1)S_x + TH_2(2,2)S_y + TH_2(2,3)S_z \\
S_{z_2} &= TH_2(3,1)S_x + TH_2(3,2)S_y + TH_2(3,3)S_z \\
\\
B_{x_g} &= TG(1,3)B \\
B_{y_g} &= TG(2,3)B \\
B_{z_g} &= TG(3,3)B
\end{aligned} \tag{6.7}$$

Making the substitutions of terms in Equation 6.7 into Equation 6.6, the spin Hamiltonian with all terms now becomes:

$$\begin{aligned}
H = \mu_B B_z \{ & g_x GR(1,3) [GR(1,1)S_x + GR(1,2)S_y + GR(1,3)S_z] \\
& + g_y GR(2,3) [GR(2,1)S_x + GR(2,2)S_y + GR(2,3)S_z] \\
& + g_z GR(3,3) [GR(3,1)S_x + GR(3,2)S_y + GR(3,3)S_z] \} \\
+ A_x^1 [& TH_1(1,1)TH_1(1,1)I_x^1 S_x + TH_1(1,2)TH_1(1,1)I_y^1 S_x \\
& + TH_1(1,3)TH_1(1,1)I_z^1 S_x + TH_1(1,1)TH_1(1,2)I_x^1 S_y \\
& + TH_1(1,2)TH_1(1,2)I_y^1 S_y + TH_1(1,3)TH_1(1,2)I_z^1 S_y \\
& + TH_1(1,1)TH_1(1,3)I_x^1 S_z + TH_1(1,2)TH_1(1,3)I_y^1 S_z \\
& + TH_1(1,3)TH_1(1,3)I_z^1 S_z] \\
+ A_y^1 [& TH_1(2,1)TH_1(2,1)I_x^1 S_x + TH_1(2,2)TH_1(2,1)I_y^1 S_x \\
& + TH_1(2,3)TH_1(2,1)I_z^1 S_x + TH_1(2,1)TH_1(2,2)I_x^1 S_y \\
& + TH_1(2,2)TH_1(2,2)I_y^1 S_y + TH_1(2,3)TH_1(2,2)I_z^1 S_y \\
& + TH_1(2,1)TH_1(2,3)I_x^1 S_z + TH_1(2,2)TH_1(2,3)I_y^1 S_z \\
& + TH_1(2,3)TH_1(2,3)I_z^1 S_z] \\
+ A_z^1 [& TH_1(3,1)TH_1(3,1)I_x^1 S_x + TH_1(3,2)TH_1(3,1)I_y^1 S_x \\
& + TH_1(3,3)TH_1(3,1)I_z^1 S_x + TH_1(3,1)TH_1(3,2)I_x^1 S_y \\
& + TH_1(3,2)TH_1(3,2)I_y^1 S_y + TH_1(3,3)TH_1(3,2)I_z^1 S_y \\
& + TH_1(3,1)TH_1(3,3)I_x^1 S_z + TH_1(3,2)TH_1(3,3)I_y^1 S_z \\
& + TH_1(3,3)TH_1(3,3)I_z^1 S_z] \\
+ A_x^2 [& TH_2(1,1)TH_2(1,1)I_x^2 S_x + TH_2(1,2)TH_2(1,1)I_y^2 S_x \\
& + TH_2(1,3)TH_2(1,1)I_z^2 S_x + TH_2(1,1)TH_2(1,2)I_x^2 S_y \\
& + TH_2(1,2)TH_2(1,2)I_y^2 S_y + TH_2(1,3)TH_2(1,2)I_z^2 S_y \\
& + TH_2(1,1)TH_2(1,3)I_x^2 S_z + TH_2(1,2)TH_2(1,3)I_y^2 S_z \\
& + TH_2(1,3)TH_2(1,3)I_z^2 S_z] \\
+ A_y^2 [& TH_2(2,1)TH_2(2,1)I_x^2 S_x + TH_2(2,2)TH_2(2,1)I_y^2 S_x \\
& + TH_2(2,3)TH_2(2,1)I_z^2 S_x + TH_2(2,1)TH_2(2,2)I_x^2 S_y \\
& + TH_2(2,2)TH_2(2,2)I_y^2 S_y + TH_2(2,3)TH_2(2,2)I_z^2 S_y \\
& + TH_2(2,1)TH_2(2,3)I_x^2 S_z + TH_2(2,2)TH_2(2,3)I_y^2 S_z \\
& + TH_2(2,3)TH_2(2,3)I_z^2 S_z] \\
+ A_z^2 [& TH_2(3,1)TH_2(3,1)I_x^2 S_x + TH_2(3,2)TH_2(3,1)I_y^2 S_x \\
& + TH_2(3,3)TH_2(3,1)I_z^2 S_x + TH_2(3,1)TH_2(3,2)I_x^2 S_y \\
& + TH_2(3,2)TH_2(3,2)I_y^2 S_y + TH_2(3,3)TH_2(3,2)I_z^2 S_y \\
& + TH_2(3,1)TH_2(3,3)I_x^2 S_z + TH_2(3,2)TH_2(3,3)I_y^2 S_z \\
& + TH_2(3,3)TH_2(3,3)I_z^2 S_z] \\
- g_{n_1} \mu_N I_z^1 B - g_{n_2} \mu_N I_z^2 B
\end{aligned} \tag{6.8}$$

As was previously done for the tellurium-related defects, the spin operators are rewritten in terms of raising and lowering operators, as shown in Equation 6.9.

$$\begin{aligned}
 S_x &= \frac{1}{2}(S_+ + S_-) \\
 S_y &= \frac{1}{2i}(S_+ - S_-) \\
 I_x &= \frac{1}{2}(I_+ + I_-) \\
 I_y &= \frac{1}{2i}(I_+ - I_-)
 \end{aligned}
 \tag{6.9}$$

Finally, choose the 24 basis-set states $|m_s, m_{I_1}, m_{I_2}\rangle$. These are combinations of $m_s = \{+\frac{1}{2}, -\frac{1}{2}\}$, $m_{I_1} = \{+\frac{1}{2}, -\frac{1}{2}\}$, and $m_{I_2} = \{+\frac{5}{2}, +\frac{3}{2}, +\frac{1}{2}, -\frac{1}{2}, -\frac{3}{2}, -\frac{5}{2}\}$. Using these basis states, the spin Hamiltonian is written as a 24 x 24 Hermitian matrix. Many of the elements are zero. Diagonalizing the 24 x 24 matrix produces the eigenvalues that are used to determine the best set of spin-Hamiltonian parameters for the iodine spectrum. There are 18 parameters that must be determined, six for the g matrix and six each for the phosphorus and iodine hyperfine matrices. A Matlab least-squares fitting routine, similar to the one in Appendix B, was written to extract these parameters from the experimental angular-dependence data. The final set of parameters for the iodine spectrum are presented in Table 6.2.

6.2.2 Model for Iodine in $\text{Sn}_2\text{P}_2\text{S}_6$

When the iodine impurity was first discovered in this material, the expectation was that it would be located on a sulfur site because of the similar electronic structures. In SPS, S^{2-} ions would have valence electrons in the $3p^6$ orbitals and I^- on a S^{2-} site would have

similar $5p^6$ valence electrons. However, the EPR data suggest that the unpaired electron interacts with an iodine and a single phosphorus atom.

Table 6.2: Spin-Hamiltonian parameters describing iodine EPR spectrum in SPS crystals

g-value	^{31}P hyperfine (MHz)	^{127}I hyperfine (MHz)
1.9787	2029.0	268.4
2.0592	1464.6	658.3
2.0113	1802.3	235.3

Euler Angles	g-matrix	A matrix for ^{31}P	A matrix for ^{127}I
ϕ	-26.75°	146.05°	2.95°
θ	24.10°	-37.50°	8.40°
ψ	94.20°	10.80°	12.40°

It is this phosphorous interaction that provides the critical information to determine the model for the iodine-related defect. Other defects studied in SPS crystals [14, 22, 27], where the unpaired spin is shared with phosphorus, shows *two* phosphorus ions are involved, not just one. These are the spectra for the Sn vacancy, the S vacancy, and a Sb^{2+} ion next to a Sn vacancy. However, in the present case where the unpaired spin interacts with only one phosphorous nucleus and another $I = 5/2$ nucleus, the data strongly suggest that the iodine ion is replacing a phosphorous ion in the SPS crystal. The phosphorous ions are normally present as pairs, adjacent to each other, in the $(\text{P}_2\text{S}_6)^{4-}$ anionic units in the regular lattice. The suggested model replaces one component of the phosphorous pair with an iodine, thus forming a $(\text{PIS}_6)^{4-}$ unit that converts to a $(\text{PIS}_6)^{5-}$ unit when an electron is trapped during illumination at low temperature. As demonstrated in the EPR spectra, this model has the unpaired spin interacting with one phosphorous nucleus and one iodine

nucleus. An example in the literature of iodine being present as I^{5+} ions is $LiIO_3$ crystals, a nonlinear optical material [56].

The production of the iodine EPR spectrum is different in the tellurium- and silver-doped crystals, which suggests the production mechanism for the iodine signal depends on other defects that are present in the material. For the tellurium-doped SPS samples, the hypothesized tellurium-related electron trap is trapping two electrons when the sample is illuminated with 633 nm HeNe laser light at 20 K. Then, when the sample is briefly warmed to temperatures above 100 K after removing the laser light, the Te electron trap releases one of the electrons, forming the tellurium-related defect F previously discussed in Section 6.2.1. The released electron could either annihilate a trapped hole (e.g., a hole that was trapped as defects D or E), or it could become trapped at iodine replacing the phosphorus ion in the $(PIS_6)^{4-}$ unit. In support of this model, the iodine EPR spectrum is seen at the same time as defects D, E, and F. The relative intensities of these EPR spectra, however, depends on the specific temperature that the sample is warmed to.

6.3 Copper Impurity in $Sn_2P_2S_6$ Crystals

An SPS sample doped with 1% copper was also studied using EPR. This defect was initially investigated by Dr. Eric Golden. When the sample is illuminated with 633 nm HeNe laser light at 38 K, an EPR signal associated with copper is easily seen, as shown in Figure 6.10. This spectrum has hyperfine structure due to ^{63}Cu and ^{65}Cu nuclei. These isotopes have $I = 3/2$ with abundances of 69.15% and 30.85%, respectively. Thus, four EPR lines are expected per nuclei. In this case, the lines due to each copper isotope are overlapping and the two isotopes are not resolved. There are also hyperfine lines present

in the spectrum from ^{117}Sn and ^{119}Sn nuclei at one neighboring Sn site. As the sample is rotated in the a-c plane, all four copper lines collapse into a single line. This is similar to the behavior observed for Cu in CSP.

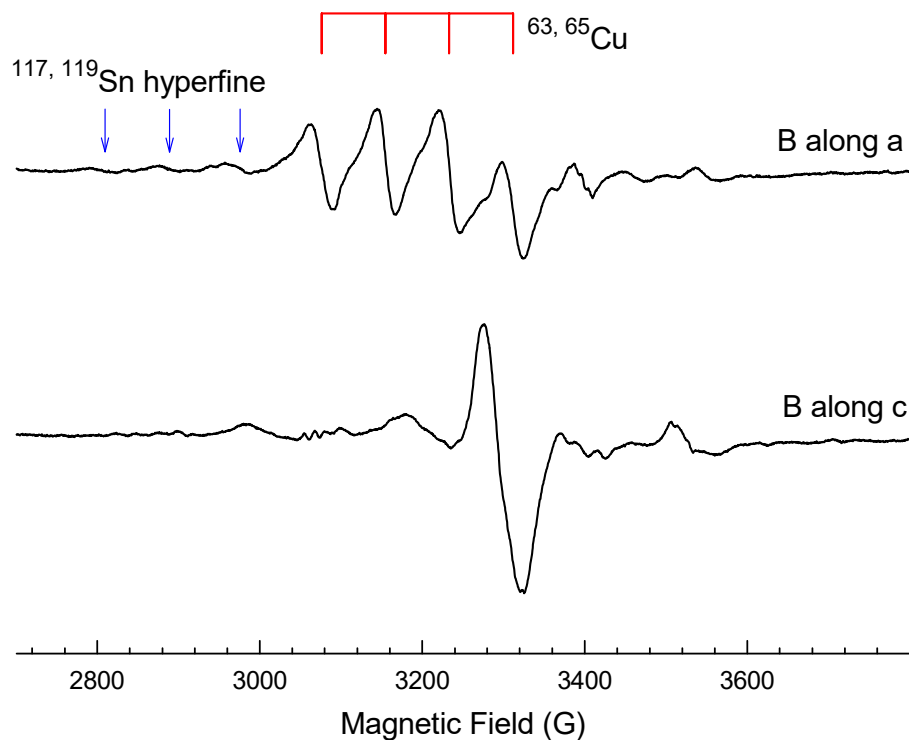


Figure 6.10. EPR spectra from Cu impurities in SPS crystals.

The thermal stability of the photoinduced copper EPR signal in SPS was determined. Initially, 633 nm HeNe laser light was placed on the sample at 40 K, then the laser light was removed and the intensity of the copper signal was measured. The sample was warmed briefly to 60 K, then cooled back to 40 K. The intensity of the copper signal was again measured. The sample was then warmed briefly again to 80 K and cooled back to 40 K again. After measuring the resulting EPR intensity, the sample was warmed to an

even higher temperature. The results of this thermal anneal study are shown in Figure 6.11.

These data suggests that the activation energy for the copper defect is roughly 140 meV.

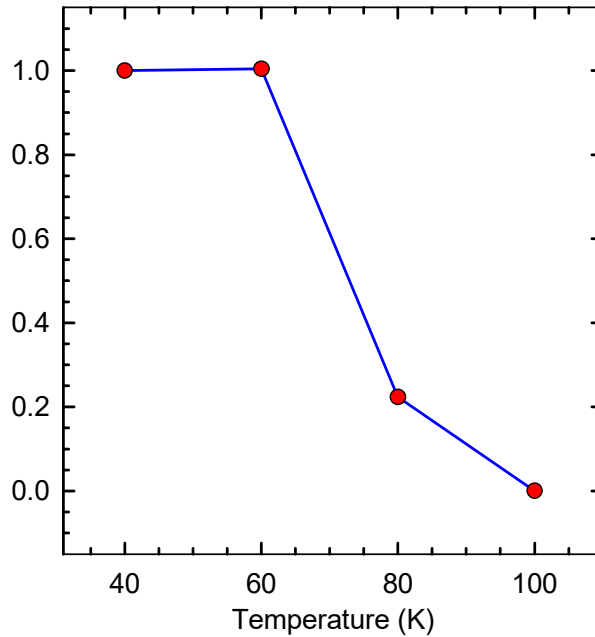


Figure 6.11. Thermal stability of the photoinduced Cu EPR signal in SPS.

6.3.1 Model for the Copper Impurity

The EPR spectrum of copper suggests that the copper ion is on a Sn site in the SPS crystal. In SPS, copper would expected to be in the $\text{Cu}^{2+} (3d^9)$ ground state when on a Sn^{2+} site. However, this does not appear to be the case. Copper instead exhibits characteristics of a shallow, more hydrogenic-like, acceptor in SPS. Furthermore, the angular dependence of the EPR signal for copper indicates the unpaired spin is not in the d shell. The g-values for copper were determined (shown in Table 6.3). This defect has small g shifts from $g = 2.0$ which suggests that the unpaired spin is in a delocalized outer orbital.

Table 6.3: Spin-Hamiltonian parameters for copper in a 1% Cu-doped SPS crystal.

Direction	g-value	Cu hyperfine
a	2.0949	78.7 G
b	2.0505	49.7 G
c	2.0292	< 10 G

One possible explanation that is consistent with the delocalized unpaired spin is that copper has accepted an extra electron (due to the material being compensated) and is therefore a singly ionized A^- acceptor with $S = 0$ before illumination. In this state, the copper would be Cu_{Sn}^- with electron configuration $3d^{10} + 2e^-$. During illumination, the copper loses this extra electron and becomes a neutral A^0 acceptor with $S = 1/2$. In other words, it becomes Cu_{Sn}^0 with electron configuration $3d^{10} + 1e^-$. The A^0 and A^- acceptors both have a filled $3d^{10}$ shell and therefore there is no unpaired spin in the d-shell. They have one or two outer electrons, respectively, that are partially delocalized onto neighboring anions and cations.

6.4 Silver-Related Defect in $Sn_2P_2S_6$ Crystals

Silver-doped SPS is expected to behave similarly to Cu-doped SPS. This, however, is not the case for a 1% Ag-doped SPS crystal. A hole trapped at a Ag-on-Sn site, which would be analogous to the Cu-on-Sn site previously discussed, is not seen. The expected EPR signal for this hole trap would exhibit a positive g shift and a relatively small Ag hyperfine splitting. Instead, a quite different Ag-related EPR spectrum is observed. As seen in Figure 6.12, it consists of a pair of lines with an electronlike negative g shift and a large hyperfine splitting (934 G) due to ^{107}Ag and ^{109}Ag nuclei (both with $I = 1/2$). The

separation and positions of the two lines change significantly as the temperature goes from 20 to 50 K. This suggests that the Ag ion may be rapidly moving between equivalent positions. This spectrum is assigned to a Ag ion (at either an interstitial or a Sn site) that has trapped an electron and is best described as a Ag^0 atom ($4d^{10}5s^1$).

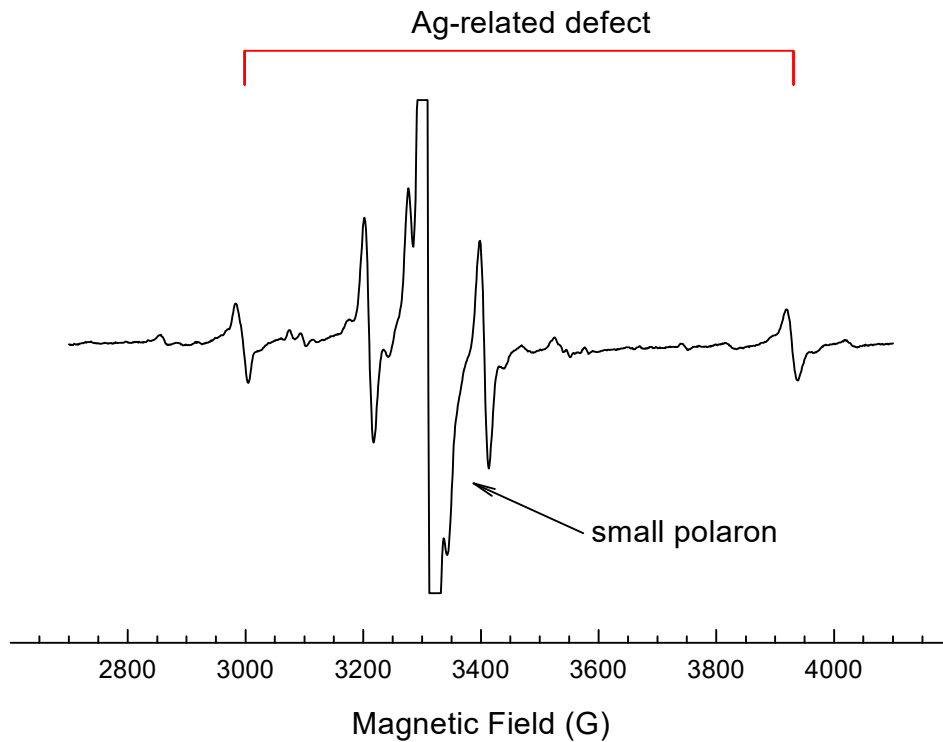


Figure 6.12. EPR spectrum obtained from a 1% Ag-doped SPS crystal. The spectrum was taken at 30 K with the magnetic field along the b axis while illuminated with 633 nm laser light during measurement.

Chapter 7. Conclusions

Point defects in two semiconductor materials, CdSiP₂ and Sn₂P₂S₆, have been investigated and characterized. Electron paramagnetic resonance (EPR) spectroscopy is used to identify the electronic structure of defects and their charge states. EPR spectra and optical absorption bands were correlated, and thus specific defect assignments were made for the primary absorption bands in CdSiP₂. My research established that singly ionized silicon vacancies in CdSiP₂ (V_{Si}^-) are responsible for three unwanted absorption bands at 800 nm, 1.0 μm , and 1.9 μm , which are easily seen at room temperature. Two new acceptor defects were identified in CdSiP₂: the neutral silicon-on-phosphorus antisite (Si_P^0) and the neutral copper-on-cadmium (Cu_{Cd}^0). These defects are easily seen at 77 K and are associated with two additional broad photoinduced optical absorption bands at 0.8 μm and 1.4 μm . For all three acceptors that were studied (V_{Si}^- , Si_P^0 , and Cu_{Cd}^0), the associated donor is Si_{Cd}^+ . This research has also established that illuminating a CdSiP₂ crystal with 1064 nm light may reduce the unwanted absorption, and therefore pumping a CdSiP₂-based optical parametric oscillator with 1064 nm light may improve device performance.

Seven point defects that have not previously been reported have been identified in tellurium-doped Sn₂P₂S₆ crystals using EPR. Two of these point defects are trapped-electron centers: an iodine ion on a phosphorous site and a tellurium ion on a Sn site. Five point defects are trapped-hole centers that are attributed to Te ions replacing sulfur ions. The g-matrix has been determined for each of the new paramagnetic defects and possible models are assigned.

One area where further research would be useful is illuminating CdSiP₂ crystals with light that is longer wavelength (and thus lower energy) than 633 nm light. For example, illuminating a crystal with 800 nm laser light may convert fewer defects into a different charge state than 633 nm laser light. It may also be possible to photoinduce an optical absorption band with 633 nm light that is not photoinduced with 800 nm light, and therefore a correlation may be made between the absorption data and the EPR data. Once a correlation is confirmed, crystal growers can then use this information to know which as-grown defects to attempt to reduce during growth so that ultimately optical parametric oscillators that use CdSiP₂ will perform better.

Large-scale quantum chemistry modeling can be applied to experimental Sn₂P₂S₆ data to verify the proposed models. Furthermore, although several defects have been characterized in Te-doped Sn₂P₂S₆, a correlation has not been established between a particular defect and how that defect affects photorefractive properties. For example, each Te-doped Sn₂P₂S₆ sample that was studied contains the same two electron traps and five hole traps, but the concentration of each defect varies from crystal to crystal. The photorefractive properties of each sample could then be compared to the defect concentration to establish a correlation. Additionally, by knowing the thermal stabilities of each defect, a clever researcher may be able to extrapolate photorefractive response times at room temperature. Furthermore, the presence of an electron trap that is introduced during the crystal growth process via chemical vapor transport may produce competing fringes in SPS, thus hindering photorefractive response times [57]. Therefore, the vertical Bridgman growth method may be more effective at growing material that has fast response

times. Similarly, growing Sn-deficient SPS may also produce more of the desired stable hole traps (such as Defects D and E) which improve photorefractive gains [57]. This information may further assist in evaluating $\text{Sn}_2\text{P}_2\text{S}_6$ as a photorefractive material since fast response times are highly desired.

Bibliography

1. P. G. Schunemann, "CdSiP₂ and OPGaAs: New Nonlinear Crystals for the Mid-Infrared," OSA Tech. Digest (Optical Society of America, 2011), paper A1FA1.
2. F. K. Hopkins, B. Claflin, P. G. Schunemann, N. C. Giles, and L. E. Halliburton, "Potential of CdSiP₂ for Enabling Mid-Infrared Sources," Proc. SPIE 9616, 96160W (2015).
3. J. Wei, J. M. Murray, F. K. Hopkins, D. M. Krien, K. T. Zawilski, P. G. Schunemann, S. Guha, "Measurement of refractive indices of CdSiP₂ at temperatures from 90 to 450 K," Optical Materials Express **8**, 235 (2018).
4. A. Ruediger, O. Schirmer, S. Odoulov, A. Shumelyuk, and A. Grabar, "Studies of light-induced charge transfer in Sn₂P₂S₆ by combined EPR/optical absorption spectroscopy," Optical Materials **18**, 123 (2001).
5. A. Ruediger, Light Induced Charge Transfer Processes and Pyroelectric Luminescence in Sn₂P₂S₆, Ph.D. dissertation, University of Osnabruck, Osnabruck, Germany, 2001.
6. K. T. Zawilski, P. G. Schunemann, T. M. Pollak, D. E. Zelmon, N. C. Fernelius, and F. K. Hopkins, "Growth and characterization of large CdSiP₂ single crystals," Journal of Crystal Growth **312**, 1127 (2010).
7. S. G. Abrahams and J. L. Bernstein, "Luminescent piezoelectric CdSiP₂: Normal probability plot analysis, crystal structure, and generalized structure of the A^{II}B^{IV}C^V₂ family," Journal of Chemical Physics **55**, 796 (1971).
8. E. M. Golden, N. C. Giles, E. Maniego, F. K. Hopkins, K. T. Zawilski, P. G. Schunemann, and L. E. Halliburton, "Identification of native defects (vacancies and antisites) in CdSiP₂ crystals," Journal of Applied Physics **118**, 185702 (2015).
9. J. L. Shay, "Ternary chalcopyrite semiconductors growth, electronic properties, and applications," *International series of monographs in the science of solid state v.7*, (Peramon Press Inc., Maxwell House, Elmsford, NY, 1975).
10. A. Shileika, "Energy band structure and modulation spectra of A²B⁴C⁵ semiconductors," Surface Science **37**, 730 (1973).
11. V. Kremlin, B. Boulanger, V. Petrov, P. Segonds, B. Menaert, P. G. Schunemann, and K. T. Zawilski, "Nonlinear, dispersive, and phase-matching

- properties of the new chalcopyrite CdSiP₂,” *Optical Materials Express* **1**, 1292 (2011).
12. P. G. Schunemann, K. T. Zawilski, L. A. Pomeranz, D. J. Creeden, and P. A. Budni, “Advances in nonlinear optical crystals for mid-infrared coherent sources,” *Journal of the Optical Society of America B* **33**, D36 (2016).
 13. G. Dittmar and H. Schafer, The Crystal Structure of Sn₂P₂S₆, *Zeitschrift fur Naturforschung*. **29B**, 312 (1974).
 14. E. M. Golden, S. A. Basun, A. A. Grabar, I. M. Stoika, N. C. Giles, D. R. Evans, and L. E. Halliburton “Sulfur vacancies in photorefractive Sn₂P₂S₆ crystals,” *Journal of Applied Physics* **116**, 244107 (2014).
 15. E. M. Golden, “Hyperfine Interactions in the Electron Paramagnetic Resonance Spectra of Point Defects in Wide-Band-Gap Semiconductors,” PhD Dissertation, Air Force Institute of Technology, 2014.
 16. K. A. Brekhov, K. A. Grishunin, D. V. Afanasev, S. V. Semin, N. E. Sherstyuk, G. Kh. Kitaeva, E. D. Mishina, Th. Rasing, and A. V. Kimel, “Photoinduced dynamics and femtosecond excitation of phonon modes in ferroelectric semiconductor Sn₂P₂S₆,” *JETP Letters* **102**, 372 (2015).
 17. P. Ondrejko, M. Guennou, M. Kempa, Y. Vysokhanskii, G. Garbarino, and J. Hlinka, “An x-ray scattering study of Sn₂P₂S₆: absence of incommensurate phase up to 1 GPa,” *Journal of Physics: Condensed Matter* **25**, 115901 (2013).
 18. P. Ondrejko, M. Kempa, Y. Vysokhanskii, P. Saint-Gregoire, P. Bourges, K. Rushchanskii, and J. Hlinka, “Neutron scattering study of ferroelectric Sn₂P₂S₆ under pressure,” *Physical Review B* **86**, 224106 (2012).
 19. K. Glukhov, K. Fedyo, J. Banys, and Y. Vysokhanskii, “Electronic Structure and Phase Transition in Ferroelectric Sn₂P₂S₆ Crystal,” *International Journal of Molecular Sciences* **13**, 14356 (2012).
 20. I. P. Studenyak, V. V. Mitrovicij, Gy. Sh. Kovacs, O. A. Mykajlo, M. I. Gurzan, and Yu. M. Vysokhanskii, “Temperature variation of optical absorption edge in Sn₂P₂S₆ and SnP₂S₆ crystals,” *Ferroelectrics* **254**, 295 (2001).
 21. I. N. Geifman, I. V. Kozlova, U. M. Vysokhanski, V. Y. Kofman, and O. A. Mikailo, Temperature dependence of Mn²⁺ EPR in Sn₂P₂S₆ near the Phase Transition, *Applied Magnetic Resonance* **2**, 435 (1991).
 22. E. M Golden, S. A. Basun, D. R. Evans, A. A. Grabar, I. M. Stoika, N. C. Giles, and L. E. Halliburton, “Sn vacancies in photorefractive Sn₂P₂S₆ crystals:

- An electron paramagnetic resonance study of an optically active hole trap,” *Journal of Applied Physics*, **120**, 133101 (2016).
23. K. Z. Rushchanskii, Y. M. Vysochanskii, and D. Strauch, “Ferroelectricity, Nonlinear Dynamics, and Relaxation Effects in Monoclinic $\text{Sn}_2\text{P}_2\text{S}_6$,” *Physical Review Letters* **99**, 207601 (2007).
 24. J. Hlinka, R. Currat, M. de Boissieu, F. Livet, and Y. M. Vysochanskii, “Two-length-scale behavior near the ferroelectric phase transition of $\text{Sn}_2\text{P}_2\text{S}_6$,” *Physical Review B* **71**, 052102 (2005).
 25. J. Hlinka, I. Gregora, and V. Vorliceck, “Complete spectrum of long-wavelength phonon modes in $\text{Sn}_2\text{P}_2\text{S}_6$ by Raman scattering,” *Physical Review B* **65**, 064308 (2002).
 26. J. Grigas, E. Talik, V. Lazauskas, Yu. M. Vysochanskii, R. Yevych, M. Adamiec, and V. Nelkinas, “XPS of electronic structure of ferroelectric $\text{Sn}_2\text{P}_2\text{S}_6$ Crystals,” *Ferroelectrics* **378**, 70 (2009).
 27. B. E. Kananen, E. M. Golden, S. A. Basun, D. R. Evans, A. A. Grabar, I. M. Stoika, J. W. McClory, N. C. Giles, and L. E. Halliburton, “Dual role of Sb ions as electron traps and hole traps in photorefractive $\text{Sn}_2\text{P}_2\text{S}_6$ crystals,” *Optical Materials Express* **6**, 3992 (2016).
 28. S. A. Basun, L. E. Halliburton, and D. R. Evans, “Hyperbolic decay of photo-created Sb^{2+} ions in $\text{Sn}_2\text{P}_2\text{S}_6:\text{Sb}$ crystals detected with electron paramagnetic resonance,” *Applied Physics Letters* **110**, 052903 (2017).
 29. A. T. Brant, L. E. Halliburton, S. A. Basun, A. A. Grabar, S. G. Odoulov, A. Shumelyuk, N.C. Giles, and D. R. Evans, “Photoinduced EPR study of Sb^{2+} ions in photorefractive $\text{Sn}_2\text{P}_2\text{S}_6$ crystals,” *Physical Review B* **86**, 052903 (2012).
 30. J. A. Weil, J. R. Bolton, and J. E. Wertz, *Electron Paramagnetic Resonance*, (2nd ed. John Wiley & Sons, Hoboken, New Jersey, 2007).
 31. M. S. Holston, “Characterization of Point Defects in Lithium Aluminate (LiAlO_2) Single Crystals,” PhD Dissertation, Air Force Institute of Technology, 2015.
 32. R. T. Weber, J. Jiang, and D. P. Barr, *EMX User's Manual* (Bruker EPR Division, Billerica, Massachusetts, 1998).
 33. S. Yang, “Paramagnetic Resonance Studies of Defects in Titanium Dioxide Crystals,” PhD Dissertation, West Virginia University, 2010.

34. M. Fox, *Optical Properties of Solids*, (2nd ed. Oxford University Press, Oxford, UK, 2011).
35. B. C. Smith, *Fundamentals of Fourier Transform Infrared Spectroscopy*, CRC Press LLC, Boca Raton, Florida, 1996.
36. Nicolet FT-IR Spectrometer Product Specifications, Thermo Electron Corporation, 2004.
37. B. Henderson and G.R. Imbusch, *Optical Spectroscopy of Inorganic Solids* (Oxford University Press, New York, 1989)
38. Agilent Cary 4000/5000/6000i Series UV-VIS-NIR Spectrophotometers pamphlet, Agilent Technologies, May 2011.
39. M.H. Rakowsky, W. K. Kuhn, W.J. Lauderdale, L.E. Halliburton, G.J. Edwards, M.P. Scripsick, P. G. Schunemann, T. M. Pollack, M.C. Ohmer, F.K. Hopkins, "Electron-Paramagnetic-Resonance Study of a native acceptor in as-grown ZnGeP₂" *Applied Physics Letters* **64**, 1615 (1994)
40. L.E. Halliburton, G. J. Edwards, M.P. Scripsick, M.H. Rakowsky, P.G. Schunemann, and T.M. Pollak, "Electron-nuclear double resonance of the zinc vacancy in ZnGeP₂", *Applied Physics Letters* **66**, 2670 (1995)
41. N. C. Giles, L.E. Halliburton, P.G. Schunemann, and T.M. Pollak, "Photoinduced electron paramagnetic resonance of the phosphorus vacancy in ZnGeP₂" *Applied Physics Letters* **66**, 1758 (1995).
42. S.D. Setzler, N.C. Giles, L.E. Halliburton, P.G. Schunemann, and T.M. Pollak, "Electron paramagnetic resonance of a cation antisite defect in ZnGeP₂" *Applied Physics Letters* **74**, 1218 (1999).
43. S. D. Setzler, P.G. Schunemann, T.M. Pollak, M.C. Ohmer, J.T. Goldstein, F.K. Hopkinds, K.T., Stevens, L.E. Halliburton and N.C. Giles, "Characterization of defect-related optical absorption in ZnGeP₂" *Journal of Applied Physics* **86**, 6677 (1999).
44. N. C. Giles, Lihua Bai, M. M. Chirila, N. Y. Garces, K. T. Stevens, P. G. Schunemann, S. D. Setzler, and T. M. Pollak, "Infrared absorption bands associated with native defects in ZnGeP₂" *Journal of Applied Physics* **93**, 8975 (2003)
45. K. T. Stevens, S. D. Setzler, L. E. Halliburton, N. C. Fernelius, P. G. Schunemann, and T. M. Pollak, "Electron-nuclear double resonance study of the zinc vacancy in zinc germanium phosphide (ZnGeP₂)," *Materials Research Society Symposium Proceedings* **484**, 549 (1998).

46. U. Kaufmann, J. Schneider, and A. Rauber, “ESR detection of antisite lattice defects in GaP, CdSiP₂, and ZnGeP₂,” *Applied Physics Letters* **29**, 312 (1976).
47. U. Kaufmann, “EPR and optical absorption of Fe⁺, Fe²⁺, Fe³⁺, and Fe⁴⁺ on tetragonal sites in CdSiP₂,” *Physical Review B* **14**, 1848 (1976).
48. N. C. Giles, L. E. Halliburton, S. Yang, X. Yang, A. T. Brant, N. C. Fernelius, P. G. Schunemann, and K. T. Zawilski, “Optical and EPR study of point defects in CdSiP₂ crystals,” *Journal of Crystal Growth* **312**, 1133 (2010).
49. A. T. Brant, L.E. Halliburton, N. C. Giles, S. A. Basun, A. A. Grabar, and D. R. Evans, “Intrinsic small polarons (Sn³⁺ ions) in photorefractive Sn₂P₂S₆ crystals,” *Journal of Physics: Condensed Matter* **25**, 205501(2013).
50. E. M. Scherrer, B.E. Kananen, E. M. Golden, F. K. Hopkins, K. T. Zawilski, P. G. Schunemann, L. E. Halliburton, “Defect-related optical absorption bands in CdSiP₂ crystals,” *Optical Materials Express* **7**, 658 (2017).
51. E. M. Scherrer, L. E. Halliburton, E. M. Golden, K. T. Zawilski, P. G. Schunemann, F. K. Hopkins, K. L. Averett, and N. C. Giles, “Electron paramagnetic resonance and optical absorption study of acceptors in CdSiP₂ crystals,” *AIP Advances* **8**, 095014 (2018).
52. Y. A. Ossipyan, Y. S. Greznev, V. L. Matukhin, I. A. Safin, N. S. Sidorov, G.B. Teitelbaum, and O. V. Zharikov, “Specific features of NQR and EPR spectra of Y-Ba-Cu-O ceramics doped by Iodine and Bromine,” *Solid State Communications* **74**, 617 (1990).
53. T. Awano and T. Matsuyama, “Color centers in mixed crystals of alkali silver halides and ammonium silver halides,” *Radiation Effects and Defects in Solids* **134**, 389 (1995).
54. W. Schrittenlacher, “Analysis of the Hyperfine Interactions of the Vacancy-Iodine Complex in ZnSe,” *Physica Status Solidi (b)* **122**, 735 (1984).
55. W. Schrittenlacher, H. Nelkowski, and H. Pradella, “ESR and ODMR of Zinc-Vacancy-Associated Defects in ZnSe,” *Physica Status Solidi (b)* **122**, 285 (1984).
56. K. T. Han and J. Kim, “Zero-field splitting of Cr³⁺ in an electro-optical alpha-LiIO₃ single crystal,” *Solid State Communications* **102**, 467 (1997).
57. A. Shumelyuk, A. Hryhorashchuk, S. Odoulov, and D. R. Evans, “Transient gain enhancement in photorefractive crystals with two types of movable charge carrier,” *Optics Letters* **32**, 14 (2007).

Appendix A – MatLab Fitting Program to Extract EPR Parameters

Program

This appendix includes the MatLab fitting program and associated subroutine for finding the best-fit parameters for defect D. More specifically, the output of the program are the 6 terms that completely specify the g-matrix for this defect. The same subroutine was used for finding parameters for the other centers (A, B, C, and E) except changing the magnetic field values and associated crystal orientation. NOTE: In the subroutine, there is a choice that can be made for one plane of data, and that choice is noted within the subroutine. Experimental data determines which of the two choices is correct.

```
%           EPR_fitting

% This program determines the "best" g matrix for Center D in Te-doped Sn2P2S6.

% Input data are 98 EPR magnetic field values and their corresponding microwave
% frequencies. The output is 6 parameters for the g matrix.

% This program is used in conjunction with a second program named SUM_EPR_fitting.

clear all
format long

% Constants:

h = 6.62606957;    % Planck's constant
B = 9.27400968/h;  % Bohr magneton divided by Planck's constant
CTR = pi/180;     % Conversion constant, degrees to radians

% Spin-Hamiltonian parameters:
% Six for the g matrix (three principal values and three angles).

P(1) = 2.5;       % g matrix
P(2) = 1.9;
P(3) = 1.7;
P(4) = 61.2*CTR;
P(5) = 46.8*CTR;
```

```

P(6) = 85.9*CTR;
P(7) = (-6)*CTR;
P(8) = 1*CTR;
P(9) = (-1)*CTR;

% Step sizes for the parameters:

gg = 0.0001;          % step size for g values
delta1 = 0.01*CTR;   % step size for angles
delta2 = .1*CTR;

step(1) = gg;
step(2) = gg;
step(3) = gg;
step(4) = delta1;
step(5) = delta1;
step(6) = delta1;
step(7) = delta2;
step(8) = delta2;
step(9) = delta2;

sum2 = 0;
sum1 = SUM_EPR_fittingDefectD(P,B);

while sum2<sum1
  for n = 1:9
    summ = SUM_EPR_fittingDefectD(P,B);
    sum2 = summ;
    if n==1;
      sum1 = summ;
    end
    P(n) = P(n) + step(n);
    summ = SUM_EPR_fittingDefectD(P,B)
    if summ >= sum2;
      P(n) = P(n) - 2*step(n);
      summ = SUM_EPR_fittingDefectD(P,B);
      if summ >= sum2;
        P(n) = P(n) + step(n);
      end
    end
  end
end
if summ<sum2;
  sum2 = summ;
end
end

```



```
sum2
end

P(4) = P(4)*180/pi;
P(5) = P(5)*180/pi;
P(6) = P(6)*180/pi;
P(7) = P(7)*180/pi;
P(8) = P(8)*180/pi;
P(9) = P(9)*180/pi;

P          % Display final set of parameters.
sum2      % Display final value of sum2.

% End of program.
```

Subroutine

```
%          SUM_EPR_fitting

% This subroutine is used with EPR_fitting to determine the best g matrix for Center D in
% Te-doped Sn2P2S6.

% It calculates a sum of the frequency differences squared and returns the value to the
% main program. The input data are the measured EPR magnetic fields and microwave
% frequencies.

function summ = SUM_EPR_fittingDefectD(P,B)

CTR = pi/180;

% G is the 3x3 rotation matrix which takes the principal axes of the g matrix into the
% crystal coordinate system. [From "Classical Mechanics, 2nd ed." by Goldstein, pp.
% 146-147.]

% R is the 3x3 rotation matrix which takes the crystal coordinate system into the
% magnetic field coordinate system.

G(1,1) = cos(P(6))*cos(P(5)) - cos(P(4))*sin(P(5))*sin(P(6));
G(1,2) = cos(P(6))*sin(P(5)) + cos(P(4))*cos(P(5))*sin(P(6));
G(1,3) = sin(P(6))*sin(P(4));
G(2,1) = -sin(P(6))*cos(P(5)) - cos(P(4))*sin(P(5))*cos(P(6));
G(2,2) = -sin(P(6))*sin(P(5)) + cos(P(4))*cos(P(5))*cos(P(6));
G(2,3) = cos(P(6))*sin(P(4));
G(3,1) = sin(P(4))*sin(P(5));
G(3,2) = -sin(P(4))*cos(P(5));
G(3,3) = cos(P(4));

% Rotation from a to b.

%This loop is to fill all values that are constant for a-b plane
for mm=1:36
    Alpha(mm)=90*CTR;
    FRQ(mm)=9388.742;
end

h(1)=3557.603784;Beta(1)=(90-90)*CTR+P(7);
h(2)=3558.265299;Beta(2)=(90-89)*CTR+P(7);
h(3)=3585.668052;Beta(3)=(360-(90-85))*CTR+P(7);
```

```

h(4)=3531.534084;Beta(4)=(90-85)*CTR+P(7);
h(5)=3615.075395;Beta(5)=(360-(90-80))*CTR+P(7);
h(6)=3508.81205;Beta(6)=(90-80)*CTR+P(7);
h(7)=3644.482738;Beta(7)=(360-(90-75))*CTR+P(7);
h(8)=3478.733169;Beta(8)=(90-75)*CTR+P(7);
h(9)=3668.547847;Beta(9)=(360-(90-70))*CTR+P(7);
h(10)=3452.001954;Beta(10)=(90-70)*CTR+P(7);
h(11)=3689.265291;Beta(11)=(360-(90-65))*CTR+P(7);
h(12)=3429.941435;Beta(12)=(90-65)*CTR+P(7);
h(13)=3703.968962;Beta(13)=(360-(90-60))*CTR+P(7);
h(14)=3411.900121;Beta(14)=(90-60)*CTR+P(7);
h(15)=3712.388243;Beta(15)=(360-(90-55))*CTR+P(7);
h(16)=3713.991915;Beta(16)=(360-(90-50))*CTR+P(7);
h(17)=3385.830421;Beta(17)=(90-50)*CTR+P(7);
h(18)=3706.645091;Beta(18)=(360-(90-45))*CTR+P(7);
h(19)=3376.479006;Beta(19)=(90-45)*CTR+P(7);
h(20)=3696.612115;Beta(20)=(360-(90-40))*CTR+P(7);
h(21)=3373.13134;Beta(21)=(90-40)*CTR+P(7);
h(22)=3679.903853;Beta(22)=(360-(90-35))*CTR+P(7);
h(23)=3372.469825;Beta(23)=(90-35)*CTR+P(7);
h(24)=3663.185568;Beta(24)=(360-(90-30))*CTR+P(7);
h(25)=3378.433482;Beta(25)=(90-30)*CTR+P(7);
h(26)=3634.459785;Beta(26)=(360-(90-25))*CTR+P(7);
h(27)=3388.506549;Beta(27)=(90-25)*CTR+P(7);
h(28)=3607.057033;Beta(28)=(360-(90-20))*CTR+P(7);
h(29)=3399.792394;Beta(29)=(90-20)*CTR+P(7);
h(30)=3576.286568;Beta(30)=(360-(90-15))*CTR+P(7);
h(31)=3413.904711;Beta(31)=(90-15)*CTR+P(7);
h(32)=3544.233165;Beta(32)=(360-(90-10))*CTR+P(7);
h(33)=3435.293692;Beta(33)=(90-10)*CTR+P(7);
h(34)=3515.49736;Beta(34)=(360-(90-5))*CTR+P(7);
h(35)=3459.348779;Beta(35)=(90-5)*CTR+P(7);
h(36)=3484.085426;Beta(36)=(90-0)*CTR+P(7);

```

% Rotation from b to c.

% (Choice 1) Beta is 90 deg for low-field branch and 270 deg for high-field branch.

```
for mm=37:57
```

```
    Beta(mm)=90*CTR;
```

```
    FRQ(mm)=9388.742;
```

```
end
```

```
for mm=58:76
```

```
    Beta(mm)=270*CTR;
```

```
FRQ(mm)=9388.742;  
end
```

```
% (Choice 2) Beta is 270 deg for low-field branch and 90 deg for high-field branch.
```

```
% for mm=37:57  
%   Beta(mm)=270*CTR;  
%   FRQ(mm)=9388.742;  
% end  
% for mm=58:76  
%   Beta(mm)=90*CTR;  
%   FRQ(mm)=9388.742;  
% end
```

```
%lowfield branch first
```

```
h(37)=3487.423069;Alpha(37)=90*CTR+P(8);  
h(38)=3413.233173;Alpha(38)=85*CTR+P(8);  
h(39)=3304.2937;Alpha(39)=80*CTR+P(8);  
h(40)=3216.743209;Alpha(40)=75*CTR+P(8);  
h(41)=3141.22026;Alpha(41)=70*CTR+P(8);  
h(42)=3053.6697682;Alpha(42)=65*CTR+P(8);  
h(43)=2977.475282;Alpha(43)=60*CTR+P(8);  
h(44)=2911.975286;Alpha(44)=55*CTR+P(8);  
h(45)=2861.178962;Alpha(45)=50*CTR+P(8);  
h(46)=2821.087151;Alpha(46)=45*CTR+P(8);  
h(47)=2787.660603;Alpha(47)=40*CTR+P(8);  
h(48)=2761.600926;Alpha(48)=35*CTR+P(8);  
h(49)=2742.216536;Alpha(49)=30*CTR+P(8);  
h(50)=2734.198174;Alpha(50)=25*CTR+P(8);  
h(51)=2736.202764;Alpha(51)=20*CTR+P(8);  
h(52)=2747.568793;Alpha(52)=15*CTR+P(8);  
h(53)=2768.747292;Alpha(53)=10*CTR+P(8);  
h(54)=2801.70276;Alpha(54)=5*CTR+P(8);  
h(55)=2845.142237;Alpha(55)=1*CTR+P(8);  
h(56)=2855.16519;Alpha(56)=0*CTR+P(8);  
h(57)=2865.85968;Alpha(57)=-1*CTR+P(8);
```

```
%highfield branch
```

```
h(58)=3549.575399;Alpha(58)=85*CTR+P(8);  
h(59)=3632.455195;Alpha(59)=80*CTR+P(8);  
h(60)=3688.593753;Alpha(60)=75*CTR+P(8);  
h(61)=3724.686406;Alpha(61)=70*CTR+P(8);  
h(62)=3741.394668;Alpha(62)=65*CTR+P(8);  
h(63)=3731.371715;Alpha(63)=60*CTR+P(8);
```

h(64)=3700.621296;Alpha(64)=55*CTR+P(8);
h(65)=3649.834995;Alpha(65)=50*CTR+P(8);
h(66)=3591.020308;Alpha(66)=45*CTR+P(8);
h(67)=3518.103327;Alpha(67)=40*CTR+P(8);
h(68)=3430.612973;Alpha(68)=35*CTR+P(8);
h(69)=3341.719406;Alpha(69)=30*CTR+P(8);
h(70)=3248.82668;Alpha(70)=25*CTR+P(8);
h(71)=3170.627603;Alpha(71)=20*CTR+P(8);
h(72)=3083.738626;Alpha(72)=15*CTR+P(8);
h(73)=3014.900987;Alpha(73)=10*CTR+P(8);
h(74)=2944.058757;Alpha(74)=5*CTR+P(8);
h(75)=2884.572533;Alpha(75)=1*CTR+P(8);
h(76)=2875.221118;Alpha(76)=0*CTR+P(8);

% Rotation from c to a.

for mm=77:115

 Beta(mm)=0*CTR;

 FRQ(mm)=9388.742;

end

h(77)=2769.619289;Alpha(77)=-20*CTR+P(9);
h(78)=2774.971545;Alpha(78)=-15*CTR+P(9);
h(79)=2795.017451;Alpha(79)=-10*CTR+P(9);
h(80)=2822.420203;Alpha(80)=-5*CTR+P(9);
h(81)=2852.499085;Alpha(81)=0*CTR+P(9);
h(82)=2891.92938;Alpha(82)=5*CTR+P(9);
h(83)=2946.734886;Alpha(83)=10*CTR+P(9);
h(84)=3000.197316;Alpha(84)=15*CTR+P(9);
h(85)=3156.595469;Alpha(85)=25*CTR+P(9);
h(86)=3242.812909;Alpha(86)=30*CTR+P(9);
h(87)=3319.66891;Alpha(87)=35*CTR+P(9);
h(88)=3597.364837;Alpha(88)=50*CTR+P(9);
h(89)=3668.542836;Alpha(89)=55*CTR+P(9);
h(90)=3723.062687;Alpha(90)=60*CTR+P(9);
h(91)=3753.121522;Alpha(91)=65*CTR+P(9);
h(92)=3764.116701;Alpha(92)=70*CTR+P(9);
h(93)=3750.746083;Alpha(93)=75*CTR+P(9);
h(94)=3716.668043;Alpha(94)=80*CTR+P(9);
h(95)=3660.519462;Alpha(95)=85*CTR+P(9);
h(96)=3577.649689;Alpha(96)=90*CTR+P(9);
h(97)=3393.187268;Alpha(97)=100*CTR+P(9);
h(98)=3304.2937;Alpha(98)=105*CTR+P(9);
h(99)=3223.784333;Alpha(99)=110*CTR+P(9);

```

h(100)=3153.252815;Alpha(100)=115*CTR+P(9);
h(101)=3073.049147;Alpha(101)=120*CTR+P(9);
h(102)=2995.852366;Alpha(102)=125*CTR+P(9);
h(103)=2935.218513;Alpha(103)=130*CTR+P(9);
h(104)=2883.906007;Alpha(104)=135*CTR+P(9);
h(105)=2841.463814;Alpha(105)=140*CTR+P(9);
h(106)=2812.392239;Alpha(106)=145*CTR+P(9);
h(107)=2789.670206;Alpha(107)=150*CTR+P(9);
h(108)=2775.63306;Alpha(108)=155*CTR+P(9);
h(109)=2770.957353;Alpha(109)=160*CTR+P(9);
h(110)=2777.637651;Alpha(110)=165*CTR+P(9);
h(111)=2794.345913;Alpha(111)=170*CTR+P(9);
h(112)=2819.072537;Alpha(112)=175*CTR+P(9);
h(113)=2854.503675;Alpha(113)=180*CTR+P(9);
h(114)=2901.250726;Alpha(114)=185*CTR+P(9);
h(115)=2960.095482;Alpha(115)=190*CTR+P(9);

```

```

datapoints = length(h);

```

```

for nn=1:datapoints

```

```

    HH = h(nn);

```

```

    R(1,1) = cos(Alpha(nn))*cos(Beta(nn)); % Alpha and beta are
    R(1,2) = -sin(Beta(nn)); % equivalent to theta
    R(1,3) = sin(Alpha(nn))*cos(Beta(nn)); % and phi, the polar and
    R(2,1) = cos(Alpha(nn))*sin(Beta(nn)); % azimuthal angles used
    R(2,2) = cos(Beta(nn)); % to define the direction
    R(2,3) = sin(Alpha(nn))*sin(Beta(nn)); % of the magnetic field
    R(3,1) = -sin(Alpha(nn)); % relative to the zc and xc
    R(3,2) = 0; % directions in the crystal
    R(3,3) = cos(Alpha(nn)); % coordinate system.

```

```

    TG = G * R;

```

```

    W1 = B*HH*(P(1)*TG(1,1)*TG(1,3)+P(2)*TG(2,1)*TG(2,3)+P(3)*TG(3,1)*TG(3,3));
    W2 = B*HH*(P(1)*TG(1,2)*TG(1,3)+P(2)*TG(2,2)*TG(2,3)+P(3)*TG(3,2)*TG(3,3));
    W3 = B*HH*(P(1)*TG(1,3)*TG(1,3)+P(2)*TG(2,3)*TG(2,3)+P(3)*TG(3,3)*TG(3,3));
    freq(nn) = sqrt(W1^2 + W2^2 + W3^2);

```

```

end

```

```

summ=0;

```

```
for ii=1:datapoints
    % ii,FRQ(ii)-freq(ii)
    summ = summ + (FRQ(ii)-freq(ii))^2;
end
```

Appendix B – Magnetic Field Positions for Te-related Defects

This appendix includes all the data used for calculating the g matrix for each Te-related defect in $\text{Sn}_2\text{P}_2\text{S}_6$ crystals. Data is not available in all orientations due to multiple overlapping EPR signals. The term “corrected field” is to annotate that the data presented below is the magnetic field values after the Hall field vs. NMR probe corrections were applied (see Section 3.2). Also note that there is site splitting in two planes; when the crystal is rotated within the mirror plane (between c and a axes), there is no site splitting. The details of the g-matrix analysis that uses these magnetic field positions are in Section 6.1.2.

Defect A

Angle from c to a	Corrected Field (G)	Corrected Field (G)
-20	2690.05709	
-15	2705.462368	
-10	2722.832145	
-5	2744.221126	
0	2783.651422	
5	2837.123875	
10	2901.952333	
15	2990.174363	
20	3086.078986	
25	3162.939998	
30	3268.206059	
40	3585.001525	
45	3724.355648	
50	3864.035517	
55	3999.039678	
60	4098.963505	
65	4167.530525	
70	4210.569084	

75	4201.879184	
80	4146.412163	
85	4055.519017	
90	3931.875872	
95	3786.843747	
100	3652.841881	
105	3501.795983	
115	3230.444585	
120	3093.771602	
125	2997.521187	
130	2932.031214	
135	2855.16519	
140	2790.672501	
145	2750.741057	
150	2721.499093	
155	2706.795421	
160	2694.09634	
165	2699.448597	
170	2716.818374	
175	2742.878051	
180	2785.656013	
Angle from c to b	Corrected Field (G)	Corrected Field (G)
-1	2800.359685	
0	2812.397251	2784.994
1	2821.087151	2776.976
5		2732.865
10	2961.438557	2692.092
15	3072.021795	2668.698
20	3192.678099	2658.675
35	3589.015718	2702.786
40	3734.709358	2740.212
45	3862.361684	2785.656
50	3992.690138	2858.513
55	4095.615839	2918.661
60	4167.129607	3013.568
65	4201.879184	3104.456
70	4189.85164	3244.146
75	4140.398392	

80	4073.565343	
85	3927.190142	3651.84
90	3796.871711	3796.872
Angle from b to a	Corrected Field (G)	Corrected Field (G)
0	3794.195582	
5	3752.089158	3842.987
10	3704.630477	3901.13
15	3675.894672	3951.255
20	3650.456418	
25	3631.112119	4051.505
30		4092.94
35		4125.695
40	3587.011127	4158.44
45		4172.482
50		4175.158
55		4170.467
60		4149.088
65	3659.857947	4117.676
70		4077.575
75	3738.057024	4026.107
80	3788.181811	3969.968
85	3827.612107	3919.843
87	3849.662603	3894.445
88		3871.052
89		3869.047
90		3869.047
95	3800.910961	3931.199

Defect B

Angle from c to a	Corrected Field (G)	Corrected Field (G)
-20	2982.125932	
-15	2989.502825	
-10	3000.868853	
-5	3014.900987	
0	3041.632202	

5	3072.382621	
10	3112.484455	
15	3167.28996	
20	3217.414746	
25	3270.877176	
35	3379.816649	
40	3458.015726	
45	3514.490053	
50	3569.631327	
55	3618.753818	
60	3655.177229	
65	3674.561619	
70	3687.922215	
75	3684.584572	
80	3667.87631	
85	3635.792838	
90	3591.020308	
95	3535.543265	
100	3484.085426	
105	3411.228583	
115	3288.923502	
120	3237.460652	
125	3182.655146	
130	3131.197307	
135	3082.741342	
140	3045.982163	
145	3022.924361	
150	3000.868853	
155	2987.498234	
160	2986.786605	
165	2984.832129	
170	2996.188134	
175	3016.203971	
180	3041.632202	
Angle from c to b	Corrected Field (G)	Corrected Field (G)
-1		3049.661
0		3050.302
1	3067.701902	3031.609

5	3111.141379	2994.855
10	3169.956065	2961.439
15	3228.109237	2934.697
20	3293.388728	2917.979
25		2907.295
30	3413.904711	2907.966
35	3475.395526	2915.323
40	3524.177237	2930.027
45	3562.27448	2950.744
50	3594.357952	2980.813
55	3612.399266	3015.573
60	3617.079985	3057.007
65	3609.733161	3104.456
70	3583.663461	3167.961
75	3550.888406	3220.752
80	3518.163465	3271.549
85	3454.678083	3349.076
90	3409.223992	3409.224
Angle from b to a	Corrected Field (G)	Corrected Field (G)
0	3406.557887	
5	3409.223992	
10	3431.946026	3395.021
15	3444.645107	3394.52
20	3462.024907	3385.47
25	3482.080835	
30	3501.455203	3401.206
35	3516.830412	
40	3540.223984	
45	3556.260708	3431.946
50	3572.277387	3447.321
55	3580.325818	3458.016
60	3591.020308	3477.4
65	3595.691004	3493.126
70	3598.367133	3509.474
75	3595.029489	3523.556
80	3589.015718	3544.905
85	3582.330408	3559.608
87	3569.631327	

88		3568.288
89		3566.284
90		3566.284
95	3547.6109	3585.668

Defect C

Angle from c to a	Corrected Field (G)	Corrected Field (G)
-20	3619.756114	
-15	3669.8809	
-10	3706.645091	
-5	3735.380896	
0	3749.41303	
5	3746.736901	
10	3728.896046	
15	3687.922215	
20	3636.464376	
25	3579.65428	
30	3512.149694	
35	3447.050616	
45	3246.45124	
55	3131.197307	
60	3091.095474	
65	3049.319807	
70	2994.514301	
75	2964.109674	
80	2931.825744	
85	2912.982593	
90	2900.283512	
95	2901.285807	
100	2908.9684	
105	2924.057955	
110	2951.731328	
115	2991.507416	
120	3037.628032	
135	3235.290683	
140	3281.571667	

150	3429.941435	
155	3500.793688	
160	3580.325818	
165	3647.85045	
170	3698.616706	
175	3733.376306	
180	3752.760696	
Angle from c to b	Corrected Field (G)	Corrected Field (G)
-1		3754.0937
0		3755.4268
1		3752.7606
5		3752.0891
10		3732.3038
15		3708.6496
20		3669.2093
25		3635.1313
30	3701.964371	3609.0616
35	3666.543256	
40	3635.131323	3540.885498
45		3518.243648
50		3487.423069
55	3562.27447	3460.030339
60		3429.279920
75	3408.56247	
85	3322.304946	3275.557895
90	3275.557895	
Angle from b to a	Corrected Field (G)	Corrected Field (G)
0	3276.229433	3276.229
5	3244.817499	3350.409
10	3178.645965	
15	3120.502817	
20		3396.575
25	3002.201906	
30	2946.734886	3401.206
35	2905.961514	
40	2858.512856	3374.474
45	2833.214924	
50	2803.035813	

55	2789.003679	3279.567
60	2781.646832	3243.474
65	2780.985317	
70	2791.00827	3122.507
75	2807.616302	3054.331
80	2828.103218	2989.473
85	2865.198166	2946.715
87	2890.586305	2921.337
88	2903.024789	
89	2903.285386	
90	2903.956924	
95	2853.832137	2961.439

Defect D

Angle from c to a	Corrected Field (G)	Corrected Field (G)
-20	2769.619289	
-15	2774.971545	
-10	2795.017451	
-5	2822.420203	
0	2852.499085	
5	2891.92938	
10	2946.734886	
15	3000.197316	
25	3156.595469	
30	3242.812909	
35	3319.66891	
50	3597.364837	
55	3668.542836	
60	3723.062687	
65	3753.121522	
70	3764.116701	
75	3750.746083	
80	3716.668043	
85	3660.519462	
90	3577.649689	
100	3393.187268	

105	3304.2937	
110	3223.784333	
115	3153.252815	
120	3073.049147	
125	2995.852366	
130	2935.218513	
135	2883.906007	
140	2841.463814	
145	2812.392239	
150	2789.670206	
155	2775.63306	
160	2770.957353	
165	2777.637651	
170	2794.345913	
175	2819.072537	
180	2854.503675	
185	2901.250726	
190	2960.095482	
Angle from c to b	Corrected Field (G)	Corrected Field (G)
-1	2865.85968	
0	2855.16519	2875.221
1	2845.142237	2884.573
5	2801.70276	2944.059
10	2768.747292	3014.901
15	2747.568793	3083.739
20	2736.202764	3170.628
25	2734.198174	3248.827
30	2742.216536	3341.719
35	2761.600926	3430.613
40	2787.660603	3518.103
45	2821.087151	3591.02
50	2861.178962	3649.835
55	2911.975286	3700.621
60	2977.475282	3731.372
65	3053.669768	3741.395
70	3141.22026	3724.686
75	3216.743209	3688.594
80	3304.2937	3632.455

85	3413.233173	3549.575
90	3487.423069	
Angle from b to a	Corrected Field (G)	Corrected Field (G)
5		3484.085
10		3459.349
15	3544.233165	3435.294
20	3576.286568	3413.905
25	3607.057033	3399.792
30	3634.459785	3388.507
35	3663.185568	3378.433
40	3679.903853	3372.47
45	3696.612115	3373.131
50	3706.645091	3376.479
55	3713.991915	3385.83
60	3712.388243	
65	3703.968962	3411.9
70	3689.265291	3429.941
75	3668.547847	3452.002
80	3644.482738	3478.733
85	3615.075395	3508.812
87	3585.668052	3531.534
90	3558.265299	
95	3557.603784	

Defect E

Angle from c to a	Corrected Field (G)	Corrected Field (G)
-20	4308.824089	
-15	4235.967246	
-10	4057.518596	
-5	3873.647529	
0	3710.654272	
5	3548.913884	
20	3041.967971	
25	2905.961514	
30	2805.040403	

35	2720.827555	
40	2644.307323	
45	2587.832996	
50	2532.68671	
55	2498.919382	
60	2479.22428	
65	2472.87474	
70	2477.555458	
75	2496.599069	
80	2527.344476	
85	2567.426264	
90	2630.270177	
95	2707.797716	
100	2799.362401	
105	2907.966105	
110	3048.65328	
115	3211.400975	
120	3298.279929	
125	3522.513427	
130	3710.313491	
135	3898.459348	
140	4078.241051	
145	4205.22685	
150	4303.471832	
155	4346.911309	
160	4318.847042	
165	4213.074822	
170	4060.194724	
175	3897.782799	
180	3707.988166	
185	3512.821231	
190	3321.6735	
Angle from c to b	Corrected Field (G)	Corrected Field (G)
-1	3659.18641	
0	3645.154276	3679.904
5	3557.603784	3793.524
10	3491.43225	3895.117
15		3985.343

20		4080.241
25	3375.807468	4149.088
30		4212.574
35	3347.071663	4255.352
40	3349.747791	4268.051
45	3366.456053	4256.685
50	3383.805784	4228.62
55	3399.872577	4178.496
60	3435.96523	4099.184
65		4010.741
70		3909.149
75		3823.603
80		3733.376
85		3611.738
90		3522.844
Angle from b to a	Corrected Field (G)	Corrected Field (G)
0	3599.03867	3770.802
5	3431.946026	3930.538
10	3243.484446	4069.556
15	3126.516588	4173.815
20	3003.544982	4230.605
25	2890.586305	4225.273
30	2781.646832	4165.135
35	2709.471549	4069.426
40	2642.638501	3933.214
45	2589.837586	3782.168
50	2546.388086	3648.953
55	2517.612189	3488.756
60	2501.575465	3292.938
65	2495.601785	3138.544
70	2506.296275	2999.526
75	2526.342181	2891.258
80	2563.096348	2786.999
85	2605.87431	2715.485
89	2656.670635	
90	2646.647682	2667.365

Defect F

Angle from c to a	Corrected Field (G)	Corrected Field (G)
-15	3405.214811	
-10	3405.214811	
-5	3407.89094	
0	3410.567068	
5	3413.904711	
10	3417.242354	
15	3421.923073	
20	3426.603792	
25	3431.946026	
30	3437.969821	
35	3442.640517	
40	3446.649698	
45	3450.658879	
50	3454.006545	
55	3458.015726	
60	3459.348779	
65	3462.696445	
70	3462.696445	
75	3462.696445	
80	3461.353369	
85	3459.348779	
90	3456.682673	
95	3453.335007	
100	3449.325826	
105	3443.983592	
110	3439.302873	
115	3433.950617	
120	3429.941435	
125	3425.27074	
130	3419.246945	
135	3414.576249	
140	3411.228583	
145	3408.562477	
150	3406.557887	
155	3405.214811	
160	3404.543273	

165	3405.214811	
170	3405.886349	
175	3407.89094	
180	3410.567068	
185	3418.58543	
190	3413.904711	
195	3422.594611	
Angle from c to b	Corrected Field (G)	Corrected Field (G)
0	3522.844184	3522.844184
1	3516.158875	3528.196441
5	3510.145103	3529.529493
10	3500.793688	3528.857956
15	3495.441431	3528.196441
20	3484.746941	3525.520312
25	3473.390935	3518.835003
30	3463.35796	3512.149694
35	3453.335007	3504.131331
40	3445.316645	3495.441431
45	3436.626745	3487.423069
50	3430.612973	3476.728579
55	3421.261558	3466.034088
60	3416.58084	3456.011135
65	3412.571658	3446.649698
70		3437.298283
75	3409.223992	3429.941435
80	3410.567068	3423.927664
85	3413.904711	3413.904711
90	3414.576249	3414.576249
Angle from b to a	Corrected Field (G)	Corrected Field (G)
0	3524.177237	
10	3514.825822	
15		3525.520312
30	3491.392158	3518.855049
35	3485.418479	3512.821231
40	3480.066222	3508.140512
45	3472.719398	3502.126741
50	3467.377164	3496.112969
55	3462.024907	

60	3458.015726	3482.74235
65	3454.678083	3476.728579
80	3452.673492	
85	3452.001954	
87	3453.00425	
88	3452.001954	
89	3524.177237	

REPORT DOCUMENTATION PAGE				<i>Form Approved</i> OMB No. 0704-0188	
Public reporting burden for this collection of information is estimated to average 1 hour per response, including the time for reviewing instructions, searching existing data sources, gathering and maintaining the data needed, and completing and reviewing this collection of information. Send comments regarding this burden estimate or any other aspect of this collection of information, including suggestions for reducing this burden to Department of Defense, Washington Headquarters Services, Directorate for Information Operations and Reports (0704-0188), 1215 Jefferson Davis Highway, Suite 1204, Arlington, VA 22202-4302. Respondents should be aware that notwithstanding any other provision of law, no person shall be subject to any penalty for failing to comply with a collection of information if it does not display a currently valid OMB control number. PLEASE DO NOT RETURN YOUR FORM TO THE ABOVE ADDRESS.					
1. REPORT DATE (DD-MM-YYYY) 21 March 2019		2. REPORT TYPE PhD Dissertation		3. DATES COVERED (From - To) Sept 2015-March 2019	
4. TITLE AND SUBTITLE Optical and Electron Paramagnetic Resonance Characterization of Point Defects in Semiconductors				5a. CONTRACT NUMBER	
				5b. GRANT NUMBER	
				5c. PROGRAM ELEMENT NUMBER	
6. AUTHOR(S) Scherrer, Elizabeth M., Capt				5d. PROJECT NUMBER	
				5e. TASK NUMBER	
				5f. WORK UNIT NUMBER	
7. PERFORMING ORGANIZATION NAME(S) AND ADDRESS(ES) Air Force Institute of Technology Graduate School of Engineering and Management (AFIT/EN) 2950 Hobson Way Wright-Patterson AFB, OH 45433-7765				8. PERFORMING ORGANIZATION REPORT NUMBER AFIT-ENP-DS-19-M-091	
9. SPONSORING / MONITORING AGENCY NAME(S) AND ADDRESS(ES) Intentionally Left Blank				10. SPONSOR/MONITOR'S ACRONYM(S)	
				11. SPONSOR/MONITOR'S REPORT NUMBER(S)	
12. DISTRIBUTION / AVAILABILITY STATEMENT Distribution Statement A. Approved for Public Release; Distribution Unlimited.					
13. SUPPLEMENTARY NOTES This work is declared a work of the U. S. Government and is not subject to copyright protection in the United States.					
14. ABSTRACT Point defects in two semiconductor materials, both with promising optical properties, are investigated. The first material, CdSiP ₂ , is a nonlinear optical material in which absorption bands due to point defects can hinder performance when used in frequency conversion applications in the infrared. The second material, Sn ₂ P ₂ S ₆ , is a photorefractive material where point defects with specific properties are needed to optimize response in dynamic holography applications. Electron paramagnetic resonance (EPR) spectroscopy is used to identify the electronic structure of defects and their charge states. Correlations between EPR spectra and optical absorption allow assignments for the primary absorption bands in CdSiP ₂ . This research established that singly ionized silicon vacancies in CdSiP ₂ (V _{Si} ⁻) are responsible for three unwanted absorption bands peaking near 800 nm, 1.0 μm, and 1.9 μm. Two new acceptor defects were identified in CdSiP ₂ : the neutral silicon-on-phosphorus antisite (SiP ⁰) and the neutral copper-on-cadmium (Cu _{Cd} ⁰). These defects are associated with two additional broad photoinduced optical absorption bands appearing at 0.8 μm and 1.4 μm. A series of new point defects have been identified in tellurium-doped Sn ₂ P ₂ S ₆ crystals using EPR. An iodine ion on a phosphorous site and a tellurium ion on a Sn site are trapped-electron centers. Five trapped-hole centers involve Te ions replacing sulfur ions. The g-matrix has been determined for each of the new paramagnetic defects in Sn ₂ P ₂ S ₆ and models are assigned.					
15. SUBJECT TERMS Point Defects, EPR, Optical Absorption, CdSiP ₂ , Sn ₂ P ₂ S ₆					
16. SECURITY CLASSIFICATION OF:			17. LIMITATION OF ABSTRACT UU	18. NUMBER OF PAGES 142	19a. NAME OF RESPONSIBLE PERSON Dr. Nancy Giles, AFIT/EN
a. REPORT U	b. ABSTRACT U	c. THIS PAGE U			